Radio Frequency Coils for Ultra-high Field Magnetic Resonance Imaging

Inaugural-Dissertation
Zur Erlangung des Doktorgrades
der Humanwissenschaften

der Medizinischen Fakultät
der Eberhard Karls Universität
zu Tübingen

vorgelegt von

Shajan Gunamony

aus

Neyyoor, India

2016

Dekan: Professor Dr. I. B. Autenrieth

1. Berichterstatter: Professor Dr. K. Scheffler

2. Berichterstatter: Professor Dr. T. Schäffer

3. Berichterstatter: Professor Dr. M. Bock

For Binu and kids.

Contents

Abbreviations

ASL	Arterial spin labeling
BJT	Bipolar junction transistor
CB	Common base
CP	Circularly polarized
EM	Electro magnetic
EMF	Electro motive force
EPI	Echo planar imaging
ESR	Equivalent series resistance
FDA	Food and drug administration
FID	Free induction decay
FLASH	Fast low angle shot
fMRI	Functional magnetic resonance imaging
FOV	Field of view
GaAsFET	Gallium arsenide field effect transistor
GRAPPA	Generalized auto-calibrating partially parallel acquisition
GRE	Gradient echo
HEMT	High electron mobility transistor
LPSA	Lumped planar strip array
MRI	Magnetic resonance imaging
MRS	Magnetic resonance spectroscopy
MTL	Microstrip transmission line
NMR	Nuclear magnetic resonance
PSA	Planar strip array
RF	Radio frequency
RF PA	RF power amplifier
SAR	Specific absorption rate
SE	Spin echo
SNR	Signal to noise ratio
SWI	Susceptibility weighted imaging
TEM	transverse electro magnetic
TSE	Turbo spin echo
UHF	Ultra high field ($\geq$ 7T)

Chapter 1

INTRODUCTION

1.1   The advent of MR

Magnetic resonance imaging (MRI) has become a powerful tool not only to analyze the anatomical structures of the human body non-invasively but also to investigate brain activity with functional MRI (fMRI), which has contributed immensely to the advances in human cognitive neuroscience. Looking back at the origins of MRI, the nuclear magnetic resonance (NMR) phenomenon of atomic nuclei was first measured and described in 1938 by Isidor Isaac Rabi using a molecular beam in vacuum. This phenomenon was simultaneously demonstrated in condensed matter in late 1945 by Felix Bloch and Edward Purcell, which won them the Nobel Prize in physics in the year 1952 (Bloch et al., 1946; Purcell et al., 1946). Subsequent developments of the spin-echo method by Erwin L. Hahn in 1951 (Hahn 1950) and Fourier transform NMR spectroscopy by Richard R. Ernst in 1966 (Ernst 1966) are among the most important contributions in the history of MRI. However, the use of NMR for biomedical applications was fuelled by the measurement of longer relaxation times in cancerous tissue by Raymond Damadian in 1971 (Damadian, 1971). The foundation for MRI in its current form was laid in 1973 by Paul C. Lauterbur (Lauterbur 1973) and Peter Mansfield (Mansfield et al., 1973), both independently describing the use of magnetic field gradients to localize NMR signals. Ever since, an array of novel techniques, methods and hardware advancements has transformed MRI in to a remarkable diagnostic tool and is now considered the imaging modality of first choice.

1.2   Race towards higher field strength

The main magnet that generates the static magnetic field is a fundamental component of an MR system. Early commercial clinical scanners were permanent magnets at field strengths between 0.3 T and 0.7 T (Mcfarland et al., 1986; Posin et al., 1985). Permanent magnets offered small physical footprint, low initial and operational costs

and low energy deposition in tissue. Central to the advancement of human MRI on to higher field strengths has been the development of superconducting horizontal magnets with bore dimensions large enough to accommodate an adult human body. Cylindrical closed bore superconducting magnets were used for the construction of 1 T and 1.5 T clinical scanners (Bottomley et al., 1984). Introduced for clinical usage in 1985, 1.5 T scanner was considered the optimum field for clinical applications for over two decades. Technical developments evolved at a rapid rate and the 3 T whole body MR systems offered by different manufacturers are current clinical standard (Soher et al., 2007).

The promise of an increase in signal to noise ratio and spectral resolution proportional to the main magnetic field strength motivated a few academic research laboratories to pursue even higher magnetic fields. The first 8 T magnet was installed at the Ohio State University in 1998 (Abduljalil et al., 1999) while the first 7 T magnet was installed at the center for magnetic resonance research, University of Minnesota in 1999 (Vaughan et al., 2001). Despite serious concerns like the increased radio frequency (RF) energy deposition, susceptibility artifacts, RF power requirements and the dielectric resonance phenomenon (Barfuss et al. 1990), early results from these labs demonstrated that ultra-high field scanners offer substantial benefits in aspects of MRI and MR spectroscopy (MRS). Currently, there are more than 40 research laboratories with 7 T installations actively involved in clinical studies (as approved by the site's institutional review board) and methods development, bringing in more man-power and talent to overcome the challenges at ultra-high field (UHF). MRI at 7 T is not currently approved for clinical usage by the US food and drug administration (FDA) or as well as the international electro-technical commission. Compared to the early 7 T images, the anatomical and functional brain images produced by the current state-of-the-art 7 T systems are exquisite. Great strides in instrumentation have resulted in setup times comparable to clinical scanners, increasing throughput of the UHF scanners. UHF MRI is destined to make increasing contribution to clinical radiology and MRI at field strengths up to 7 T will most likely be approved for clinical use soon, at least for specific clinical applications.

1.3   Why Ultra-high field

NMR phenomenon is a result of the interaction of a nuclear spin with an external magnetic field. Atomic nuclei with an odd number of protons or neutrons possess a property called spin which is key to enabling NMR. The human body has an abundance of water in which the hydrogen nucleus contains a single proton and exhibits a spin with an associated magnetic moment.

$$\vec{\mu} = \gamma \vec{J} \tag{1.1}$$

J is the spin angular momentum and the proportionality constant γ is the gyromagnetic ratio and depends on the type of nucleus. The hydrogen proton has a γ value of 42.6 MHz/Tesla. Under the influence of an external magnetic field (B_0), the proton spins around the direction of B_0 like a spinning gyroscope. This property is called precession with the frequency given by the Larmor equation

$$\omega_0 = \gamma B_0 \tag{1.2}$$

The applied external magnetic field is usually defined along the Z direction. Spins align in separate orientations to the applied magnetic field. For a spin ½ system, m = ± ½ and there are two possible states.

$$\mu_z = \frac{1}{2} \Upsilon h \text{ (Aligned with } B_0) \tag{1.3}$$

$$\mu_z = -\frac{1}{2} \Upsilon h \text{ (Aligned against } B_0) \tag{1.4}$$

where, $\hbar = \frac{h}{2\pi}$ and h is the Planck's constant. Spins aligned with the external field are in a lower and spins aligned against B_0 are in the higher energy state. Thus, the energy level of atomic nuclei with spin quantum number j is split by an external field B_0 into $2j + 1$ Zeeman levels. j is an integer for even mass numbers and half integer for odd mass numbers. Using the Boltzmann relationship, the population difference between the upper and lower levels can be shown to be

$$\Delta N_p = \frac{N_p \hbar \Upsilon B_0}{2KT_s} \tag{1.5}$$

where, N_p is the number of protons, T_s is the absolute temperature of the sample and K is Boltzmann's constant. If the magnetic moment associated with each proton is $\frac{\Upsilon\hbar}{2}$, the net magnetization, which is the maximum available magnetization for the formation of the MR signal, is then given by:

$$M_0 = \frac{N_p \Upsilon^2 \hbar^2 B_0}{4KT_s}$$
(1.6)

Thus, available magnetization for the formation of the MRI signal is proportional directly to the strength of the applied magnetic field and inversely to the sample temperature. While the sample temperature cannot be influenced, equation 1.6 provides sufficient impetus for increasing the external magnetic field B_0 in search of achievable signal-to-noise (SNR).

1.4   RF excitation and reception

The sample magnetization must be perturbed from its equilibrium state and this is accomplished by an oscillating magnetic field (B_1) at the Larmor frequency applied orthogonal to the static field. An RF coil is used to generate the B_1 field and an RF pulse is applied to tilt the sample magnetization to the transverse XY plane. The B_1 field can be decomposed into two counter rotating components B_1^+ and B_1^-. B_1^+ is the component that rotates along with the precession of the magnetic moment whereas B_1^- is the component that rotates in the negative sense with the same frequency of ω_0.

$$\vec{B}_1^+ = (\vec{B}_x + i\vec{B}_y)/2$$
(1.7)

and

$$\vec{B}_1^- = (\vec{B}_x - i\vec{B}_y)^*/2$$
(1.8)

The component B_1^+ is to referred as the transmit / excitation field and B_1^- is referred to as the receive field (Hoult, 2000).

A unit current passing through a wire creates a magnetic field. This is defined by Ampere's law.

$$\oint B.\,dl = \mu_0 \int J.\,ds \qquad (1.9)$$

B is the magnetic field and J is the total current density. In MRI, the transmit coil is the current carrying conductor that is expected to produce a uniform magnetic field over the sample volume.

The nutation angle α of the sample magnetization by due to the applied RF pulse to tip from equilibrium to the transverse plane is given by

$$\alpha = \int_0^\tau \gamma \vec{B}_1 \, dt \qquad (1.10)$$

where, τ is the duration of the RF pulse. When the RF source is OFF, the precessing magnetization in the transverse plane induces a signal in the nearby RF coil. This induced signal, called the free induction decay (FID), exponentially decays due to spin relaxation and forms the basis for all NMR experiments. A detailed discussion on principles of NMR, spin dynamics and signal strength calculation can be found in several articles and text books (Haacke et al, 1999; Hoult et al, 1997; Hoult, 2000).

The receive function is defined using Faraday's laws of induction where the time varying magnetic field of the precessing sample magnetization induces an EMF ξ across the terminals of the receive coil.

$$\xi = \oint E.\,dl = -\frac{d}{dt}\Phi_s = -\frac{d}{dt}\int B.\,ds \qquad (1.11)$$

Φ_S is the magnetic flux through the surface. The induced EMF ξ is proportional to the negative of the rate of change of magnetic flux.

The principle of reciprocity establishes the correspondence between the transmit and receive functions of an RF coil. The sensitivity at any point in space during signal reception is proportional to the B_1 field strength produced at that point while unit current is applied to the same coil (Hoult et al., 1976). Hence, as per the principle of reciprocity,

to maximize the induced receive signal, the B_1 field produced by the coil has to be maximized. Since the strength of the B_1 field is inversely proportional to the distance from the current carrying conductor, RF coils should closely follow the contours of the imaging volume to maximize the receive sensitivity.

1.5 An RF resonator

An RF coil plays a significant role in an MR experiment. A typical RF coil is a resonant structure designed to generate an oscillating magnetic field within a confined region of interest. Applying the reciprocity principle, the RF coil detects the induced EMF by the precessing sample magnetization. The resonant frequency of the RF coil is given by

$$f = \frac{1}{2\pi\sqrt{LC}} \tag{1.12}$$

where, L and C are the equivalent inductance and capacitance of the resonant structure. The quality or Q-factor is often used as a figure of merit to characterize an RF coil. The Q-factor is defined as the ratio of the peak energy stored over the energy lost per duty cycle.

$$Q = 2\pi \frac{Max\ energy\ stored\ (I^2L/2)}{Energy\ loss\ per\ cycle\ (I^2R/2)} \tag{1.13}$$

Which gives
$$Q = \frac{\omega L}{R} \tag{1.14}$$

and R is the total loss factor.

The detected signal level increases by a factor of Q because the voltage across any capacitor at resonance is given by

$$V = Q\xi \tag{1.15}$$

From equation 1.14, it is clear that the total loss factor R must be minimized to increase the coil Q factor. While sample loss cannot be controlled, careful design considerations can minimize coil loss. The aim of the coil designer is to maximize the coil unloaded Q (Q_{UL}) and maximize the Q ratio ($\frac{Q_{UL}}{Q_L}$), where Q_L is the Q-factor when the coil is loaded by a sample. Furthermore, the loss in SNR compared to a lossless situation can be

estimated as $\sqrt{1 - \frac{Q_L}{Q_{UL}}}$ (Hayes et al., 1985), which establishes further the importance of maximizing the Q ratio. Hence it is important to understand the various loss mechanisms and minimize the controllable loss factors.

1.6   The loss mechanisms

1.6.1   Resistive loss (R_Ω)

The resistive losses are caused by the losses to the coil conductor and the coil components. At high frequencies, due to skin effect, the current flows on the outer surface of the wire. Hence the resistance of the wire is greater than the resistance at low frequencies. The coil conductor loss increases with $\sqrt{\omega}$. Copper is predominantly used for coil conductors due to its very high conductivity (59 x 10^6 Siemens/meter). The conductivity of silver is about 7% higher than that of copper (63 x 10^6 Siemens/meter). Coil loss is a critical factor at lower field strength and for small and micro coil designs. Coil conductor loss is not a major concern on coils for human imaging at higher field strength because of sample noise dominance.

Coil component losses consist of losses to the capacitors and to the detuning PIN diodes used in actively detunable coils. The series resistance (ESR) of the capacitors is defined in the manufacturer's datasheet. The value and the total number of number of distributed capacitors used to achieve the desired resonance frequency determine the total loss due to the capacitor. In addition to the PIN diode detuning circuit, a passive detuning circuit or a protection fuse is used in receive-only coils to provide secondary safety in case of malfunction of the active detuning circuit. This further adds to the coil loss, thereby reducing the unloaded Q of the coil.

1.6.2   Radiation loss (R_r)

The energy loss to the far field is represented by radiation resistance. At higher NMR frequencies, RF coils behave like energy radiating antennas, resulting in decreased RF transmit efficiency, decreased signal to noise ratio and more importantly, increased power absorption in the human subject. On most conventional segmented loop coils

used for human imaging at UHF MRI, to reduce the radiation of energy to the far-field, a local shield is added at a distance to maximize the Q_{UL}/Q_L ratio. TEM coils and microstrip transmission line based RF coils are also well suited for higher NMR frequencies because of the inherent RF shielding available in the basic coil element of these designs.

The Q factor of an unloaded coil Q_{UL} is defined as

$$Q_{UL} = \frac{\omega L}{R_C} \qquad (1.16)$$

where R_C is the sum of ohmic resistance R_Ω and radiation resistance R_r of the RF coil.

1.6.3 Sample Loss (R$_S$)

Conduction Current:A transmitting RF coil produces an oscillating magnetic field B_1 which induces RF currents in any conducting sample loading the coil. Some of the transmitted power is dissipated in the conducting lossy sample. The sample noise is unavoidable but can be minimized by restricting the RF coil designs to the volume of interest. Due to the increase in tissue conductivity with frequency, the losses to the tissue conductor increases with field strength.

It is desirable that most of the noise seen in the MR image comes from the sample being imaged because the sample noise is unavoidable. When the coil is loaded with the sample, the coil is damped by the sample resistance R_s. The loaded Q of the coil is then defined as

$$Q_L = \frac{\omega L}{R}, R = R_C + R_S \qquad (1.17)$$

The coil is sample noise dominant when the ratio of Q_{UL}/Q_L is maximized.

Displacement Current: An electric field in the near field of the coil generates displacement current in a dielectric sample placed in the RF field of the coil. Consider a simple loop coil with a single capacitor as shown in Fig. 1 and the inductive voltage buildup as a function of distance around the coil. The distribution of voltage along the coil implies that there are electric fields between different parts of the coil. This

corresponds to stray capacitance outside the coil capacitor. When the voltage excursions are larger, the stray electric field and the stray capacitance are also larger.
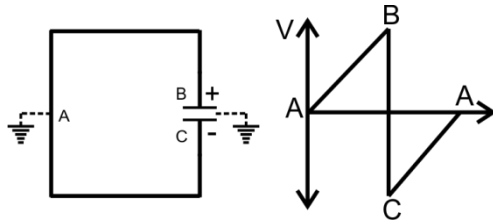

Figure 1. RF coil with a single capacitor and the voltage build-up as a function of distance around the coil.

Consider replacing the single capacitor with a series combination of 4 capacitors of equal value, while maintaining equal spacing between the capacitors as shown in Fig. 2. The maximum voltage excursion will be 1/4th of that of Fig. 1. The penetration of the electric field lines into the volume surrounding the coil is minimized and the stray capacitance is greatly reduced.
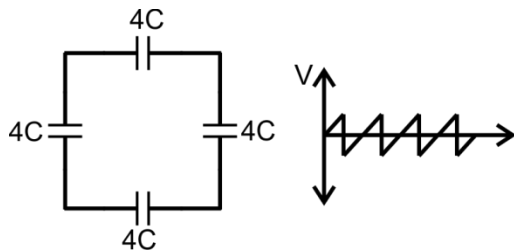

Figure 2. RF coil with four distributed capacitors and the voltage excursion is 1/4th of that in Fig. 1.

Capacitors of equal value are symmetrically distributed along the loop with each segment length in the range of $\frac{\lambda}{10}$ to $\frac{\lambda}{20}$. Non-optimal distribution of capacitors results not only in a lower Q_{UL}, but also makes the resonant frequency of the loop highly sensitive to variations in sample load.

1.7 Building blocks of an RF system

1.7.1 Transceiver Coil

A transceive coil performs a dual role. For transmit, it produces a magnetic field to rotate the spin magnetization, and during reception, a signal is induced by the magnetic flux created by the precession of the nuclear magnetization. During transmission, power from the RF amplifier (RF PA) is transferred using a coaxial cable with a characteristic impedance of 50 Ω to the RF coil through a matching circuit which matches the coil to

50 Ω. During reception, the signal is transferred to a noise matched preamplifier which requires a source impedance of 50 Ω (provided by the coil) for optimum noise figure. In addition, a TR switch is used to separate the transmit and receive functions and to protect the preamplifier from high power RF. A functional block diagram of the transceive coil setup is shown in Fig. 3.
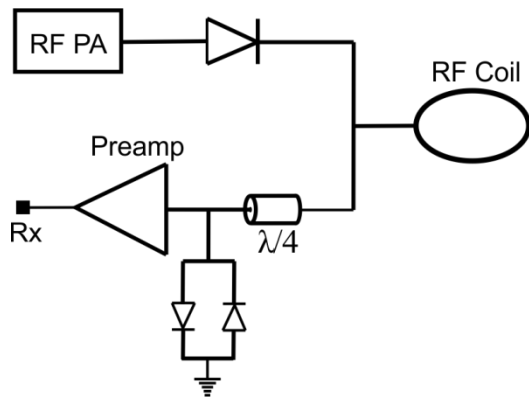

Figure 3. Functional block diagram of a TR switch.

1.7.2 Quadrature Excitation

Driving an RF coil in the quadrature mode produces a circularly polarized magnetic field. A quadrature operation requires two orthogonal feed ports on an RF Coil structure or two RF coils with their respective EM fields orthogonal to each other. The two feed ports are driven by two RF currents of same magnitude with 90° phase difference. Consider a 2 coil system with coils A and B as shown in Fig. 4.
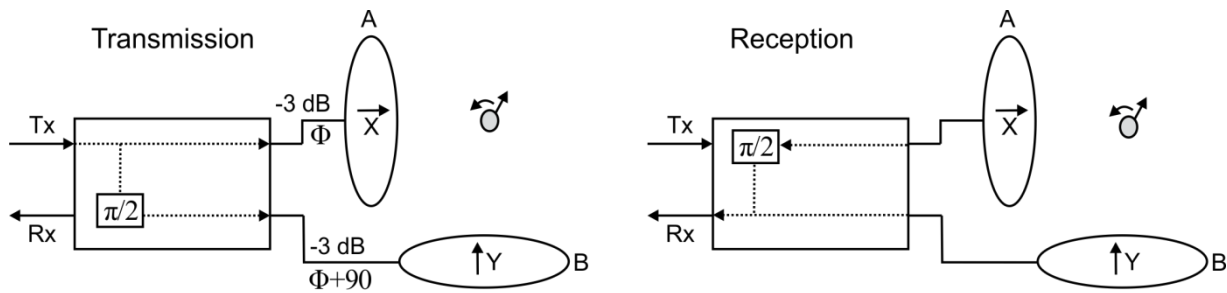

Figure 4: Representation of quadrature excitation and reception

To generate a B_1 field which rotates in the same direction as the nuclear precession, RF current at coil B should be delayed by 90° compared to coil A. This function is achieved by a quadrature hybrid which acts as a splitter during excitation and as a combiner during acquisition.

During reception, an EMF is first induced in coil A as the nuclear magnetization is aligned with coil A before pointing to coil B. The received signal from the two coils is in phase when the signal from coil A is delayed by 90° and hence doubles the available signal. The noise from the two orthogonal coils is uncorrelated, resulting in an increase in the noise level by a factor of √2. This leads to an increase in signal to noise ratio of up to √2 for orthogonal coils. Applying the principle of reciprocity to the transmit condition, a quadrature coil produces the same flip angle as that of a linear coil with half the amount of transmit power.

The size of the samples used for MR imaging often ranges from small phantoms to large samples that completely fill the coil volume, mismatching the coil input impedance. Amplitude and phase balance of the quadrature hybrid is disturbed due to this impedance mismatch. While the loss in transmit efficiency due to this is overcome by applying additional RF power, the loss in sensitivity during receive is not recovered. By inserting two TR switches as shown in Fig. 5 allows the quadrature hybrid to be bypassed during signal acquisition. The signals from the two coils are processed by the MR scanner as a two channel receive array.
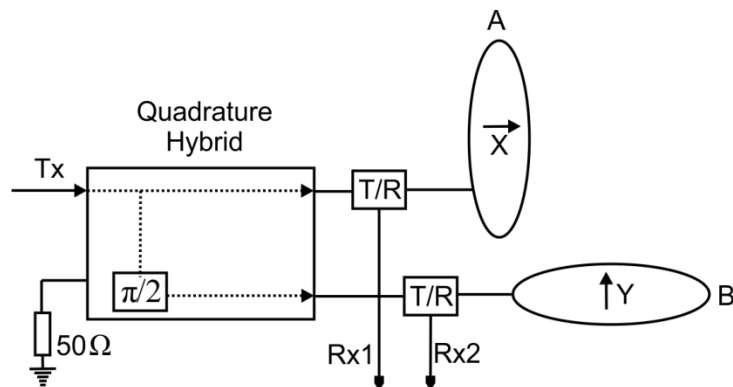

Figure 5: Transceive coil with quadrature excitation and reception with two channels.

1.7.3 Transmit Only Receive Only Coil

Another approach is to use a larger outer coil to generate a homogeneous transmit field and a smaller coil that closely follows the contours of the anatomy for signal reception. A functional block diagram of this setup is shown in Fig. 6.
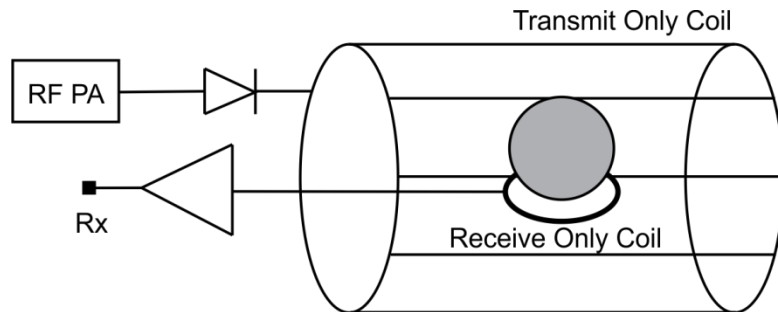

Figure 6: Transmit-only receive-only setup for optimum SNR.

The receive coil is actively detuned during transmit to prevent induced RF current in the receive coil which is placed close to the anatomy. During acquisition, the transmit coil is actively detuned to prevent noise coupling into the received signal. A typical schematic of a single receive element is shown in Fig. 7.
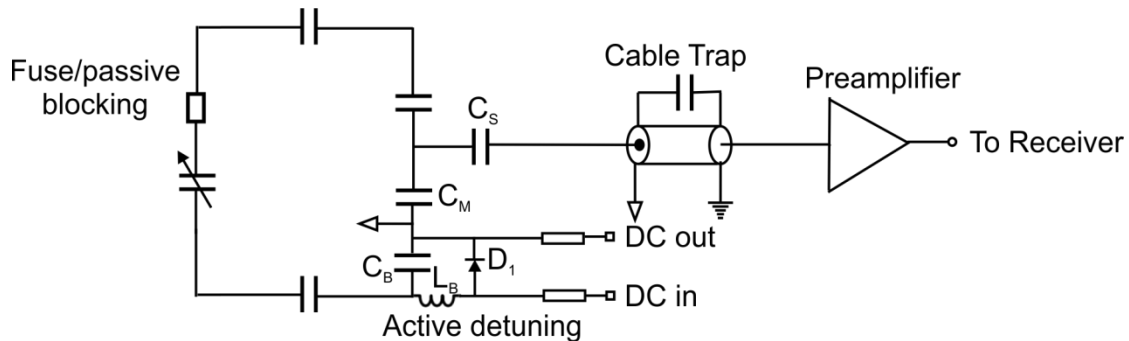

Figure 7: Equivalent circuit of a single receive coil

The active detuning circuit consists of a PIN diode (D_1) in series with an inductor (L_B) across one of the capacitors (C_B) in the loop. Depending on the size of the resonant coil and the operating frequency, one or more blocking networks are used per coil element.

The scanner provides the control signal to switch the PIN diodes. The blocking resistance R_b provided by the blocking network is

$$R_b = \frac{X^2}{R} = \frac{1}{R(\omega C_B)^2} \tag{1.18}$$

where R is the total series resistance of the blocking network. The smaller the value of the capacitor C_B, the larger is the blocking resistance. A protection fuse or a passive blocking circuit using fast recovery diodes is added for secondary level of safety, in case of malfunction of the active detuning circuit.

1.7.4 Phased Array Coils

The phased array technique that forms the basis for most of today's array coils was proposed by Roemer et al (Roemer et al., 1990). A smaller surface coil yields higher SNR closer to the coil but the sensitive region of a surface coil is much smaller than that of a volume coil (Wright et al., 1997). By using the phased array approach, the high signal to noise ratio of a small surface coil is maintained over an extended volume using an array of RF coils. The principal consideration in a coil array design is to make the individual array elements to function independently.
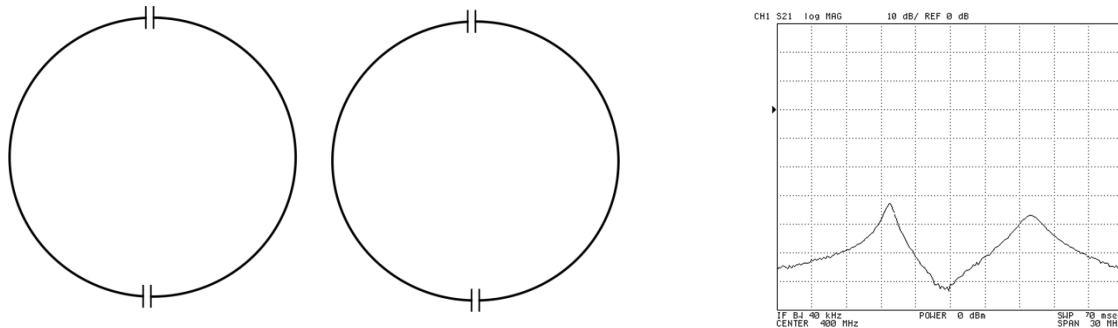

Figure 8: Two coils, tuned to the same frequency, are coupled resulting in a resonant peak split.

When a multiple of resonant elements are placed close to each other, the inductive coupling between the resonant elements causes the resonant frequency to split, reducing sensitivity at the Larmor frequency (Fig. 8).

There are different design options to cancel the mutual inductance. The most common method is to critically overlap the adjacent coils (Fig. 9a) to the point where the mutual inductance is zero and restores the sensitivity of each single element even though multiple coils are simultaneously active (Roemer et al. 1990). Another way to cancel the mutual inductance is by inductive decoupling (Fig. 9b). Two inductors, one for each adjacent loop, are wound in opposite directions and placed in line with each other. The number of turns and diameter of the inductors depends on the size of the loop and the proximity of the adjacent loops. Note that the size of the loops are smaller when inductive decoupling is used. At low frequencies, where sample loading is less, this is not a preferred choice.
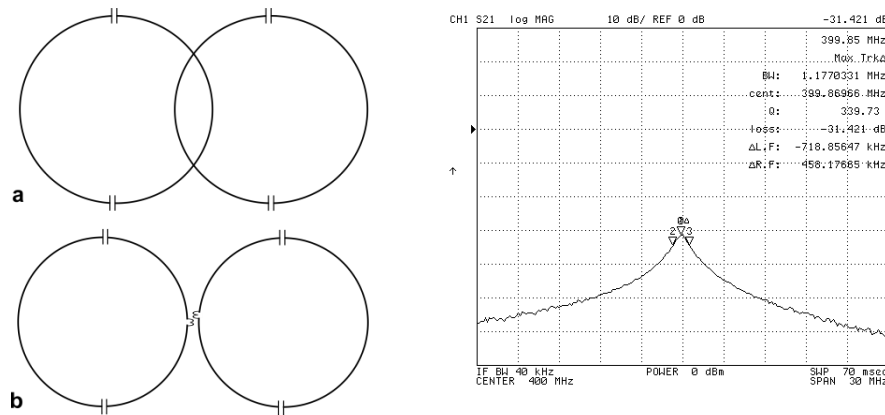

Figure 9: a) Two coils are critically overlapped to cancel the mutual inductance. b) Inductive decoupling. The plot on the right shows that the performance of a single coil can be restored by cancelling the mutual inductance.

1.7.5 Low noise preamplifiers

Low noise preamplifiers in an RF coil perform a dual role. Fig. 7 shows the implementation of a single element in a coil array. The signal induced in the coil element is amplified by the low noise preamplifier and fed to the system receivers. Furthermore, the non-adjacent loops are decoupled using preamplifier decoupling. Modern MRI preamplifiers are constructed using low noise GaAsFETs / HEMTs and these devices have high input impedance. Noise matching is accomplished using a LC circuit which transforms the high input impedance at the input of the active device to low impedance

at the preamplifier input. Typical values for the input impedance of state of the art MRI preamplifiers are in the range between 1 and 2 ohms. Preamplifier decoupling utilizes this low input impedance to transform to high impedance at the input of the RF coil, blocking the current flow. Fig. 10 shows the equivalent circuit derived from Fig. 7 showing only the components that contribute to preamplifier decoupling. Capacitors C_M, C_S, inductance L (inductance of the part of the cable/cable trap between the coil and the preamplifier) and R$_{in}$ (input impedance of the preamplifier) form a parallel resonant circuit and creates high impedance at the Larmor frequency, thereby reducing the current flow in the coil.
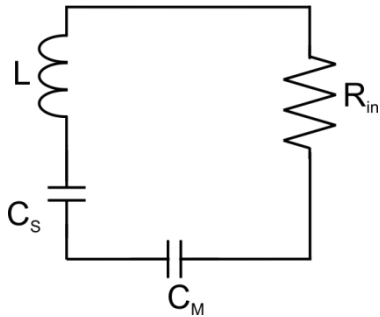

Figure 10: Input circuit of Fig. 7 with components that contribute to preamplifier decoupling.

The preamplifier is placed close to the coil to reduce the noise in the receive chain. The noise figure of the receive chain is minimum when the amplifying stage is in the first stage as defined by the Friis equation (1.19). The noise contribution from the subsequent stages is scaled by the gain of the first amplifying stage as shown in equation 1.19.

$$F_{total} = F_1 + \frac{F_2 - 1}{G_1} + \frac{F_3 - 1}{G_2} + \cdots \qquad (1.19)$$

1.8 RF coils for ultra-high field

At high Larmor frequencies, the wavelength in tissue is comparable or even smaller than the sample dimensions and B_1 exhibits traveling wave behavior (Wang et al. 2002). In this regime, RF excitation coils that are used in clinical scanners cannot be adapted to UHF scanners. The RF field produced by a volume resonator is given by:

$$\left| \sum B_{1i}^+(\vec{x}) \right| \qquad (1.20)$$

where i denotes the individual current carrying elements of the resonator, $\vec{x}$ describes spatial location and B_1^+ is a complex quantity that is responsible for spin excitation. At the center of the coil, which is equidistant from each coil element, the B_1^+ patterns add constructively resulting in central brightening. At spatial locations away from the center, the complex summation leads to partial cancellation. Due to this constructive and destructive interference, the distribution of B_1^+ is highly inhomogeneous at higher frequencies.

By splitting the volume coil to a multiple of individual coil elements, control over the magnitude and phase of the current to each of the coil element is obtained.

$$\left| \sum B_{1i}^+(\vec{x}) \right| \Rightarrow a_1 B_{1\,coil1}^+(\vec{x})e^{-i\omega t_1} + \cdots + a_n B_{1\,coiln}^+(\vec{x})e^{-i\omega t_n} \qquad (1.21)$$

This results in a transmit array. The process of controlling the current to the individual elements of a transmit array is called RF shimming. In the static shimming approach, the phase is altered which is commonly achieved by inserting coaxial cables of different length in the transmit path. Both amplitude and phase of the current to the coil elements are controlled in dynamic RF shimming approach. This is accomplished by an array of RF amplifiers. A functional block diagram of a static RF shimming setup for a transceiver array coil is shown in Fig. 11.
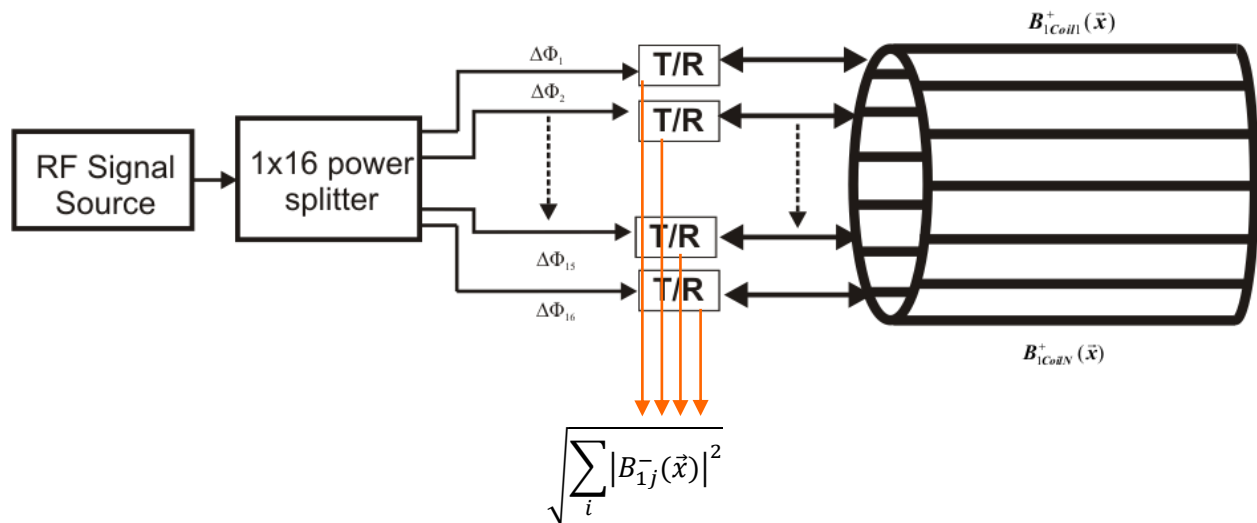
Figure 11: Functional block diagram of a static RF shimming setup for a 16-channel transceiver array.

1.9   Choice of RF coils for ultra-high field

RF coil designs for UHF can be categorized under two main design approaches. These are transceiver array (same coil is used for transmit and receive) and transmit-only receive-only array designs (separate coil arrays for transmit and receive). The table below summarizes the advantages and disadvantages of these two design approaches.

Transceiver Array	Transmit-only Receive-only Array
Tight fitting arrays provide optimum transmit efficiency. The array elements must be tuned and matched for every subject because the elements are closely coupled to the load. Number of channels is limited by the number of transmit channels or power splitter Simpler to construct	Tight fitting receive array inside a large transmit coil provides optimum SNR and parallel imaging performance. Lower transmit efficiency because of the large transmit array. Coil is loosely coupled to the sample and hence does not have to be tuned and matched for every subject. Coil construction is challenging because of the close packaging of transmit and receive array.

1.10 Objective of the thesis

While technical challenges increase substantially with field strength, consequent gains in proton imaging, spectroscopy, functional MRI and multi-nuclei imaging/spectroscopy are significant. A handful of groups worldwide are equipped with magnets stronger than 7 T. World's first 10.5 T magnet has been installed at CMRR in December 2014 and even field strengths as high as 11.7 T are under consideration. Since July 2007, a 9.4 T whole body human scanner and a 16.4 T animal scanner are operational at the high-field MR Center of Max Planck Institute for Biological Cybernetics. For a number of years, both these sophisticated equipments were the strongest MRI magnets worldwide in their respective categories. The excellence of MRI results from these unique scanners depends ultimately on the RF instrumentation, techniques to control the RF field distribution and acquisition methods. The aim of this thesis work is to develop optimized RF coils and front-end RF hardware for spin excitation and signal reception in 9.4 T and 16.4 T MRI scanners.

Chapter 2

RESULTS AND DISCUSSION

2.1 Publication No.1

Design and Evaluation of an RF Front-End for 9.4 T Human MRI

G. Shajan, Jens Hoffmann, Juliane Budde, Gregor Adriany, Kamil Ugurbil and Rolf Pohmann,

Design and Evaluation of an RF Front-End for 9.4 T Human MRI

G. Shajan,[1]* Jens Hoffmann,[1] Juliane Budde,[1] Gregor Adriany,[2] Kamil Ugurbil,[1,2] and Rolf Pohmann[1]

At the field strength of 9.4 T, the highest field currently available for human MRI, the wavelength of the MR signals is significantly shorter than the size of the examined structures. Even more than at 7 T, constructive and destructive interferences cause strong inhomogeneities of the B_1 field produced by a volume coil, causing shading over large parts of the image. Specialized radio frequency hardware and B_1 management methods are required to obtain high-quality images that take full advantage of the high field strength. Here, the design and characteristics of a radio frequency front-end especially developed for proton imaging at 9.4 T are presented. In addition to a 16-channel transceiver array coil, capable of volume transmit mode and independent signal reception, it consists of custom built low noise preamplifiers and TR switches. Destructive interference patterns were eliminated, in virtually the entire brain, using a simple in situ radio frequency phase shimming technique. After mapping the B_1^+ profile of each transmit channel, a numerical algorithm was used to calculate the appropriate transmit phase offsets needed to obtain a homogeneous excitation field over a user defined region. Between two and three phase settings are necessary to obtain homogeneous images over the entire brain. Magn Reson Med 66:596–604, 2011. © 2011 Wiley-Liss, Inc.

Key words: microstrip transmission line; 9.4 T human brain MRI; transceiver array; B_1 shimming

Magnetic resonance imaging research is increasingly moving toward ultra high field (UHF) because of the inherent advantages of higher sensitivity, greater spectroscopic resolution, and improved contrast (1,2). To realize these advantages, the radio frequency (RF) coils and the associated RF hardware, which form the front-end of the imaging system, have to be optimized. However, a number of fundamental issues complicate the design of RF coils for UHF MR systems: the penetration depth of the fields produced by the RF coil is reduced with increasing frequency (3), which causes a decline in sensitivity toward the center of the brain with a multielement receiver coil. Radiation loss in the RF coil increases as roughly the fourth power of the frequency (4,5) and the RF losses to the sample become more prominent at higher frequencies (6). The RF wavelength decreases

with field strength and becomes as low as 10.6 cm inside a human head, considering an average relative permittivity of 50, at the proton Larmor frequency of 400 MHz at 9.4 T. As this is comparable to or smaller than the dimension of the human head, the B_1 field inside the sample exhibits attenuated traveling wave behavior (7).

The radiation loss of a coil can be significantly reduced by RF shielding or by introducing a ground plane as part of the resonant structure. Microstrip transmission line (MTL) elements consisting of a thin strip and a ground plane separated by a low loss dielectric have been efficiently implemented for MR imaging at UHF (8–13). Although the RF loss to the sample tissue is unavoidable, it can be minimized by matching the coil size to the desired field of view (FOV).

The B_1 profile of a circularly polarized field that is homogeneous in the unloaded coil becomes highly inhomogeneous in the loaded case with constructively interfering B_1^+ fields in the center of the brain and signal attenuation and even voids due to destructive interferences (14,15) in the periphery. Transceiver array coils are well suited for tackling RF inhomogeneity problems by avoiding destructive interferences during reception while offering the possibility to alter the waveforms on the individual array elements during transmission. Even if an array of independent RF transmitters is not available, simply splitting a single RF waveform and exciting the array elements with different amplitudes and global phase shifts adds several degrees of freedom that allow for optimizing the B_1^+ field over the subject (11,15,16). Here, static B_1^+ phase shimming was performed by changing the length of the coaxial cables that connect the RF power source to the individual array elements. Further benefits that would be gained by the additional control of the current amplitude on the individual coil elements or by utilizing tailored B_1 shimming, i.e., multidimensional RF pulses accelerated with parallel transmission, could not be realized.

In this article, we describe the design of a capacitively decoupled 16-element transceiver array and evaluate its noise correlation and the spatial distribution of its B_1^+ field at 9.4 T. Furthermore, additional RF hardware needed for independent transmission and reception on 16 channels was developed. To obtain homogeneous excitation over larger regions of the brain, the B_1^+ field distribution is mapped for each transmit channel, and a set of transmit phase offsets that optimizes the B_1^+ field over a user-defined region of interest is calculated. Using two to three different transmit phase configurations, signal voids due to destructive interference could be eliminated

[1]High-Field Magnetic Resonance Center, Max Planck Institute for Biological Cybernetics, Tuebingen, Germany.

[2]Department of Radiology, Center for Magnetic Resonance Research, University of Minnesota Medical School, Minneapolis, Minnesota, USA.

*Correspondence to: G. Shajan, M.E. High Field Magnetic Resonance Center, MPI for Biological Cybernetics, Spemanstrasse 41, 72076 Tuebingen, Germany. E-mail: shajan.gunamony@tuebingen.mpg.de
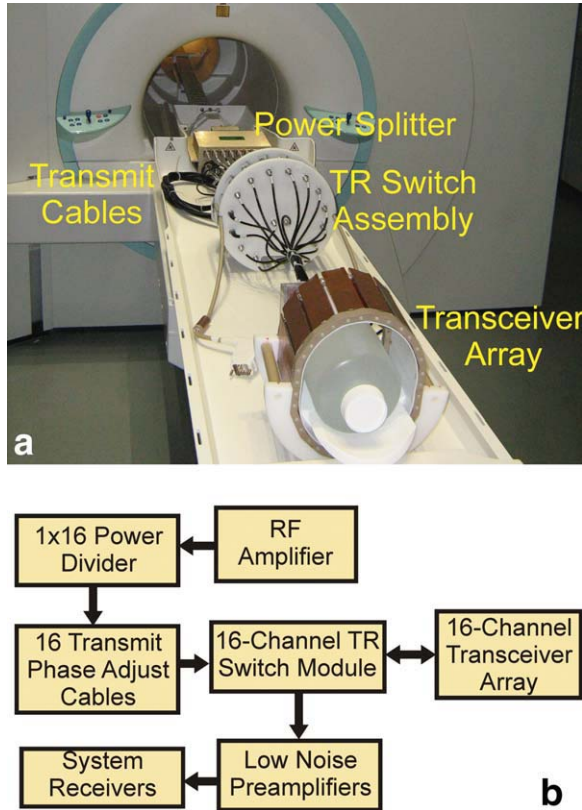
FIG. 1. **a**: RF front-end for 9.4 T human MRI, consisting of a 16-channel transceiver array prototype, a 16-channel TR switch module assembly, and a 1 × 16 power splitter. **b**: Block diagram of the experimental setup. [Color figure can be viewed in the online issue, which is available at wileyonlinelibrary.com.]

as is demonstrated on three different volunteers. Thus, we present a complete RF-setup and a phase shimming technique to demonstrate the feasibility of MR imaging of the human brain at the field strength of 9.4 T.

MATERIALS AND METHODS

Instrumentation and Setup

The hardware was developed for an MR scanner manufactured by Siemens (Siemens Medical Solutions, Erlangen, Germany), interfaced to a 9.4 T whole body magnet with a length of 3.67 m and a bore size of 82 cm. It is fitted with a head gradient with a maximum gradient strength of 60 mT/m, a slew rate of 400 T/m/s, and an inner diameter of 32 cm. The system has 32-receive channels and a 7.5 kW Dressler (Advanced Energy Industries Inc. CO, USA) RF amplifier.

A block diagram and a photograph of the developed measurement setup are shown in Fig. 1. The transmit RF power is split into 16 equally phased components using a 1 × 16 power splitter (Werlatone, Brewster, NY, USA) with an insertion loss of −0.38 dB and a phase variation of ±6° per path. The output of the power splitter is connected to the individual coil elements through a dedicated TR switch module. The transmit phase is adjusted by varying the length of the coaxial cable between the power splitter and the TR switch.

The 16 TR switch modules are assembled on to a circular holder as shown in Fig. 1. The cable length from the coil to the TR switch was chosen in such a way that the assembly is outside the gradient coil when the RF coil is placed in the isocenter of the magnet. Bench measurements were performed using a calibrated Agilent Technologies Inc. (Santa Clara, CA, USA) 4396B network analyzer together with an 85046A S-parameter test set.

We imaged healthy volunteers who had signed a written consent form approved by the Institutional Review Board of the University of Tübingen.

Coil Construction

The coil construction was based on the MTL design originally developed for 7 T (11). The major design considerations in the construction of such a coil are the selection of design parameters for the individual coil elements, the total number of elements, and the coil dimensions. The material and thickness of the substrate and the width and length of the microstrip line define the performance of a coil element (12,17). Polytetrafluoroethylene (PTFE, commonly known as Teflon) with a relative dielectric constant ε_r of 2.1 was used as the substrate because of its low loss tangent δ. Assuming quasi-TEM mode of propagation, the wavelength in the microstrip line is given by $\lambda = \lambda_0/\sqrt{\varepsilon_{ff}}$, where λ_0 is the free space wavelength and ε_{ff} is the effective relative dielectric constant (10). With capacitive termination of 1.5 pF at both the ends of the MTL, the 14-cm long MTL forms a $\lambda/2$ resonator at the Larmor frequency.

Adhesive backed copper tapes (3M, St Paul, MN, USA) were used for the strip and the ground plane of the microstrip. Both the substrate thickness and the width of the strip were 12.5 mm. The input circuit in Fig. 2 consists of a trimmer capacitor C_T (52H02, Johanson Manufacturing corp., NJ, USA) to tune the coil element to the Larmor frequency and an impedance matching section with a 1.5 pF fixed capacitor in series and a trimmer capacitor C_M connected in shunt. The input circuit is assembled on a single-sided FR4 circuit board, which is fitted in a pocket created in the Teflon block. The ground shielding is extended on to the side walls up to 10 mm (18), improving the adjacent element decoupling by at least 2 dB. Along the length of the coil element, the ground shielding extends up to the end of the circuit board. To avoid shifts in the coil's resonance frequency caused by the RF shield of the head gradient system when the coil is placed in the isocenter of the magnet, the input circuit and the side walls are shielded.

Sixteen identical Teflon blocks of 42 mm width were fabricated and placed on a holder to form an elliptical coil with inner dimensions of 20.5 cm along the minor axis and 28 cm along the major axis. A 2-mm thick Teflon sheet is wrapped along the inner volume of the coil to isolate the subject from the conducting strips.

The tight placement of the MTL elements around the coil geometry causes electromagnetic coupling between adjacent coil elements. The scattering parameter S_{21}, determined with the network analyzer, is a measure of this coupling. In the absence of any decoupling
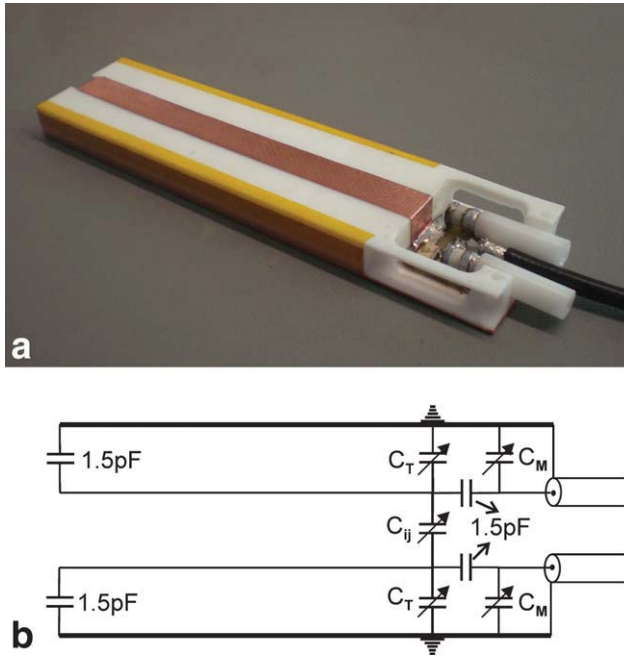
FIG. 2. **a**: Implementation of the 14-cm long microstrip element with shielding extended to the side walls of the substrate material and the assembled input circuit. **b**: Equivalent circuit of two adjacent coil elements and the decoupling capacitor C_{ij}. During installation, C_{ij} is set to the value that offers maximum decoupling. [Color figure can be viewed in the online issue, which is available at wileyonlinelibrary.com.]

mechanism, it is about -5 dB. Among the several decoupling options available, the capacitive decoupling technique is most suitable for UHF MTL coils. A variable capacitor (C_{ij}) was connected between the input circuits of the adjacent coil elements to attain sufficient decoupling and to enable independently tuned and matched coil elements (19). The decoupling trimmer capacitors were adjusted during installation to the value that offers maximum decoupling and do not need to be adjusted for different subjects. Approximately 1 to 1.5 pF was required to decouple the adjacent elements depending on their location in the coil array. RG223 flexible coaxial cables (Huber + Suhner AG, Switzerland) attached to each of the coil elements were bunched tightly, and the ground conductors of the 16 cables are shorted together (see Fig. 4b). The coil assembly is mounted on a patient table extension such that the coil center can be positioned in the magnet isocenter.

TR Switch Module

The transmit and receive functions are separated by appropriately biasing the PIN diodes in the TR Switch. Apart from protecting the receive preamplifier from high power transmit RF, the TR switch prevents noise coupling from the transmit to the receive path (20).

The circuit diagram of the TR switch module is shown in Fig. 3a. Shunt-mounted diodes provide higher isolation, whereas series-connected diodes are commonly used when minimum insertion loss is required. The

receive path has a single PIN diode (UM4001B, Microsemi Corporation, Irvine, CA, USA) in shunt along with a 90° Π network. During the excitation pulse, a 100 mA current turns the diodes ON. The diode D_1 is pulled to ground through capacitor C_s. This creates an open circuit at the Larmor frequency in the receive path, thus protecting the preamplifier from the transmit RF. The diodes are turned OFF during signal acquisition. The overall electrical length of the receive path is 180°, and hence, the input impedance of the preamplifier is seen at the "Coil" port of the TR switch when looking into the TR switch from the coil side.

The two series-connected diodes in the transmit path, each providing at least -20 dB of isolation when turned OFF, prevent noise coupling from transmit to receive path. The high power PIN diodes have a higher capacitance C_T. A series LC network is connected across the PIN diode to resonate across C_T in the reverse bias condition. S_{21} is measured across the reverse biased diode, and the values of L_1 and C_1 are chosen to maximize the isolation across the diode terminals. A Π section is added to adjust for impedance mismatch (Transmit ON condition) in the transmit path.

Low Noise Preamplifier

Low input impedance preamplifiers (21,22) have been widely used for signal amplification in the receive path. A two stage amplifier in cascode configuration, as shown in Fig. 3b, consisting of a pHEMT (ATF35143, Avago
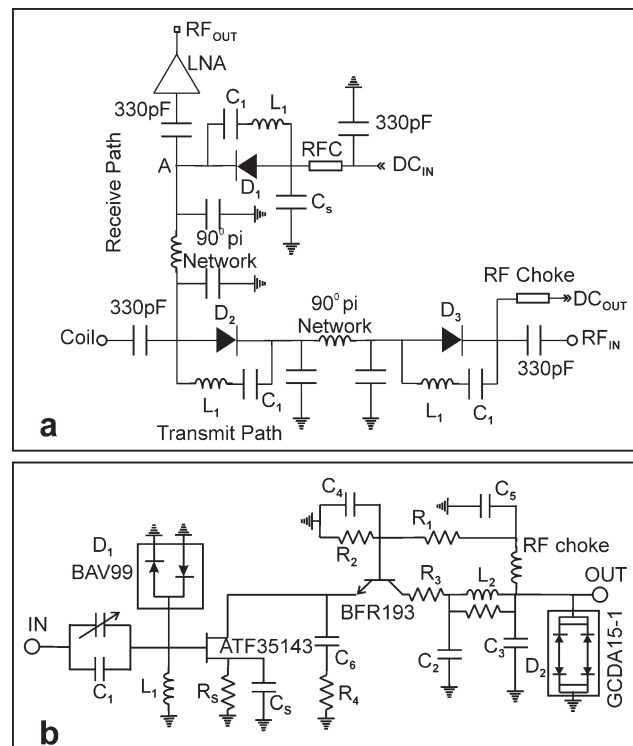

FIG. 3. **a**: Schematic diagram of the 9.4 T TR switch. The port RF$_{IN}$ is connected to the output of the power splitter, and the preamplifier output RF$_{OUT}$ is connected to the system receivers. **b**: Schematic diagram of the 9.4 T preamplifier. D_1 and D_2 are protection diodes. ATF35143 and BFR193 are the active devices.

Technologies, San Jose, CA, USA) in common source mode followed by a BJT (BFR193, Infineon Technologies, Milpitas, CA, USA) in common base (CB) mode was designed. This combination exploits the most desirable characteristics of each device, such as the very large input resistance of the pHEMT and the large voltage gain of the BJT. Furthermore, the CB stage short-circuits the Miller capacitor (C_μ), because one side of C_μ is connected to ground (23,24).

The input circuit consists of a series capacitor and an inductor in shunt (22), with values such that it is resonant at 400 MHz. Because of the high input impedance of the active device, the input impedance of the preamplifier is dominated by the impedance of this series resonant LC network. The pHEMT is self biased thus allowing the use of a single polarity power supply (25). A DC supply of 10 V is available at the RF contacts of the Siemens coil plugs for biasing the preamplifier. The drain current I_D is set to 15 mA by adjusting R_s, a potentiometer in parallel with a chip resistor (BREL international, FL, USA). The Π network at the output forms the output matching network.

For tighter dielectric tolerance of the substrate and lower loss at high frequency, RO4003C laminate (Rogers Corporation, AZ, USA) was used for the fabrication of the TR switch and preamplifier circuit boards.

B_1 Calibration

We performed slice-selective B_1 shimming (26) by changing the length of the cables between the output of the power divider and the coil array. By doing so, the relative phases with which the currents on the individual elements are oscillating can be varied. This variation, in turn, alters the B_1^+ field produced by the coil over the subject. Therefore, 16 cables of adequate length, each introducing a phase offset between 0° and 360° must be chosen such that a strong and uniform B_1^+ field in a desired region within the brain is produced. We derive the optimal cable lengths from an offline calculation based on single-channel B_1^+ magnitude (27) and phase maps (16) as described below:

The total B_1^+ field produced by the coil array in the subject is given by complex addition of the single-channel fields $B_{1,k}^+$:

$$\left|B_1^+(\vec{x})\right| = \left|\sum_{k=1}^{16} \left|B_{1,k}^+(\vec{x})\right| \cdot \exp[i(\Psi_k(\vec{x}) - \Theta_k)]\right|. \qquad [1]$$

Ψ_k denotes the position-dependent relative phase of the $B_{1,k}^+$ field, while Θ_k is a global phase offset introduced by a coaxial cable of specific length that connects the power divider to the coil element k. To perform B_1^+ shimming in situ, one needs to map the subject-dependent B_1^+ magnitude and phase of every single channel in a short time and under stringent RF power limitations. We found that a rapid and simple field estimation technique introduced recently (27) works well for the purpose of RF shimming. A set of low flip angle FLASH images (FOV = 230 mm, TR = 100 msec, TE = 4.12 msec, acquisition matrix = 128 × 128, 6-mm slice thickness) was acquired by transmitting the RF power directly through

only one array element at a time with a fixed cable length, e.g., $\Theta_k = 0$. The signal was always sampled on all 16 elements, which resulted in 256 magnitude images $|S_{k,j}|$ and the associated 256 phase images $\varphi_{k,j}$, where the index k describes the transmitting and the index j the receiving channel.

Relative single-channel field magnitude maps $B_{1,k}^+$ can be estimated from the magnitude images according to the method described in (27):

$$\left|B_{1,k}^+(\vec{x})\right| \approx \frac{\sum_{j=1}^{16}\left|S_{k,j}(\vec{x})\right|}{\sqrt{\sum_{k,j=1}^{16}\left|S_{k,j}(\vec{x})\right|}}. \qquad [2]$$

The raw phase images $\varphi_{k,j}$ contain phase contributions from the B_1^+ field but are also caused by the ≈reception of the signal and other sources which are equal in all images (16,27). By calculating the phase relative to a reference channel (e.g., channel 1), these phase contributions can be removed (16):

$$\Psi_k(\vec{x}) = \arg\left(\sum_{j=1}^{16}\exp\left[i\left(\varphi_{k,j}(\vec{x}) - \varphi_{1,j}(\vec{x})\right)\right]\right) \qquad [3]$$

With the relative field and phase maps, a prediction of the combined B_1^+ field magnitude in dependence of arbitrarily chosen cable lengths (global phase offsets Θ_k) can be calculated offline using Eq. 1. To find an optimized set of cable lengths, a GUI was written in MATLAB (The MathWorks Inc., Natick, MA), in which the user can specify a region within the slice in which the B_1^+ field is desired to be shaped according to a predefined criterion. Only the field magnitude is considered, allowing an arbitrary spatial distribution of the resulting B_1^+ phase. This provides more degrees of freedom for the field magnitude optimization but introduces a nonlinear problem. Hence, a simulated annealing (28) algorithm iteratively changes the phase offsets Θ_k and calculates the predicted total B_1^+ field to minimize a given cost function. For example, if field homogeneity is the main purpose of shimming, the standard deviation of all pixels from a given target flip angle can be minimized. However, this approach results in increased power requirements. If the prevention of signal cancellations is demanded, regardless of field homogeneity, the inverse of the minimum field value in the slice is a reasonable and power efficient choice.

RESULTS AND DISCUSSION

TR Switch Module

The properties of the 16 identical TR-switch/preamplifier modules designed here were measured as:

Gain: 30 dB

Noise Figure: 1.25 dB (Preamplifier + TR switch)

Output to input isolation: −47 dB

The isolation provided by the preamplifier protection circuit in the receive path during transmit ON is −49 dB at the Larmor frequency. The isolation in the transmit path is −42 dB during signal acquisition; the two series
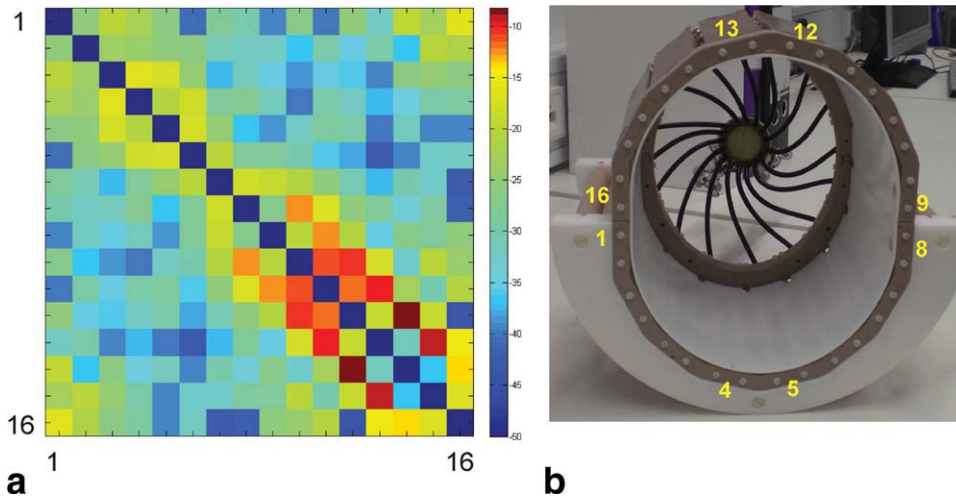
FIG. 4. **a**: The noise correlation matrix in dB scale. The coil element number is indicated along the axis. **b**: A picture of the transceiver array with the element numbers marked with reference to the noise correlation plot.

diodes provide a more broadband response when compared to the shunt mounted diode performance.

Coil Decoupling/Noise Correlation

The input return loss of the coil elements was adjusted to better than -25 dB for every subject. The isolation provided by the decoupling capacitor eliminates peak splitting, and a single resonance was seen for each coil element. Unloaded, the strongest coupling was observed between the next nearest elements. Although additional decoupling strategies, like preamplifier decoupling (22) or capacitive decoupling between the next nearest elements might be used to reduce next-neighbor coupling, no such measures were required when the coil was loaded with either a cylindrical phantom (3 L, 100 mM saline) or a human head, as this dampened the next nearest element coupling considerably. Using the coil with minimal loading, however, would require additional steps to sufficiently suppress element coupling.

As observed earlier at 7 T (11,18), the coil decoupling performance was highly sensitive to the presence of the load. This was even more severe at 9.4 T, as evident

from the noise correlation plot in Fig. 4. The filling factor especially near the elements 11, 12, 13, and 14 at the top of the coil is smaller than that of the other elements of the coil, limiting the nearest neighbor element decoupling to about -10 dB. This is caused by the shape of the human head, which requires a larger distance between brain and coil to make space for the nose. Shortening elements 12 and 13 might make it possible to increase the filling factor, and thus the decoupling, by moving the coil elements closer to the head. The other coil elements that are strongly coupled to the load exhibit better decoupling performance and hence support tight fitting coils for better transmit efficiency and improved signal to noise ratio.

Adjustment of the coil parameters is performed for each subject with a focus on optimizing the receive performance. While any two adjacent elements were connected to the network analyzer for tuning and matching, the remaining coil elements were connected to the individual TR switches thereby simulating the receive condition. Even though the transmit mode was not adjusted separately, the transmit efficiency was not compromised,
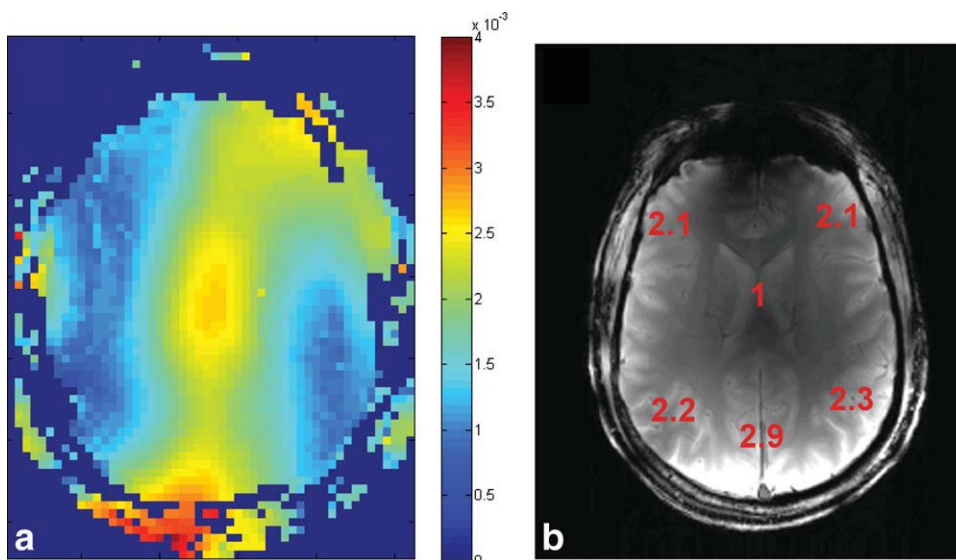

FIG. 5. **a**: B_1^+ field map obtained as per the procedure given in (1). **b**: Spatial distribution of SNR normalized with reference to the ROI in the center. For the SNR scan, the RF power required to produce a $90°$ flip angle in the center of the slice was determined. The dark shading at the top is due to B_0 artifact.
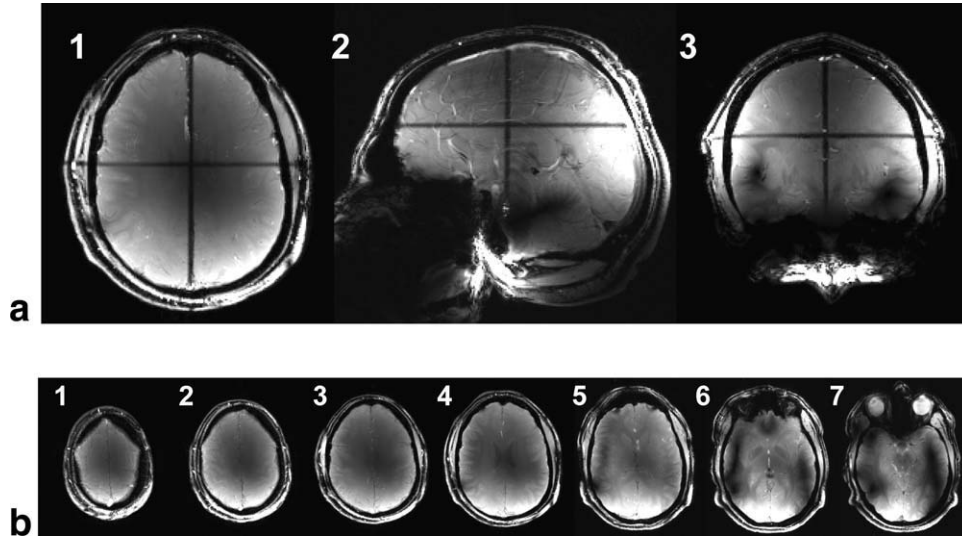
FIG. 6. **a**: FLASH images demonstrating the coil coverage in the "standard" quadrature transmit phase configuration in axial (1), sagittal (2), and coronal (3) plane. The crosshairs in each image reference the slice location of the other two planes. Imaging parameters: FOV: 250 mm, slice thickness: 3 mm, TE: 4.6 msec, TR: 40 msec, matrix: 256 × 256. **b**: Multiple axial slices acquired in the same session. Signal voids due to destructive interference appear from slice 4 and are highly prominent in slices 6 and 7.

each coil element having an input return loss of −24 dB or better and a maximum change in the adjacent element decoupling of 2.2 dB under the transmit condition. This was verified with 50 Ω load terminations on all the coil elements.

B_1 Profile, Signal-to-Noise Ratio, and Coil Coverage

For these measurements, the "standard" phase configuration that sets up a circular polarization with an incremental transmit phase offset of ~22.5° between successive coil elements was used. The spatial distribution of the B_1^+ field generated by the transceiver array in the volume coil transmit mode was mapped at 9.4 T using magnetization preparation followed by gradient recalled echo imaging as explained in (1,29). The result is shown in Fig. 5a. The images were acquired in the axial plane through the center of the brain. The elements directly below the head, especially 4 and 5, produced the strongest local fields. The characteristic bright region exhibited by T/R volume coils in the center of the coil due to constructive interference was observed. The dark areas at the outer regions of the brain are considerably larger than at 7 T (11), illustrating the increased importance of strategies for improving homogeneity.

Using the RF pulse calibration method explained in (1), the RF power required to produce a 90° flip angle at the center of the selected axial slice was estimated. Gradient-echo images with the following parameters were acquired: FOV: 24 cm, matrix size: 256 × 256, slice thickness: 5 mm, TE = 6.1 msec, and TR = 5000 msec. Circular regions of interest of equal size were selected on six locations across the image as shown in Fig. 5b. The signal-to-noise ratio (SNR) was determined by dividing the mean signal value by the standard deviation of the background noise. The SNR values were normalized with respect to the region of interest in the center. The SNR performance is qualitatively similar to that of a

receive-only surface coil array with the maximum SNR closest to the coils.

For all measurements on humans, the subjects were positioned supinely inside the coil with the tip of the nose at the level of the outer edge of the coil housing. Figure 6a shows FLASH images in the three imaging planes illustrating the extent of the coil coverage. The sagittal slice shows whole brain coverage, which includes regions outside the coil (cerebellum) that are excited due to wave propagation effects.

The "standard" transmit phase configuration produced a characteristic field pattern in the human brain reproducible on different volunteers. The axial images of the upper brain are free of signal voids as shown in Fig. 6b. Two dark arcs begin to appear from the center axial slices and deepen toward the slices in the lower brain in the region of the temporal lobes (see slices 6 and 7 of Fig. 6b). These signal voids arise from a very weak B_1^+ field in regions, where the individual magnetic fields from the array elements interfere destructively. Because
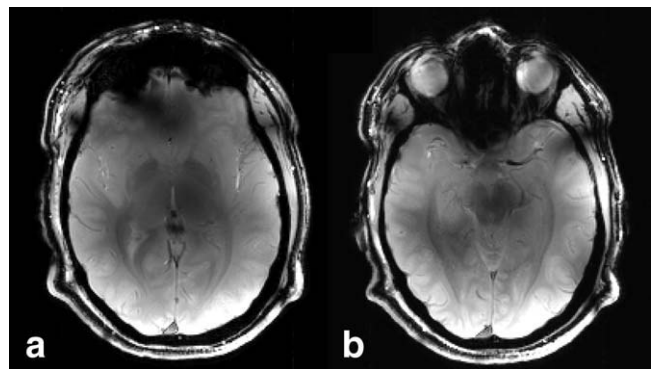

FIG. 7. The influence of phase optimization: (**a**) and (**b**) are B_1-shimmed FLASH images that correspond to slices 6 and 7 of Figure 6b.
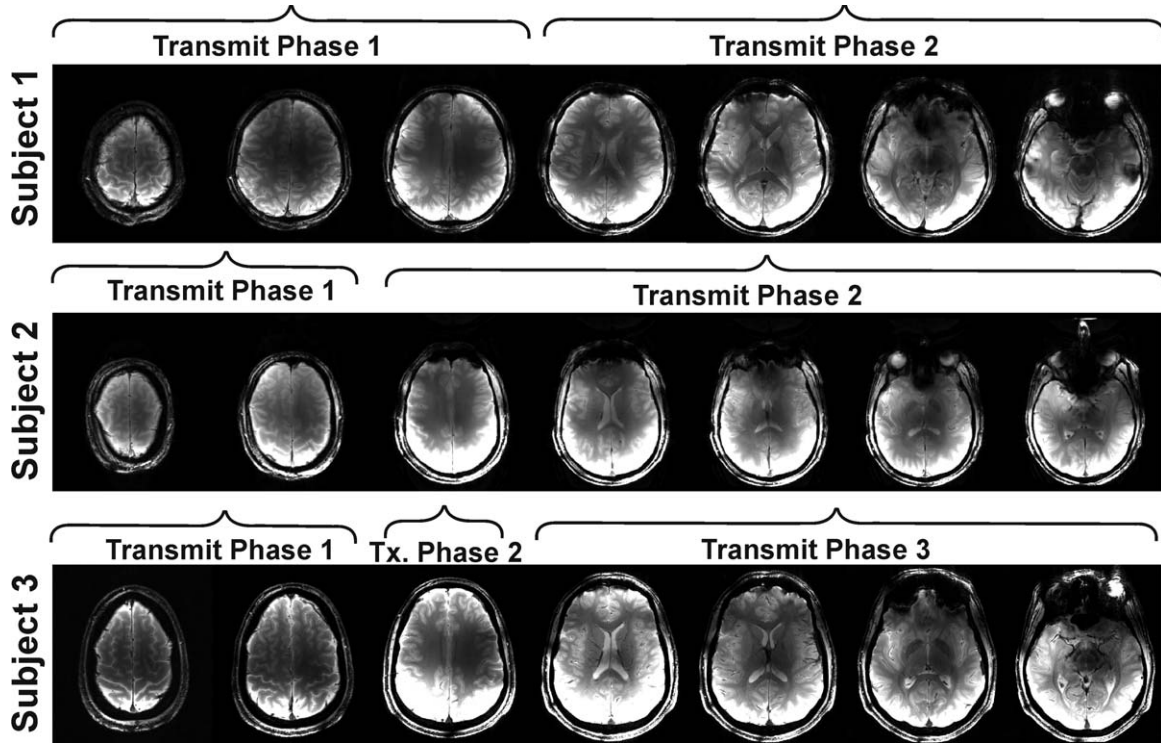
FIG. 8. The transmit phase optimization routine was verified on three different subjects. The phase offsets are tabulated in Table 1. Because of the increased sample–coil interaction, different shim solutions are needed for different subjects.

of the symmetry of the coil elements and the human head, the fields typically form a pattern with constructive interference on the coil's axis of symmetry and destructive interference in a ring-shaped region around it. We observe two dark arcs because the symmetry of the human head is more pronounced in the left-right direction than in the anterior-posterior direction. In addition, the effect is intensified in slices from the level of the eyes and downward probably because of the larger sample dimensions in the lower slices.

RF Shimming

To demonstrate the capability of the simple RF phase shimming method, the B_1^+ field was optimized for the lower portion of the volunteer's brain where the most severe signal dropouts could be observed in the standard quadrature phase configuration. Relative single-channel field and phase maps were acquired in the axial slice 6 shown in Fig. 6b and the numeric algorithm searched for the phase configuration which maximized the minimum field value in the brain to prevent signal voids.

The FLASH images shown in Fig. 7 correspond to slices 6 and 7 in Fig. 6b and were acquired with the same imaging parameters, but the phase cables were plugged according to the calculated configuration. A considerable improvement in image quality can be observed in the selected slice (Fig. 7a) and in the adjacent one (Fig. 7b) compared to the standard phase configuration.

Table 1

Transmit Phase Delay on Each of the Coil Elements for the Measurements Shown on Fig. 8

		Ch-1	Ch-2	Ch-3	Ch-4	Ch-5	Ch-6	Ch-7	Ch-8	Ch-9	Ch-10	Ch-11	Ch 12	Ch-13	Ch-14	Ch-15	Ch-16
Subject 1	Transmit Phase 1	291	190	74	102	47	102	139	194	226	213	262	270	273	213	0	0
	Transmit Phase 2	202	164	113	46	0	29	54	118	119	181	167	238	228	188	154	211
Subject 2	Transmit Phase 1	0	20	43	67	90	114	132	160	181	201	226	248	273	294	313	343
	Transmit Phase 2	124	89	78	18	0	29	60	108	87	140	99	176	195	102	92	163
Subject 3	Transmit Phase 1	0	20	43	67	90	114	132	160	181	201	226	248	273	294	313	343
	Transmit Phase 2	0	47	82	71	59	117	196	141	64	326	261	252	262	270	282	330
	Transmit Phase 3	121	124	85	18	0	29	54	90	91	117	123	225	140	112	104	135

The tabulated values are actual phase delays on each of the coil elements after correcting for the power splitter and coaxial cable errors.

Furthermore, less power was needed to reach the same mean flip angle. This is a consequence of the utilized cost function which favors shim solutions that are not particularly homogeneous, but which are free of field cancellations and are power efficient. Reducing the power requirements was found to be possible in low axial slices where the standard configuration is not effective.

In principle, the utilized RF shimming method is able to remove signal voids due to B_1^+ destructive interferences in any localized region within any slice covered by the coil array when the individual coil elements are driven with optimized phase offsets. The quality of the shim, i.e., the strength and homogeneity of the B_1^+ field, increases as the spatial dimension of the region chosen for optimization is reduced. Also, a phase configuration optimized for B_1^+ homogeneity through the lower brain was always found to be unsatisfactory in axial slices through the top-brain region.

In our experience, the total imaging volume inside the coil can be covered in two to three different phase configurations without noticeable signal voids. The length of coverage in the longitudinal direction is limited by the positioning of the head in the coil and also by the weaker field toward the end of the microstrip coil elements. Figure 8 presents multiple FLASH images acquired on three different subjects with either two (Row 1 and 2) or three (Row 3) phase configurations. These images are not intensity corrected but have different window levels. The delay in phase introduced using coaxial cables on each coil element is summarized in Table 1. The shading seen on the parasinus and temporal lobe regions in the inferior slices is due to B_0-inhomogeneities caused by susceptibility differences. In addition, we found that separate shim configurations had to be calculated for the different subjects because of their diverse head shapes and variations in their position.

CONCLUSIONS

Even more than at 7 T, MR imaging at a magnetic field strength of 9.4 T requires new approaches to solve the problems connected to the high field. The potential advantages of UHF-MR will only be realized by using an optimized RF setup. Here, we presented and characterized an RF-front-end, tailor-made for imaging at 9.4 T, consisting of a 16-channel transceiver array and a TR-switch module with integrated low-noise preamplifier. In addition, we have shown that using subject dependent B_1 phase shimming with a 16-channel array, considerable mitigation of B_1 inhomogeneity is feasible in the brain even at this high field strength. This enables us to take advantage of the potential of UHF-imaging, as shown in a comparison to 3 T (30,31). The high B_1 homogeneity and SNR obtained in this study show the validity of the MTL transceiver array approach for 9.4 T, generating a volume coil type transmit mode and a multichannel receive array, combined with RF-shimming to avoid wavelength effects. On the other hand, our results also highlight the increasing challenges with the higher field even compared to 7 T, manifest in the larger B_1-variations in the circularly polarized field, the stronger cou-

pling between the elements and the more difficult B_1-shimming, requiring more than one phase setting for whole-brain coverage. The excellent results obtained with the presented setup (30,31) show that overcoming these difficulties is possible with the current approach.

REFERENCES

1. Vaughan JT, Garwood M, Collins CM, Liu W, DelaBarre L, Adriany G, Anderson P, Merkle H, Goebel R, Smith MB, Ugurbil K. 7T vs. 4T: RF power, homogeneity and signal-to-noise comparison in head images. Magn Reson Med 2001;46:24–30.
2. Ugurbil K, Hu X, Chen W, Zhu XH, Kim SG, Georgopoulos A. Functional mapping in the human brain using high magnetic fields. Phil Trans R Soc Lond B 1999;354:1195–1213.
3. Yang QX, Wang J, Collins CM, Smith MB, Zhang X, Ugurbil K, Chen W. Phantom design method for high field MRI human systems. Magn Reson Med 2004;52:1016–1020.
4. Ong KC, Wen H, Chesnick AS, Duewell S, Jaffer FA, Balaban RS. Radiofrequency shielding of surface coils at 4.0T. JMRI 1995;5:773–777.
5. Harpen MD. Radiative losses of a birdcage resonator. Magn Reson Med 1993;29:713–716
6. Collins CM, Li S, Smith MB. SAR and B1 field distributions in a heterogeneous human head model within a birdcage coil. Magn Reson Med 1998;40:847–856.
7. Yang QX, Wang J, Zhang X, Collins CM, Smith MB, Liu H, Zhu X, Vaughan JT, Ugurbil K, Chen W. Analysis of wave behavior in lossy dielectric samples at high field. Magn Reson Med 2002;47:982–989.
8. Lee RF, Westgate CR, Weiss RG, Newman DC, Bottomley PA. Planar strip array (PSA) for MRI. Magn Reson Med 2001;45:673–683.
9. Lee RF, Hardy CJ, Sodickson DK, Bottomley PA. Lumped-element planar strip array (LPSA) for parallel MRI. Magn Reson Med 2004;51:172–183.
10. Zhang X, Ugurbil K, Sainati R, Chen W. An inverted microstrip resonator for human head proton MR imaging at 7 Tesla. IEEE Trans Biomed Eng 2005;52:495–504.
11. Adriany G, Van de Moortele PF, Wiesinger F, Moeller S, Strupp JP, Anderson P, Snyder C, Zhang X, Chen W, Pruessmann KP, Boesiger P, Vaughan JT, Ugurbil K. Transmit and receive transmission line arrays for 7 Tesla parallel imaging, Magn Reson Med 2005;53:434–445.
12. Zhang X, Ugurbil K, Chen W. A microstrip transmission line volume coil for human head MR imaging at 4T. J Magn Reson 2003;161:242–251.
13. Zhang X, Ugurbil K, Chen W. Microstrip RF surface coil design for extremely high-field MRI and spectroscopy. Magn Reson Med 2001;46:443–450.
14. Vaughan JT, DelaBarre L, Snyder C, Tian J, Akgun C, Shrivastava D, Liu W, Olson C, Adriany G, Strupp J, Anderson P, Gopinath A, Van de Moortele PF, Garwood M, Ugurbil K. 9.4T Human MRI: preliminary results. Magn Reson Med 2006;56:1274–1282.
15. Van de Moortele PF, Akgun C, Adriany G, Moeller S, Ritter J, Collins CM, Smith MB, Vaughan JT, Ugurbil K. B1 Destructive interferences and spatial phase patterns at 7T with a head transceiver array coil. Magn Reson Med 2005;54:1503–1518.
16. Metzger GJ, Snyder C, Akgun C, Vaughan JT, Ugurbil K, Van de Moortele PF. Local shimming for prostate imaging with transceiver arrays at 7T based on subject-dependent transmit phase measurements. Magn Reson Med 2008;59:396–409.
17. Kumar A, Bottomley PA. Optimizing the intrinsic signal-to-noise ratio of MRI strip detectors. Magn Reson Med 2006;56:157–166.
18. Adriany G, Van de Moortele PF, Ritter J, Moeller S, Auerbach EJ, Akgün C, Snyder CJ, Vaughan JT, Ugurbil K. A Geometrically adjustable 16-channel transmit/receive transmission line array for improved RF efficiency and parallel imaging performance at 7 Tesla. Magn Reson Med 2008;59:590–597.
19. Lian J, Roemer PB. MRI RF coil. U.S. Pat. 5,804,969, 1998.
20. Yang X, Zheng T, Fujita H. T/R Switches, Baluns and detuning elements in MRI RF Coils. ISMRM Fourteenth Scientific Meeting Weekend Syllabus, Seattle, Washington, USA, 2006.
21. Mueller OM, Edelstein WA. Gallium-Arsenide MOSFETs for noise reduction in MR systems. Proceedings of the 6th Annual Meeting of SMRM, New York City, USA, 1987. p 411.
22. Roemer PB, Edelstein WA, Hayes CE, Souza SP, Mueller OM. The NMR phased array. Magn Reson Med 1990;16:192–225.

23. Scott GC. Preamps: analysis, noise and stability. ISMRM 17th Scientific Meeting Weekend Syllabus, Honolulu, Hawaii, USA, 2009.

24. Lee TH. Planar microwave engineering: a practical guide to theory, measurements and circuits. Cambridge University Press, Cambridge, UK; pp 369–471.

25. Low Noise Amplifiers for 1600 MHz and 1900 MHz Low Current Self-biased Applications using the ATF-35143 Low Noise PHEMT: Application Note 1174, Avago Technologies, San Jose, CA, USA.

26. Hoffmann J, Budde JS, Shajan G, Pohmann R. Slice-selective B1 phase shimming at 9.4T. Proceedings of the 18th Annual Meeting of ISMRM, Stockholm, Sweeden, 2010. p 1470.

27. Van de Moortele PF, Ugurbil K. Very fast multi channel B1 calibration at high field in the small flip angle regime. Proceedings of the 17th Annual Meeting of ISMRM, Honolulu, Hawaii, USA, 2009. p 367.

28. S. Kirkpatrick. Optimization by simulated annealing. Science 1983; 220:671–680.

29. Klose U, Mapping of the radio frequency magnetic field with a MR snapshot FLASH technique. Med Phys 1992;19:1099–1105.

30. Budde JS, Pohmann R, Shajan G, Ugurbil K. Susceptibility weighted imaging of the human brain at 9.4T. Proceedings of the 17th Annual Meeting of ISMRM, Honolulu, Hawaii, USA, 2009. p 43.

31. Budde JS, Shajan G, Hoffmann J, Ugurbil K, Pohmann R. Human imaging at 9.4T using T2*, phase and susceptibility weighted contrast. Magn Reson Med 2010; ePub ahead. DOI: 10.1002/MRM.22632

2.2 Publication No 2

A 16-Channel Dual-Row Transmit Array in Combination with a 31-Element Receive Array for Human Brain Imaging at 9.4 T

G. Shajan, Mikhail Kozlov, Jens Hoffmann, Robert Turner, Klaus Scheffler and Rolf Pohmann,

A 16-Channel Dual-Row Transmit Array in Combination with a 31-Element Receive Array for Human Brain Imaging at 9.4 T

G. Shajan,[1]* Mikhail Kozlov,[2] Jens Hoffmann,[1] Robert Turner,[2] Klaus Scheffler,[1,3] and Rolf Pohmann[1]

Purpose: Arranging transmit array elements in multiple rows provides an additional degree of freedom to correct B_1^+ field inhomogeneities and to achieve whole-brain excitation at ultra-high field strengths. Receive arrays shaped to the contours of the anatomy increase the signal-to-noise ratio of the image. In this work, the advantages offered by the transmit and receive array techniques are combined for human brain imaging at 9.4 T.

Methods: A 16-element dual-row transmit array and a 31-element receive array were developed. Based on an accurate numerical model of the transmit array, the deposited power was calculated for different head sizes and positions. The influence of the receive array on the transmit field was characterized. Parallel imaging performance and signal-to-noise ratio of the receive array were evaluated.

Results: On average, a two fold increase in signal-to-noise ratio was observed in the whole-brain volume when compared with a 16-channel elliptic microstrip transceiver array. The benefits of combining the two arrays, B_1^+ shimming in three directions and high receive sensitivity, are demonstrated with high-resolution in vivo images.

Conclusion: The dual-row transmit array provides whole-brain coverage at 9.4 T, which, in combination with the helmet-shaped receive array, is a valuable radio frequency configuration for ultra-high field magnetic resonance imaging of the human brain. **Magn Reson Med 71:870–879, 2014. © 2013 Wiley Periodicals, Inc.**

Key words: transmit array; receive array; 9.4 T

INTRODUCTION

Remarkable progress has been made in addressing radio frequency (RF)-related challenges in magnetic resonance imaging (MRI) at ultra-high field (UHF) (1–3). An array of transmit elements is an essential tool to mitigate transmit field (B_1^+) inhomogeneities caused by the shorter wavelength in tissue, because it offers the flexibility to independently influence the amplitude and phase of the current in the individual coil elements. A variety of transceiver array designs, with coil elements arranged in single row or multiple rows, has been proposed for human brain imaging at 7 T and above (4–10).

The B_1^+ inhomogeneities caused by constructive and destructive interferences are even more severe at 9.4 T than at 7 T, which makes it difficult to achieve whole-brain coverage due to the field dropouts seen in the lower temporal lobes and cerebellum in the circularly polarized (CP) mode, even with relatively long coil elements (4). To improve longitudinal coverage and the RF shim capability in the z-direction, several research groups have already reported experimental (6–10) as well as numerical results (11,12) on the use of coil elements arranged in multiple rows. There is no significant difference in the transmit field pattern of a single-row array when compared with multiple-row transmit arrays if they are of similar length and driven in CP mode. However, multiple rows of transmit elements provide additional degrees of freedom to manipulate the transmit field using RF shimming methods for improved coverage of the lower brain (6–13). Special attention has to be paid to the power deposited in the tissue at 400 MHz, because this power loss can be highly localized and is not uniform over the entire volume (14). Therefore, realistic numerical simulations are essential to understand the RF field behavior in the MR environment in order to estimate the power deposited in the tissue and the local specific absorption rate (SAR).

The number of channels in most transceiver arrays presented up to now range from 8 to 16, depending on the available RF hardware in the scanner. Covering the same brain volume with a higher number of smaller receive elements on close-fitting, shaped helmets (15–18) results in significant signal-to-noise ratio (SNR) gain close to the array without losing sensitivity at larger distances (19) and improves parallel imaging performance due to the larger number of independent receive elements that are distributed in all spatial directions (20–22). The latter is an important factor in realizing the advantages of UHF MRI, as the reduced wavelength at high resonance frequency results in more distinct coil sensitivities and hence more effective sensitivity encoding (23).

In this work, we aim to evaluate the benefits offered by transmission and reception techniques using

individual arrays in MRI at 9.4 T. Thirty-one receive elements (to maintain symmetry, as described later) were arranged on a close-fitting helmet, and the receive array was combined with a 16-channel dual-row transmit array. The transmit performance and peak SAR averaged over 10 g of tissue (SAR_{10g}) were characterized in the CP mode. RF shimming was applied to improve transmit field homogeneity for high-quality, high-resolution whole-brain images in human subjects.

METHODS

The coil arrays were tested on a 9.4-T whole-body scanner (Siemens Healthcare, Erlangen, Germany), fitted with a head gradient insert (AC84; Siemens Healthcare) and equipped with 32 receive channels and a 7.5-kW RF amplifier (Advanced Energy Industries Inc., Fort Collins, CO, USA). To feed the 16 transmit elements, the RF signal was split into 16 components with equal amplitude and phase using a 1 × 16 power splitter (Werlatone, Brewster, NY, USA). RF shimming was restricted to static phase shimming, in which the transmit phase was adjusted by varying the length of the coaxial cable between the power splitter and the coil input. For CP mode excitation, the relative phase increment between neighboring elements was 22.5°.

Bench measurements were performed using a calibrated network analyzer (4396B; Agilent Technologies Inc., CA, USA) together with an 85046A *S*-parameter test set. The noise figure of the transmit/receive (TR) switch with preamplifier was measured using an Agilent N8973A noise figure meter and N4000A noise source. We imaged healthy volunteers who had signed a written consent form approved by the institutional review board of the University of Tübingen.

Transmit Array Construction

The transmit coil was constructed on a 2.5 mm thick fiber glass tube with an inner diameter of 28 cm. It consists of 16 identical rectangular loops (85 mm × 100 mm) arranged in two rows of eight elements each. A 12-mm gap was provided between the elements of the same row and between the rows. Lower row elements were rotated by 22.5° with respect to the upper row. All adjacent elements were inductively decoupled (24). Pads for soldering components were etched on a single-sided polyimide laminate (Novaclad® Laminate, Sheldahl, MN, USA) and attached to the fiber glass tube. A total of 13 fixed capacitors (5.6 pF, C-series; American Technical Ceramics, NY, USA, and Dalian Dalicap Co., Ltd., China) and one variable capacitor (5610; Johanson Manufacturing Corporation, NJ, USA) were distributed with equal spacing in each loop made of 2-mm-diameter silver wire. To actively detune the coil elements, a PIN diode (MA4PK2000, MA, USA) in series with an inductor was connected in parallel to one of the capacitors in each loop. This configuration requires sufficient reverse bias across the PIN diode to hold it in high-impedance state during spin excitation. The self-generated reverse bias direct current (DC) voltage that allowed the diode to operate in reverse-bias condition was measured as explained in Ref. 25. Furthermore, a measurement of flip

angle versus transmit voltage (26) showed linear behavior up to the maximum power that can be applied per transmit coil element.

Miniaturized versions (30 mm × 60 mm) of previously presented TR switches (4) with preamplifiers were included inside the coil housing. Even though this coil was not optimized for receive performance, adding receive capability provided two main benefits: first, it can be combined with non-proton coils where proton images are needed for localization, although additional cable traps might be required at the X-nuclei frequency; and second, the external TR switch modules that are used in most transceiver arrays (3,4) are removed, which simplifies the setup and reduces the loss in the receive path.

Cables with equal phase length were connected between the TR switch and each element input. The cables to the second-row elements were routed in such a way that there was minimal influence on the reflection and transmission parameters of the two adjacent elements in the first row. The DC signal to actively detune the second-row elements was inserted into the RF cable through a bias tee. DC wiring and RF cabling were limited by the lack of space around the coil inside the head gradient. Great care was taken to complete the wiring without affecting the characteristics of the individual coil elements. The transmit ports of the 16-TR switches were connected to two customized eight-channel non-magnetic high-power modular connectors (ODU Steckverbindungssysteme GmbH & Co. KG, Mühldorf, Germany). A picture of the completed coil assembly is shown in Figure 1a, with the element numbering presented in Figure 1b.

Receive Array Construction

A tight-fitting helmet (left/right: 185 mm; anterior/posterior (AP): 220 mm; head/foot: 200 mm) with 3 mm wall thickness was fabricated by a three-dimensional (3D) printer (Eden 250; Objet GmbH, Germany). A total of 31 receive elements were arranged in four rows covering a length of 180 mm along the *z*-direction (Fig. 2a). In each of the first two rows, 10 elements formed two complete rings around the helmet. The third and fourth rows consisted of symmetrically arranged partial rings with seven and four elements, respectively. The layout and dimensions of the receive array elements are shown in Figure 2a. A combination of inductive decoupling and geometric overlap (27) was adopted to cancel the inductive coupling between neighboring coil elements. A 10-mm gap (8 mm for row 1) was maintained between the adjacent elements in the same row, and the coupling between these elements was minimized by inductive decoupling, which leads to smaller element size and larger separation between the non-neighboring coil elements. Each lower row element geometrically overlaps with two from the upper row. The elements in the first row were tapered to cover the helmet's dome. As adding an additional element to the third or fourth row would spoil the left–right symmetry, the 32nd receive channel was not used (Fig. 2a).

To tune the coil elements to the Larmor frequency of 399.72 MHz, a total of six fixed capacitors (5.1 pF, B-series; American Technical Ceramics and Dalian Dalicap Co., Ltd.) and one variable capacitor (2320-2; Johanson
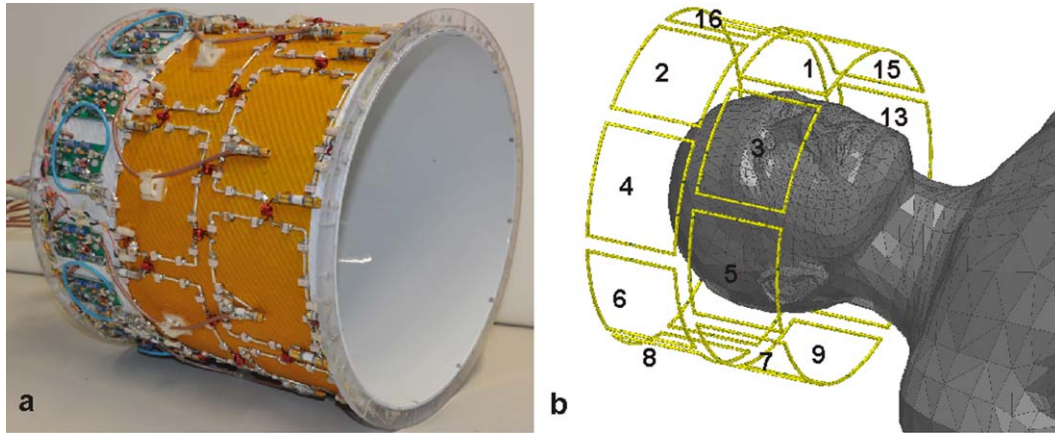
FIG. 1. **a:** Photograph of the transceiver array hardware with coil elements and the TR switches. **b:** Screenshot of the simulation model of the coil loaded with the phantom along with the assigned channel numbers. Only coil elements and human model are shown. [Color figure can be viewed in the online issue, which is available at wileyonlinelibrary.com.]

Manufacturing Corporation) were mounted in series. For the top-row elements, being smaller in size, five 6.2-pF fixed capacitors in combination with the variable capacitor were sufficient. Two capacitors in series were used at the input (Fig. 2b), one of which (matching capacitor [C_M]) was used for impedance matching whereas the other was part of the active detuning circuit, which also comprises a PIN diode (MA4P7470F-1072T; M/A-COM,

MA, USA) in series with a hand-wound inductor. The components of the input circuit consisting of matching, active detuning, and DC feed were assembled on a separate circuit board mounted on to the helmet. As secondary safety level, in case of malfunction of the detuning circuitry, a protection fuse (Siemens Healthcare) was incorporated on each channel. Solder pads made out of polyimide laminate were attached to the surface of the
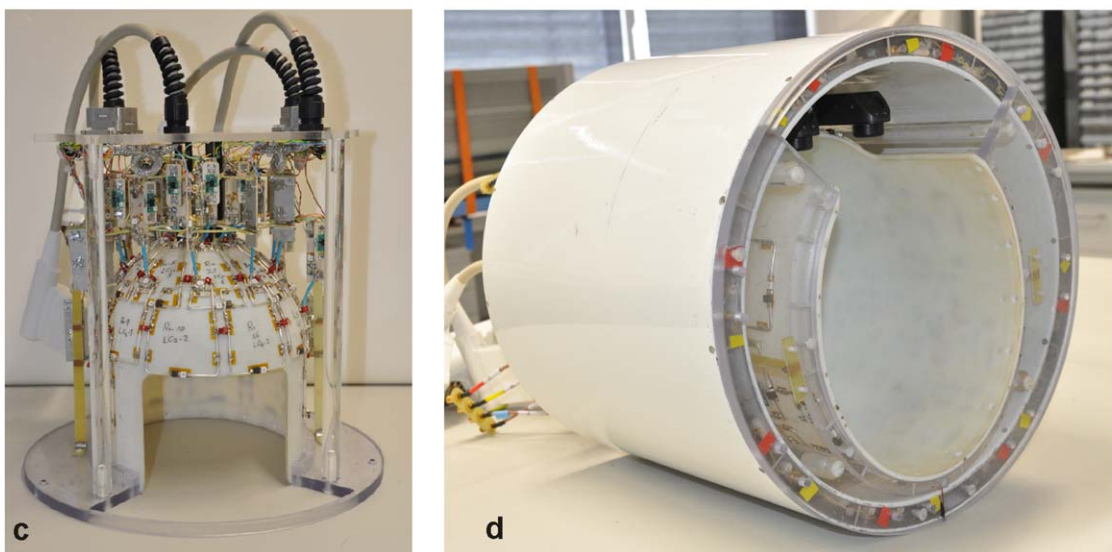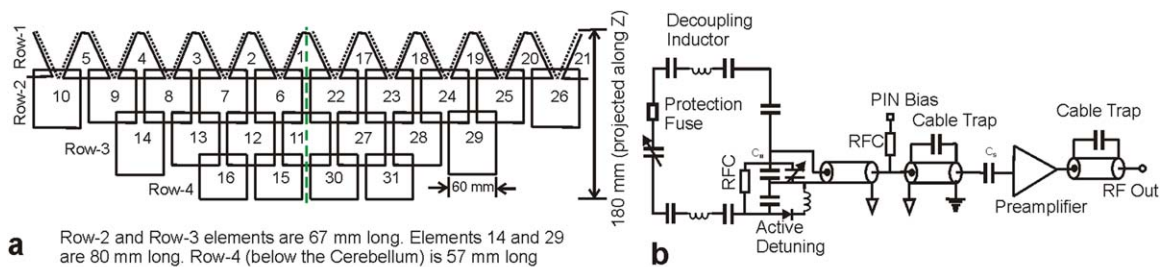

FIG. 2. Receive array. **a:** Two-dimensional view of the receive coil layout. Element dimensions are marked in the figure. **b:** Equivalent circuit schematic of a single element of the receive array. **c:** Photograph of the receive array. The socket on the top plate is used to plug-in the transmit array coil plugs. **d:** The final setup consists of the receive array and the periscopes assembled inside the transmit array. [Color figure can be viewed in the online issue, which is available at wileyonlinelibrary.com.]

helmet, and the components were soldered to these pads. Equal spacing between the capacitors was maintained. A 2-mm-diameter silver wire was used to connect these pads and to close the loop. A short coaxial cable connected the coil element with a circuit board, which consisted of two cable traps, one each at the input and output of the preamplifier, a series capacitor (C_S) to adjust the preamplifier decoupling (27), a bias tee and a low-noise preamplifier (WanTcom Inc., MN, USA). To protect the preamplifier from high voltage, a pair of PIN diodes (MPP4203; Microsemi, MN, USA) was added across the input of the high-electron mobility transistor (HEMT). The preamplifiers were assembled parallel to the B_0 field, and the circuit boards present inside the transmit field were oriented in such a way that its ground plane provides minimal shielding effect. The output cables are bunched together into four cable bundles, each with a cable trap across the outer sheath. Pictures of the receive array and the final setup are shown in Figures 2c and 2d, respectively. To allow for adding a fiber optics periscope for visual stimulation, the receive array was lowered in the AP direction (Fig. 2d).

Scanner Interface

The scanner has four coil sockets, each with eight bias lines that gives a total of 32 bias lines to control the two arrays. Eight bias lines were used to control 16 TR switches and another eight for active detuning of the 16 transmit elements. The remaining 16 bias lines were used to actively detune the receive array elements. To ensure equal splitting of the current to the shared elements, 43-Ω resistors were inserted in series with the bias lines in the input circuit board. The transmit array can be used in transceive mode (without the receive array) or in transmit-only receive-only (ToRo) mode. In transceive mode, the two coil plugs of the transmit array were connected directly to the scanner sockets. In ToRo mode, the four coil plugs of the receive array were plugged to the scanner sockets, and the DC signal to control the transmit array was routed from the receive array to two external sockets mounted on the top plate of the receive array (Fig. 2c), onto which the plugs of the transmit array were connected.

Coil Simulation

To accelerate the numerical analysis of the transmit array and to incorporate the effects of feeding/tuning/matching circuitry, a co-simulation approach consisting of an RF circuit simulator (ADS 2011.10; Agilent Technologies) and a 3D EM tool (HFSS 14; Ansys, PA, USA) was used for our investigation (28). The transmit array was tuned in the RF circuit domain, and then, the electric and magnetic field components were calculated together with SAR maps in the 3D EM domain. The realistic 3D EM model of the arrays included all coil construction details for the resonance elements, simulated with precise dimensions and electrical properties of the material. Series resistances (R_s) of 0.2 Ω for the PIN diodes and a Q of 200 at 400 MHz for the capacitors were assumed. Decoupling inductors and coil conductors were modeled with the same wire gauge as in the actual implementation. The head-gradient shield and the magnet bore were

included in the model. However, cable traps, RF cabling, and DC wiring were not included in the simulation. Only six components (feed-point, variable capacitor, and four decoupling ports) in each element were substituted by ports to reduce the time required for postprocessing and limit the amount of simulation data. Other distributed capacitors remained in the 3D EM domain. A multi-tissue human body model (29) extending up to the middle of the torso was scaled to mimic different head sizes (average head: $x = 0.9/y = 0.9/z = 0.9$; small head: 0.85/0.85/0.9; large head: 0.95/0.975/0.9). The position of the load was varied in the x–y plane to replicate the subject positions in the two different scanning modes: transceive mode, with the head position at the center, and the ToRo mode, in which the head was lowered to reproduce the head position inside the receive array. The locations and values of SAR_{10g} and the safe excitation efficiencies $\left(B_{1_{avg}}^+ / \sqrt{SAR_{10g}}\right)$ for the three body models were calculated for varying head positions along z-direction in 5-mm steps, where $B_{1_{avg}}^+$ is the value of B_1^+ averaged over the volume of interest. The investigation work flow in the numerical domain was as per the methods already presented (11,12). Because of the geometrical complexity of the receive array and some limitations in the 3D EM meshing, the receive array model was not incorporated in the numerical domain. Previous investigation of 7 T ToRo arrays (30) showed that a properly detuned receive array does not increase SAR_{10g}. Detuning of the receive array was validated by comparing field maps acquired with and without the actively detuned receive array in the transmit field. Uncertainty of SAR_{10g} due to the simplified numerical model was covered by an essential safety margin.

Transmit Field Characterization

The spatial distribution of the B_1^+ field generated by the transmit array was mapped in transceive mode and in ToRo mode. In transceive mode, the receive array was removed, and the receive signal was routed through the preamplifiers in the TR switches assembled in the transmit array. In the ToRo mode, the receive helmet was assembled inside the transmit array, and the signal was received using the 31 elements of the receive helmet. This comparison serves to establish the influence of the receive array hardware in the transmit field and to validate the performance of the active blocking networks in the receive array. An incremental transmit phase offset of $\sim 22.5°$ between adjacent transmit elements was used to generate the CP mode. A presaturated turbo FLASH sequence (26) and the 3D actual flip angle imaging (AFI) technique (31) (field of view: $230 \times 201 \times 154$ mm^3, matrix: $128 \times 56 \times 44$, TR_1/TR_2: 28/140 ms, echo time [TE]: 4.5 ms, bandwidth: 390 Hz/pixel, acquisition time: 10 min) were used for acquiring the field maps. The mean B_1^+ field produced by 1 V at the input of the matched coil was calculated for the measured transmit field and compared with the simulated field map.

Determination of the g-Factor

To determine the parallel imaging characteristics of the receive array, an average-sized head-and-shoulder phantom filled with tissue equivalent solution ($\varepsilon_r = 58.6$,

Table 1
S-parameters in dB showing the reflection and transmission parameters of the 16-channel transmit array when loaded with the head-and-shoulder phantom

Channel	1	2	3	4	5	6	7	8	9	10	11	12	13	14	15	16
1	−29	−14.8	−15.3	−23.3	−29.5	−28.3	−28.5	−28	−23.6	−32.6	−32.8	−23.4	−28	−34	−21.8	−18.5
2		−26	−14.5	−23	−21	−16	−19.2	−21.7	−44	−36.7	−31	−32	−26.5	−42	−17.9	−19.5
3			−21.5	−15.1	−16.3	−24	−25.8	−33.5	−33.5	−32.3	−25.8	−28.2	−48	−24	−34.5	−22.3
4				−24	−15.8	−18.8	−24.5	−18.8	−29.1	−27.8	−25.1	−32	−34.7	−32.5	−31.7	−30.3
5					−28	−15.9	−21.6	−25.9	−26.3	−30.7	−23.3	−29.7	−30.4	−25.2	−27.5	−19.5
6						−20	−13.7	−23.5	−30.3	−25.6	−32.7	−35	−30.4	−26.5	−26.5	−26
7							−27	−12.7	−18.8	−26	−28.3	−32.4	−39.2	−31.8	−27.7	−29.7
8								−25	−15.7	−14.4	−24.9	−27.8	−26.2	−29.5	−33.6	−39.3
9									−27	−13.7	−27	−24	−29.5	−35.5	−43	−25.1
10										−27	−14.1	−15.6	−27.9	−22.8	−21.2	−27.6
11											−26	−18.9	−18.8	−18.6	−18	−27.8
12												−35	−15.3	−14.1	−23.5	−24.6
13													−31	−15.5	−16.8	−16.6
14														−30	−12.8	−48
15															−36	−22
16																−28

$\sigma = 0.64$ S/m) (32) was scanned with a 3D gradient echo sequence (field of view: $256 \times 208 \times 160$ mm^3, voxel size: $1 \times 1 \times 1$ mm^3, TR $= 8$ ms, TE $= 2$ ms), using the GRAPPA parallel imaging technique with reduction factors (R) of 2, 3, and 4 in the AP direction. Each scan was repeated 15 times, and the mean values and standard deviations over these 15 scans were determined for every pixel. The *g*-factor for each pixel in the entire brain volume was determined by the following equation:

$$g = \frac{\text{SNR}_{R=1}}{\text{SNR}_R} \cdot \sqrt{\frac{T_R}{T_{R=1}}}, \qquad [1]$$

where SNR_R and $\text{SNR}_{R=1}$ are the SNRs in the accelerated and the nonaccelerated images, respectively, and T_R and $T_{R=1}$ are the corresponding scan durations.

SNR Comparison

To be able to assess the receive sensitivity of the presented array, a comparison to a previously published elliptical transceive array with 16 microstrip elements (4) was performed. For both coils, the head-and-shoulder phantom was used to obtain 3D gradient echo images with low flip angle and similar parameters as for the *g*-factor maps. In addition, the imaging experiment was repeated with a flip angle of zero to measure the noise distribution, and a flip angle map was generated using AFI (31). An SNR map over the entire volume was generated, and the flip angle map was used together with the known T_1 value of the phantom to calculate the SNR that would be reached with a flip angle of 90° and infinite repetition time (SNR$_{90}$) using the following equation:

$$\text{SNR}_{90} = \text{SNR} \cdot \frac{1 - \cos\alpha \cdot e^{-T_R/T_1}}{(1 - e^{-T_R/T_1}) \cdot \sin\alpha}, \qquad [2]$$

where α is the spatially varying flip angle as determined by the AFI measurement and T_R is the repetition time of the experiment.

RESULTS

Transmit Array

The head-and-shoulder phantom was used as the load for the bench measurements. Because of the lower loaded Q factor of the loop, the coil reflection and transmission parameters were less sensitive to load variations, and hence, the coil was not retuned to individual subjects. As the transmit array was shielded by the head gradient insert, the bench measurements were done by positioning the coil inside a bore simulator that mimics the influence of the head gradient. A self-built test-jig was used to provide the control signals to the coil as in the scanner. The coil reflection and transmission coefficients were measured through the TR switch, which was switched to transmit mode using the test-jig. The return loss on each transmit channel was adjusted to at least −20 dB in the loaded condition. To show the decoupling between all coil elements in transmit condition, the complete *S*-parameter matrix is tabulated in Table 1 with the element numbering from Figure 1b. All neighboring elements, both within the row and between the rows, and the non-neighboring elements were well decoupled. The quality of active detuning was measured using a pair of decoupled flux probes. The active detuning PIN diodes provided −30 dB of isolation when 50 mA current was supplied to each coil element. The TR switches with built-in preamplifiers provided a gain of 27 dB, a noise figure of 0.8 dB and 41 dB of protection from transmit RF. The noise correlation matrix that shows the coupling in the receive condition is shown in Figure 3a. In this plot, the average decoupling between all neighboring elements is −18 dB.

Receive Array

The unloaded Q (Q_{UL}) of a single receive element, measured in an unshielded environment and which also contained the decoupling inductor, was 190. Q_{UL} dropped to 160 when the protection fuse and active detuning circuit were added. The unloaded to loaded
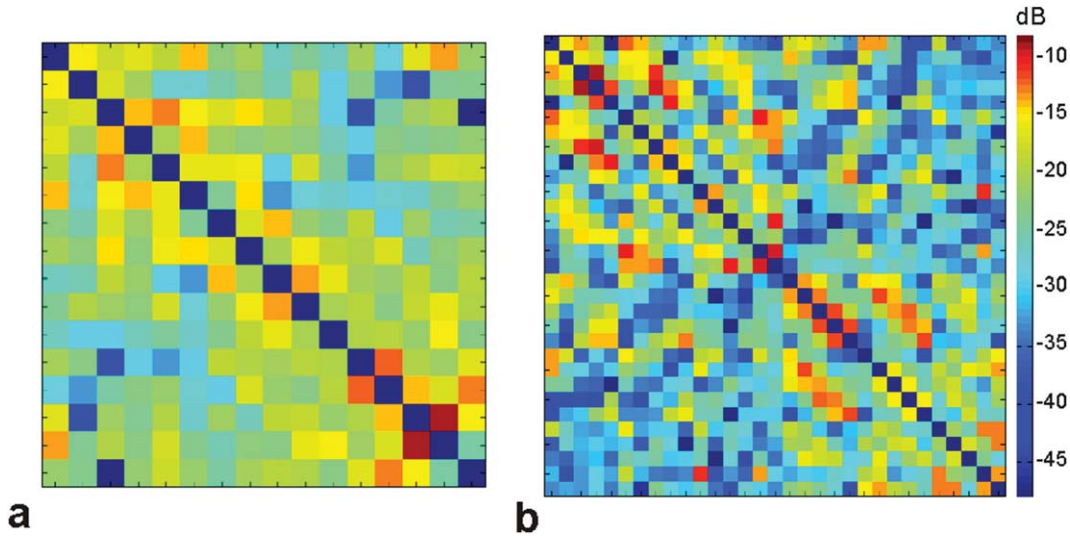
FIG. 3. Noise correlation plots in decibels. **a:** Transmit array: The average coupling between adjacent elements in the transceive mode is −18 dB. **b:** Receive array: Average value of the adjacent element decoupling is −15.6 dB, and the average of all off-diagonal values is −25.9 dB.

Q ratio (Q_{UL}/Q_L), depending on the proximity of the receive element to the load, varied between 8 and 12, indicating sample noise dominance. The average PIN diode detuning measured with a pair of decoupled flux probes was −36 dB with 50 mA of DC. The coil was loaded with the head-and-shoulder phantom, and the impedance matching and adjacent element decoupling were determined with all coil elements in tuned condition. The capacitors C_M and C_S influence both impedance match and preamplifier decoupling and hence were both adjusted iteratively. A target impedance match of −15 dB

was achieved on all the channels. Preamplifier decoupling was measured in an unloaded coil with two elements in tuned state (each PIN bias line controls two channels), whereas all other elements were actively detuned. The difference between the S_{21} values measured with a pair of decoupled flux probes, when the coil was terminated to 50 Ω and then to the low input impedance preamplifier, was −23 dB.

Figure 3b shows the noise correlation matrix of the receive array when loaded with the head-and-shoulder phantom. The plot shows that the coil element layout
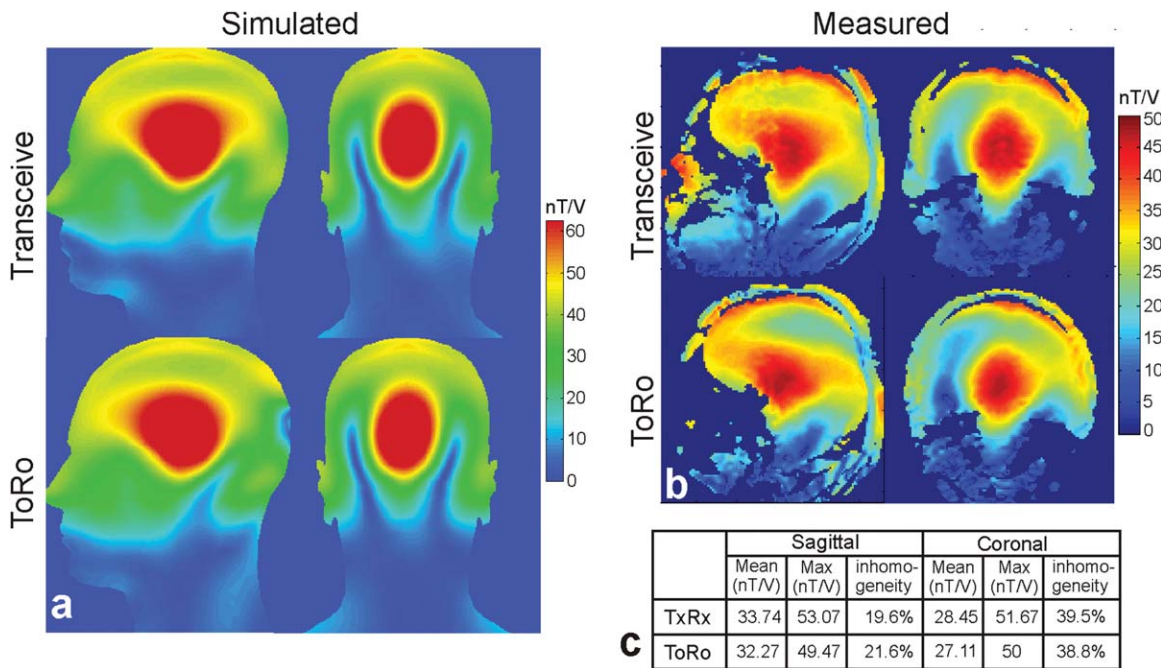

		Sagittal			Coronal		
		Mean (nT/V)	Max (nT/V)	inhomo-geneity	Mean (nT/V)	Max (nT/V)	inhomo-geneity
TxRx		33.74	53.07	19.6%	28.45	51.67	39.5%
ToRo		32.27	49.47	21.6%	27.11	50	38.8%

FIG. 4. Transmit field (B_1^+) maps in the two scan modes. The head is centered in the transmit array in transceive mode and offset in the AP direction in ToRo mode. **a:** Central sagittal and coronal slices of the simulated field maps. **b:** Measured field maps. **c:** A comparison of the measured field maps (in nT/V) in the two scan modes to estimate the influence of the receive array on the transmit performance.

used for constructing the receive array provides very good decoupling. The maximum value in this plot was −8.95 dB, and the average isolation achieved between all the adjacent element pairs was −15.6 dB. The average of all the off-diagonal values in the matrix was −25.9 dB.

Transmit Field Characterization and SAR

The first row in Figure 4a shows sagittal and coronal views of the simulated field maps in transceive mode, whereas the second row shows the corresponding field maps in ToRo mode. The variation in the transmit field distribution as seen in the central sagittal slice, particularly in the back of the head where the subject is closest to the transmit elements, is due to the lowered position of the load in the ToRo mode. For brain volume superior to the cerebellum, the CP mode provides a relatively efficient excitation. However, a characteristic arc due to field cancellation can be seen across the cerebellum, which is typical of CP mode excitation at 9.4 T. Hence, the uniformity and excitation efficiency were calculated for the brain volume superior to the cerebellum. To extend the excitation to the temporal lobe and to the cerebellum, RF shimming methods (33) are essential.

The measured field maps using the two scan modes are shown in Figure 4b. The transmit efficiency, measured on a $2 \times 2 \times 2$ cm^3 volume in the center of the brain, was 47.33 nT/V. In ToRo mode, the measured transmit field was altered in the back of the head. This is not due to the presence of the receive array but to the lowered head position as predicted in the simulated sagittal field map. Furthermore, field maps were acquired in the two scan modes with the same subject, maintaining the same position inside the transmit array, to determine the influence of the receive array on the transmit performance. Figure 4c shows statistics of the comparison from a region of interest drawn on the central sagittal and coronal slices covering the brain superior to the cerebellum. The drop in the mean transmit field in the presence of the receive array was less than 5%, indicating sufficient decoupling between transmit and receive arrays.

The mean transmit efficiency in CP mode, calculated from the measured field maps in the whole brain volume superior to the cerebellum, was 28.67 nT/V with an inhomogeneity of 24.9%. This means that a pulse length of 916 µs would be required to achieve a mean flip angle of 90° over the brain volume using a 1-kW hard pulse. The transmit efficiency of this array is lower than that reported earlier at 7 T (6,8) because of the much larger coil size, increase in coil and tissue losses at 9.4 T, and a different RF shim setting. The mean transmit efficiency from the simulated dataset was 40.8 nT/V for the corresponding volume. The additional losses in the measured transmit field are due to a number of factors such as differences in the load, solder joints, the complex cabling involved in the transmit array design, which were not included in the simulation and possible mismatches in the excitation phase.

An estimate of the power budget obtained from the numerical model is shown in Figure 5a. About 43% of the transmit power was delivered to the tissue. The most
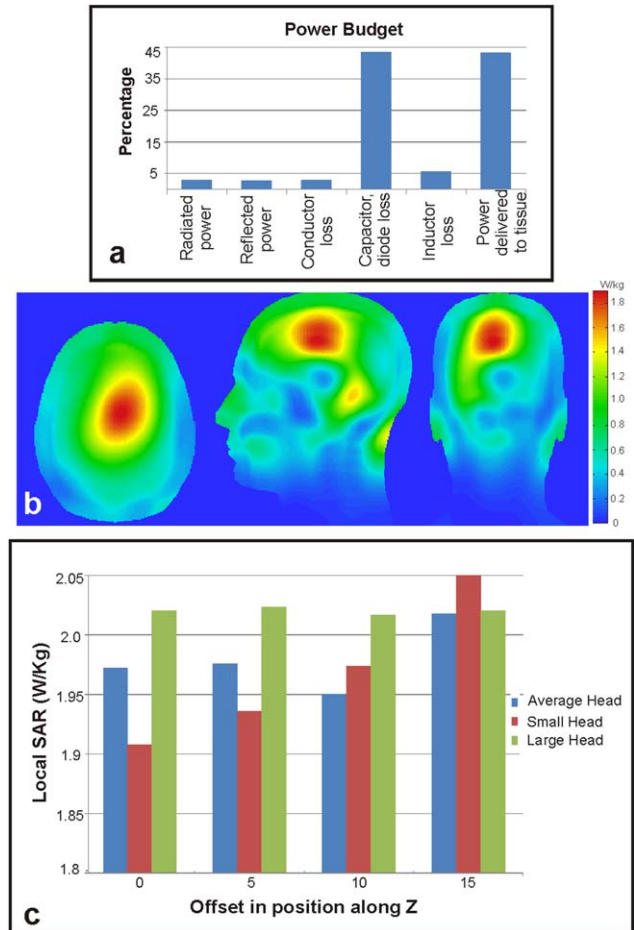

FIG. 5. **a:** Power budget analysis showing the distribution of the total input power. **b:** SAR$_{10g}$ for the 2×8 transmit array in CP mode excitation. **c:** Dependence of local SAR$_{10g}$ to different head size and position. A transmit power of 8 W was used in b and c. [Color figure can be viewed in the online issue, which is available at wileyonlinelibrary.com.]

significant loss factor is the capacitor loss that accounts for 44%. Losses to the coil components increase largely because of the increase in dielectric loss due to the lower Q of the capacitors. To measure the temperature rise on coil components, an RF source was connected to a single transmit element (all other elements terminated to 50 Ω) for 30 min and set to the maximum power as limited by the SAR settings. The maximum temperature rise, measured using a fiber optic probe, was 5.2°C on the diode and 3.6°C on the capacitors and well within the component specifications. Furthermore, no variation in S-parameter was observed before and after the heat test.

The calculated SAR$_{10g}$ profiles are shown in Figure 5b. The peak SAR$_{10g}$ was 1.8975 W/kg in the CP mode. To understand the robustness of the transmit array configuration, the dependence of peak SAR$_{10g}$ on different head sizes and its positional variation is plotted in Figure 5c. To ensure safety in subject measurements, the transmit power was limited based on the maximum of the estimated local SAR$_{10g}$, adding a safety margin of 100%. This is in addition to the overestimation of SAR$_{10g}$ due to the stronger B_1^+ in the numerical domain.
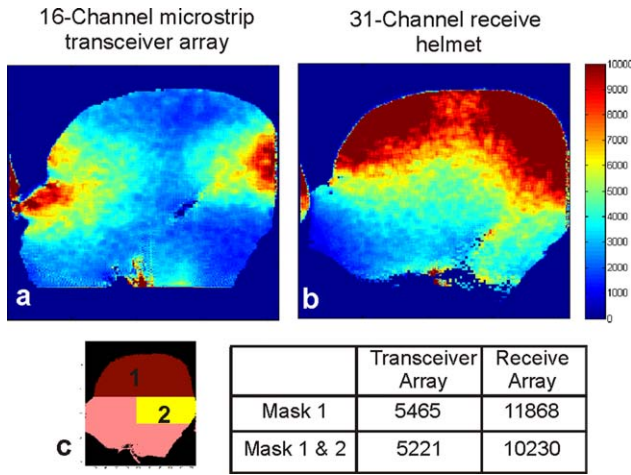
FIG. 6. SNR comparison. **a:** SNR map of the 16-channel microstrip transceive array on the head-and-shoulder phantom. **b:** SNR map of the 31-channel receive array. Same color scale is used for both maps. **c:** Representation of the mask used for the SNR calculation and the SNR from the respective volumes. [Color figure can be viewed in the online issue, which is available at wileyonlinelibrary.com.]

Receive Array Performance

Figure 6 shows receive SNR maps of the head-and-shoulder phantom, extrapolated to a flip angle of 90° and long TR, for the presented coil in comparison with a 16-channel microstrip array (4). Two masks, one covering the brain volume superior to the cerebellum and the second mask covering the brain volume with the cerebellum, were created. The SNR gain in the first volume was a factor of 2.17, and in the entire volume represented by masks 1 and 2 was 1.96. This gain is due to the smaller size of the receive elements and their proximity to the head in the close-fitting helmet.

Figure 7 shows *g*-factor maps, acquired with the receive array loaded with the head-and-shoulder phantom, for acceleration up to a factor of 4 in the AP direction. The average *g*-factors (G_{avg1} and G_{avg12}) were calculated for the whole volume represented by the masks shown in Figure 6. The noise amplification remained sufficiently low, demonstrating good parallel imaging behavior. The *g*-factor values of less than 1 are

due to noise cancellation in the reconstruction process and are a well-known feature of GRAPPA (34,35). Figure 8 demonstrates the parallel imaging capability of the receive array with GRAPPA acceleration in two directions with no visible artifacts even up to an acceleration factor of 8.

Figure 9 shows high-resolution in vivo FLASH images without intensity correction acquired with the receive array. For these images, a slice-selective B_1 phase shimming approach (33) was used to optimize the transmit phase required for improved B_1^+ homogeneity. The calculated phase offsets for the individual channels were realized by inserting coaxial cables as phase shifters in the transmit path. The estimated phase depends on the cost function used in the shim algorithm (homogeneity/efficiency; Ref. 13), slice position and orientation, reflection and coupling characteristics of the coil, and size and shape of the head and its position inside the coil. These images demonstrate the ability to influence the B_1^+ field in all three spatial directions and to mitigate the severe B_1^+ artifacts typically present in the lower brain at 9.4 T.

DISCUSSION AND CONCLUSION

Currently, transceiver array coils are used in most applications that require multichannel transmit at UHF. In contrast, receive arrays are being used in almost every MRI examination at clinical field strengths because of their superior receive sensitivity. The close-fitting transceiver arrays reach high transmit efficiency; however, these arrays require time-consuming, subject-specific adjustments before each scan session. In this work, at 9.4 T, a receive array was successfully combined with a transmit array, which provides the capability to modulate the transmit field in all three directions. Time-consuming tune and match adjustments are not necessary, thus providing a simple and fast setup, comparable with clinical routine examination. The coil combination provides high receive sensitivity when compared with a transceiver approach, although at the cost of reduced
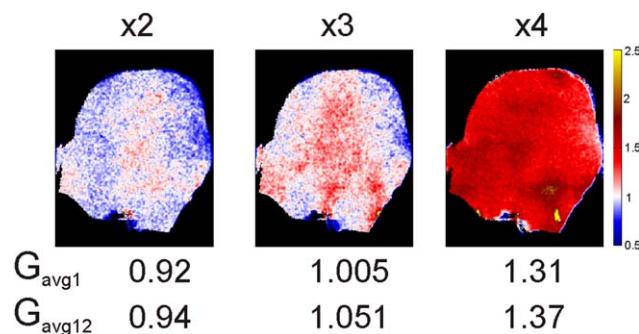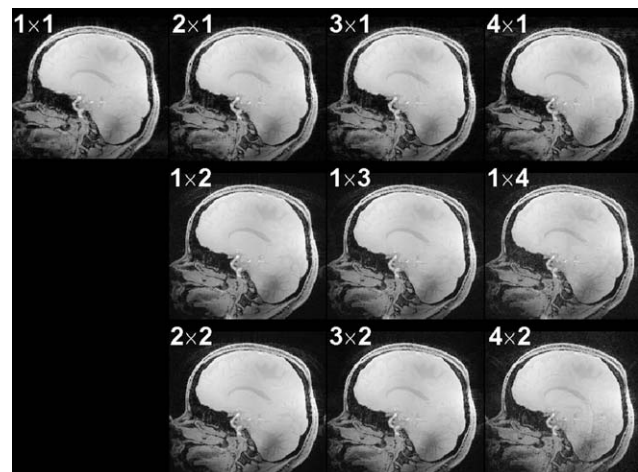

FIG. 7. The *g*-factor maps for the receive array with acceleration factor up to 4 in the AP direction. The mean *g*-factors for the volumes represented in Figure 6 are shown for each acceleration factor. [Color figure can be viewed in the online issue, which is available at wileyonlinelibrary.com.]

FIG. 8. Gradient echo images with GRAPPA acceleration in two directions: In the image, $i \times j$ corresponds to anterior–posterior × right–left (in-plane × through-plane).

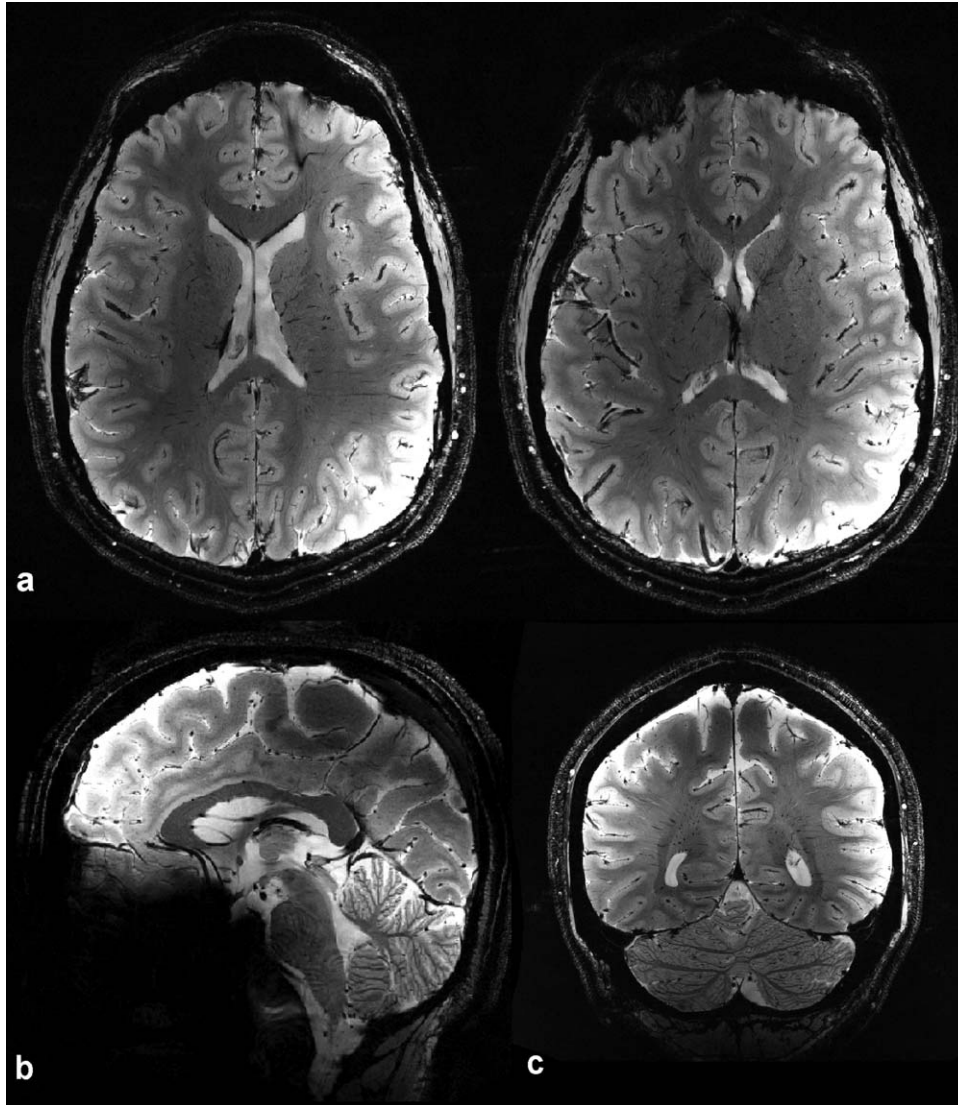FIG. 9. RF-shimmed in vivo images: (**a**) axial view: TE = 14 ms, TR = 400 ms, 260 μm in-plane resolution (702 × 832 matrix), slice thickness (ST) = 1 mm, nominal flip angle (FA) = 35°, acquisition time (TA) = 4 min, 41 s; (**b**) sagittal view: TE = 14 ms, TR = 500 ms, 330 μm in-plane resolution (522 × 576 matrix), ST = 1 mm, FA = 25°, TA = 3 min, 48 s; (**c**) coronal view: TE = 14 ms, TR = 400 ms, 250 μm in-plane resolution (768 × 820 matrix), ST = 1 mm, FA = 25°, TA = 5 min, 12 s.

transmit efficiency due to the large size of the transmit array. Using an elliptic cross section that conforms more closely to the head than the currently used circular shape could help to further improve the transmit efficiency. In addition, the issue of increased coil component loss at 400 MHz should be addressed, which is currently a dominant loss factor.

At frequencies as high as 400 MHz, the capacitance across overlapped loop strips of the receive element is a significant factor and this increases capacitive coupling. Wiggins et al. (16) demonstrated the benefits of using wires for coil loop conductors at 3 T. By adopting this approach for the receive array design, the decoupling between overlapped coil elements could be improved to −15 dB from −11 dB due to reduced capacitive coupling. The SNR map in Figure 6 shows that SNR gain was achieved over the entire brain volume. However, the SNR in the region of the cerebellum is not as high as in the cortex, demonstrating the need for coil elements closely following the contours of the anatomy. Further adaptation of the coil shape to the head will complicate the electromechanical design of our setup. It would

require a split-top housing design for the receive array and either a sliding or a split-top design for the transmit array to allow subject positioning in the coil.

As the RF power from a single amplifier was split up to excite each coil element, our experimental results were restricted to CP mode and static phase shimming (33). An even simpler static shim approach, applying global phase offset between the two rows, provided improved homogeneity in the upper brain at the cost of slightly reduced transmit efficiency (9,11,12) when compared with the CP mode. The availability of parallel transmit systems with independent amplitude and phase control adds another degree of freedom to improve spin excitation in terms of homogeneity, power efficiency, or SAR reduction. The transmit and receive array combination presented here is an enabling hardware for all these approaches.

REFERENCES

1. Van de Moortele PF, Akgun C, Adriany G, Moeller S, Ritter J, Collins CM, Smith MB, Vaughan JT, Ugurbil K. B1 destructive interferences

and spatial phase patterns at 7T with a head transceiver array coil. Magn Reson Med 2005;54:1503–1518.

2. Vaughan JT, Delabarre L, Snyder C, et al. 9.4T human MRI: preliminary results. Magn Reson Med 2006;56:1274–1282.

3. Adriany G, Van de Moortele PF, Wiesinger F, et al. Transmit and receive transmission line arrays for 7T parallel imaging. Magn Reson Med 2005;53:434–445.

4. Shajan G, Hoffmann J, Budde J, Adriany G, Ugurbil K, Pohmann R. Design and evaluation of an RF front-end for 9.4T human MRI. Magn Reson Med 2011;66:596–604.

5. Avdievich NI, Pan JW, Kuznetsov AM, Hetherington HP. Variable geometry elliptical transceiver phased array for imaging of the human brain at 7T. In Proceedings of the 17th Annual Meeting of ISMRM, Honolulu, Hawaii, USA, 2009. p 3002.

6. Avdievich NI, Pan JW, Hetherington HP. Improved longitudinal coverage for human brain at 7T: A 16 element transceiver array. In Proceedings of the 19th Annual Meeting of ISMRM, Montreal, Canada, 2011. p 328.

7. Gilbert KM, Curtis AT, Gati JS, Klassen LM, Menon RS. A radiofrequency coil to facilitate B1+ shimming and parallel imaging acceleration in three dimensions at 7T. NMR Biomed 2011;24:815–823.

8. Gilbert KM, Belliveau JG, Curtis AT, Gati JS, Klassen LM, Menon RS. A conformal transceive array for 7T neuroimaging. Magn Reson Med 2012;67:1487–1496.

9. Adriany G, Gözübüyük A, Auerbach EJ, Van de Moortele PF, Anderson P, Vaughan JT, Ugurbil K. A 32 channel transmit/receive transmission line head array for 3D RF shimming. In Proceedings of the 15th Annual Meeting of ISMRM, Berlin, Germany, 2007. p 166.

10. Adriany G, Ritter J, Vaughan JT, Ugurbil K, Van de Moortele PF. Experimental verification of enhanced B1 shim performance with a Z-encoding RF coil array at 7 tesla. In Proceedings of the 18th Annual Meeting of ISMRM, Stockholm, Sweden, 2010. p 3831.

11. Kozlov M, Turner R. Analysis of RF transmit performance for a 7T dual row multichannel MRI loop array. In Proceedings of the 33rd Annual International Conference of the IEEE EMBS, Boston, MA, USA, 2011. pp 547–553.

12. Kozlov M, Turner R. Analysis of RF transmit performance for a multi-row multi-channel MRI loop array at 300 and 400 MHz. In Proceedings of the Asia-Pacific Microwave Conference, Melbourne, Australia, 2011. pp 1190–1193.

13. Shajan G, Hoffmann J, Scheffler K, Pohmann R. A 16-element dual-row transmit coil array for 3D RF shimming at 9.4T. In Proceedings of the 20th Annual Meeting of ISMRM, Melbourne, Australia, 2012. p 308.

14. Robitaille PM, Berliner LJ. Ultra high field magnetic resonance imaging (biological magnetic resonance), Vol. 26. Berlin: Springer. 131 pp.

15. Wiggins GC, Triantafyllou C, Potthast A, Reykowski A, Nittka M, Wald LL. 32-Channel 3 tesla receive-only phased array head coil with soccer-ball element geometry. Magn Reson Med 2006;56:216–223.

16. Wiggins GC, Polimeni JR, Potthast A, Schmitt M, Alagappan V, Wald LL. 96-Channel receive-only head coil for 3 tesla: design optimization and evaluation. Magn Reson Med 2009;62:754–762.

17. Wiggins GC, Wiggins CJ, Potthast A, Alagappan V, Kraff O, Reykowski A, Wald LL. A 32 channel receive-only head coil and detunable

18. Ledden PJ, Mareyam A, Wang S, Van Gelderen P, Duyn J. 32 Channel receive-only SENSE array for brain imaging at 7T. In Proceedings of the 15th Annual Meeting of ISMRM, Berlin, Germany, 2007. p 242.

19. Wright SM, Wald LL. Theory and application of array coils in MR spectroscopy. NMR Biomed 1997;10:394–410.

20. Pruessmann KP, Weiger M, Scheidegger MB, Boesiger P. SENSE: sensitivity encoding for fast MRI. Magn Reson Med 1999;42:952–962.

21. Sodickson DK, Manning WJ. Simultaneous acquisition of spatial harmonics (SMASH): fast imaging with radio frequency coil arrays. Magn Reson Med 1997;38:591–603.

22. Griswold MA, Jakob PM, Heidemann RM, Nittka M, Jellus V, Wang J, Kiefer B, Hasse A. Generalized autocalibrating partially parallel acquisitions (GRAPPA). Magn Reson Med 2002;47:1202–1210.

23. Wiesinger F, Van de Moortele PF, Adriany G, Zanche ND, Ugurbil K, Pruessmann KP. Potential and feasibility of parallel MRI at high field. NMR Biomed 2006;19:368–378.

24. Kokubunji TN, Soka TT, Kashiwa YM, Akishima EY, Katakura K. RF probe for MRI. US Patent 5,489,847, 1994.

25. Caverly RH, Hiuller G. Establishing the minimum reverse bias for a p-i-n diode in a high-power switch. IEEE Trans Microwave Theory Tech 1990;38:1938–1943.

26. Chung S, Kim D, Breton E, Axel L. Rapid B1+ mapping using a preconditioning RF pulse with TurboFLASH readout. Magn Reson Med 2010;64:439–446.

27. Roemer PB, Edelstein WA, Hayes CE, Souza SP, Mueller OM. The NMR phased array. Magn Reson Med 1990;16:192–225.

28. Kozlov M, Turner R. Fast MRI coil analysis based on 3-D electromagnetic and RF circuit co-simulation. J Magn Reson 2009;200:147–152.

29. Vogel M, Kleihorst R. Large-scale simulations including a human body model for MRI. In Proceedings of the IEEE Microwave Conference, Honolulu, Hawaii, USA, 2007. pp 1345–1348.

30. Kozlov M, Turner R. Comprehensive numerical study of 7T transmit-only, receive-only array coils. In Proceedings of the 18th Annual Meeting of ISMRM, Stockholm, 2010. p 1447.

31. Yarnykh VL. Actual flip-angle imaging in the pulsed steady state: a method for rapid three-dimensional mapping of the transmitted radiofrequency field. Magn Reson Med 2007;57:192–200.

32. Beck BL, Jenkins KA, Rocca JR, Fitzsimmons JR. Tissue-equivalent phantoms for high frequencies. Concepts Magn Reson B 2004;20:30–33.

33. Hoffmann J, Budde J, Shajan G, Pohmann R. Slice-selective B1 phase shimming at 9.4 tesla. In Proceedings of the 18th Annual Meeting of ISMRM, Stockholm, Sweden, 2010. p 1470.

34. Robson PM, Grant AK, Madhuranthakam AJ, Lattanzi R, Sodickson DK, McKenzies CA. Comprehensive quantification of signal-to-noise ratio and g-factor for image-based and k-space-based parallel imaging reconstructions. Magn Reson Med 2008;60:895–907.

35. Polimeni JR, Wiggins GC, Wald LL. Characterization of artifacts and noise enhancement introduced by GRAPPA reconstructions. In Proceedings of the 16th Annual Meeting of ISMRM, Toronto, Canada, 2008. p 1286.

2.3 Publication No. 3

A Three-layered RF Coil Arrangement for Sodium MRI of the Human Brain at 9.4 Tesla

G. Shajan, Christian Mirkes, Kai Buckenmaier, Jens Hoffmann, Rolf Pohmann and Klaus Scheffler, Magn Reson Med DOI: 10.1002/mrm.25666

Three-layered Radio Frequency Coil Arrangement for Sodium MRI of the Human Brain at 9.4 Tesla

G. Shajan,[1]* Christian Mirkes,[1,2] Kai Buckenmaier,[1] Jens Hoffmann,[1] Rolf Pohmann,[1] and Klaus Scheffler[1,2]

Purpose: A multinuclei imaging setup with the capability to acquire both sodium (^{23}Na) and proton (^{1}H) signals at 9.4 Tesla is presented. The main objective was to optimize coil performance at the ^{23}Na frequency while still having the ability to acquire satisfactory ^{1}H images.

Methods: The setup consisted of a combination of three radio frequency (RF) coils arranged in three layers: the innermost layer was a 27-channel ^{23}Na receive helmet which was surrounded by a four-channel ^{23}Na transceiver array. The outer layer consisted of a four-channel ^{1}H dipole array for B_0 shimming and anatomical localization. Transmit and receive performance of the ^{23}Na arrays was compared to a single-tuned ^{23}Na birdcage resonator.

Results: While the transmit efficiency of the ^{23}Na transceiver array was comparable to the birdcage, the ^{23}Na receive array provided substantial signal-to-noise ratio (SNR) gain near the surface and comparable SNR in the center. The utility of this customized setup was demonstrated by ^{23}Na images of excellent quality.

Conclusion: High SNR, efficient transmit excitation and B_0 shimming capability can be achieved for ^{23}Na MRI at 9.4T using novel coil combination. This RF configuration is easily adaptable to other multinuclei applications at ultra high field ($\geq$ 7T). **Magn Reson Med 000:000–000, 2015. © 2015 Wiley Periodicals, Inc.**

Key words: receive array; 9.4T; dual tuned coils; ^{23}Na MRI

INTRODUCTION

Sodium (^{23}Na) MRI can be used to gain complementary information about cellular viability and metabolism to proton (^{1}H) imaging (1–4). However, the low in vivo concentration and the small gyromagnetic ratio of the ^{23}Na nucleus lead to an inherently low signal-to-noise ratio (SNR). ^{23}Na MRI at ultra high field (UHF, $\geq$ 7 Tesla (T)) is highly beneficial because of the more than linear increase in SNR with respect to the strength of the static magnetic field (B_0) (5–8). This article focuses on the

[1]High Field MR Center, Max Planck Institute for Biological Cybernetics, Tübingen, Germany.

[2]Department for Biomedical Magnetic Resonance, University of Tübingen, Tübingen, Germany.

*Correspondence to: G. Shajan, M.E., High Field MR Center, Max Planck Institute for Biological Cybernetics, Spemannstr. 41, 72076 Tübingen, Germany.
E-mail: shajan.gunamony@tuebingen.mpg.de

design of a radio frequency (RF) coil setup custom-built for ^{23}Na MRI at 9.4T.

B_0 shimming capability, efficient transmit sensitivity and high SNR are some of the desirable aspects of an RF coil meant for ^{23}Na imaging. Shimming to maximize B_0 homogeneity is an essential requirement at UHF because the inhomogeneity increases with field strength. Enabling ^{1}H and ^{23}Na imaging in an integrated dual-frequency RF coil configuration avoids the need to switch between ^{1}H and ^{23}Na coils to determine the values of adequate shim currents (9,10). Furthermore, shimming at ^{1}H frequency is accomplished in a considerably shorter time compared to shimming at the ^{23}Na frequency (11,12).

B_0 shimming and anatomical localization in dual-frequency applications at clinical field strengths (1.5T and 3T) were accomplished in the past using dual-tuned RF coils which produced identical current distributions at two different frequencies (13,14). However, these dual-tuned coils suffer from a loss in transmit efficiency introduced by the high impedance trap circuits that are part of the design. Moreover, due to the shorter ^{1}H RF wavelength, this type of coil is not well suited to provide whole brain excitation for the ^{1}H frequency at 9.4T. Instead, transmit arrays must be used to provide sufficient spatial coverage for ^{1}H imaging and B_0 mapping (15). Combining a ^{1}H array with a head sized ^{23}Na resonator is difficult because the birdcage rungs can significantly shield the local ^{1}H array surrounding the birdcage.

Another important design consideration is maximizing the SNR at the ^{23}Na frequency. As has been shown previously, phased array coils can be used to accomplish this task (16,17). Experimental SNR comparisons for proton imaging at 3T, which is close to the ^{23}Na frequency (105.7 MHz) at 9.4T, presented by Keil et al (18) demonstrated that increasing the number of coil elements, even up to 64 channels, allows retaining the central SNR while increasing the SNR in the periphery. Only a marginal drop in central SNR was reported (using optimum SNR combination) for a 96-channel head array, while achieving a higher SNR close to the coil elements (19).

It is a challenging task to incorporate all the desired features discussed above into one coil setup. Nevertheless, the principal design criterion remains the optimization of the coil performance at the ^{23}Na frequency while maintaining adequate spatial coverage and sensitivity at the ^{1}H frequency. Nested (20,21) and composite (22) ^{23}Na/^{1}H arrays are some of the coil configurations that have already been used successfully at 3T and 7T. We aimed to meet the various needs of ^{23}Na imaging at 9.4T

by integrating three different RF coil arrays onto a single structure. The outermost layer consisted of a four-element transceiver ^{1}H dipole array providing large longitudinal coverage for anatomical localization and B_0 shimming. In the middle layer, a four-element [23]Na loop array that could be operated in transmit-only or transceive mode was inserted. The received signal from the four [23]Na loops was combined and routed to a single receiver. The innermost layer consisted of a 27-channel receive array constructed on a tight fitting helmet and making use of the remaining available receive channels of the MR system.

The performance of the three layered coil setup was evaluated by comparing the transmit efficiency and SNR to a single tuned [23]Na quadrature birdcage coil. Moreover, the ability to acquire whole brain ^{1}H images at 399.7 MHz in the presence of the [23]Na transmit and receive arrays is demonstrated.

METHODS

All measurements were performed on a 9.4T whole-body human MR scanner (Siemens Healthcare, Erlangen, Germany), equipped with a SC72 gradient system having a maximal amplitude of 40 mT/m and a maximum slew rate of 200 T/m/s. A narrowband amplifier with a maximum output of 7.5 kW was used for ^{1}H excitation while a broadband amplifier capable of delivering 4 kW covered the frequency range needed for [23]Na MRI (105.7 MHz). Signal reception was enabled by 32 independent broadband receive channels. Bench measurements were performed using a calibrated network analyzer (4396B, Agilent Technologies Inc., CA) together with an 85046A S-parameter test set. The electrical properties of phantom solutions were measured at room temperature using a dielectric probe kit (DAK-12, SPEAG, Zurich, Switzerland).

[1]H Transceiver Array

The objective of the ^{1}H coil was to provide whole brain excitation in the presence of the [23]Na transceiver and receive arrays without having a negative influence on the performance of the [23]Na coils. We have shown previously that a combination of a ^{1}H patch antenna and a single tuned [23]Na high pass birdcage coil provides whole brain excitation at the ^{1}H frequency without influencing the [23]Na coil performance (23). However, the performance of such a patch antenna would be compromised when combined with a multichannel [23]Na receive array due to the numerous cables and receive electronics that have to be placed between the antenna and the subject's head.

In this work, dipole elements, which have been proposed as a promising alternative for UHF applications, were used because they are much simpler to construct than phased arrays and offer extended longitudinal coverage (24). A dipole for the ^{1}H frequency at 9.4T is 37.5 cm long in free space. To accommodate the dipole in the head sized coil, the dipoles were shortened to 22 cm by adding tuning inductors (24). Four dipole elements were assembled on 25 mm spacers fixed on to a fiber glass tube (inner diameter: 26 cm, wall thickness:

3 mm, length: 30 cm). The dipole elements were equally spaced around the cylinder with an angular separation of 90°. A shielded cable trap was formed in the coaxial cable that fed the dipoles. For transceive mode operation, the dipole elements were interfaced to the scanner through a separate TR switch on each channel. The TR switches were miniaturized version of the TR switch design presented by Shajan et al (25).

The dipoles were tuned and matched inside the magnet bore to a head and shoulder phantom filled with tissue-equivalent solution ($\varepsilon_r = 58.6$ and $\sigma = 0.64$ S/m) (26). The four-element ^{1}H dipole array formed the outermost layer of the RF coil setup. To compensate for the frequency shift introduced by the [23]Na coils in the inner layers and the coil cover that surrounds the dipole array, tuning adjustments on the dipoles were carried out in the magnet bore on the fully assembled coil setup. This tuning step was performed once and was not repeated for individual subjects.

[23]Na Transceiver Array

One of the main considerations for a [23]Na transceiver coil design, in addition to transmit efficiency and uniformity of the RF field, was to adopt a design that has minimal influence on the ^{1}H array. Birdcage coils are the most commonly used volume resonator for spin excitation (27) at low frequencies. Head sized birdcage resonators are typically designed with 12 or 16 rungs. If a birdcage coil was placed inside the ^{1}H dipole array, the performance of the latter would be greatly reduced due to shielding by the rungs of the birdcage. To mitigate this problem, several identical high impedance ^{1}H traps can be added to make the birdcage transparent at the ^{1}H frequency. However, these additional passive components not only reduce transmit efficiency, but would also make coil-tuning an arduous task. Alternatively, the number of rungs can be reduced or the birdcage can be replaced by a loop array to limit the shielding effect on the coil in the outer layer.

In this work, we adopted the loop array approach and constructed a four-channel [23]Na transceiver array on the 26 cm fiber-glass tube. Four large loops (15 cm × 18 cm) were symmetrically arranged on the tube, aligning the center of the loops with the dipoles. The copper tracks for the loops were etched on a flexible printed circuit laminate with 35 μm copper on a polyimide film (Krempel GmbH, Vaihingen, Germany). The gap between adjacent loops and hence the width of the individual loops was chosen based on coupling to non-neighboring elements and the inhomogeneity of the transmit field caused by the gaps. A 2D view of the transceiver array is shown in Figure 1. Each loop had a total of 12 capacitors of 39 pF and a variable capacitor in parallel with one of the fixed capacitors for frequency adjustment. The neighboring elements were inductively decoupled. Coupling between the non-neighboring elements was 4.7 dB due to the low frequency and the large size of the transmit elements. Hence, decoupling inductors were implemented in the non-neighboring coils and the inductors were connected using a 180° (cable + pi network) line. A shielded dual-tuned cable trap (105.7 MHz and 399.7
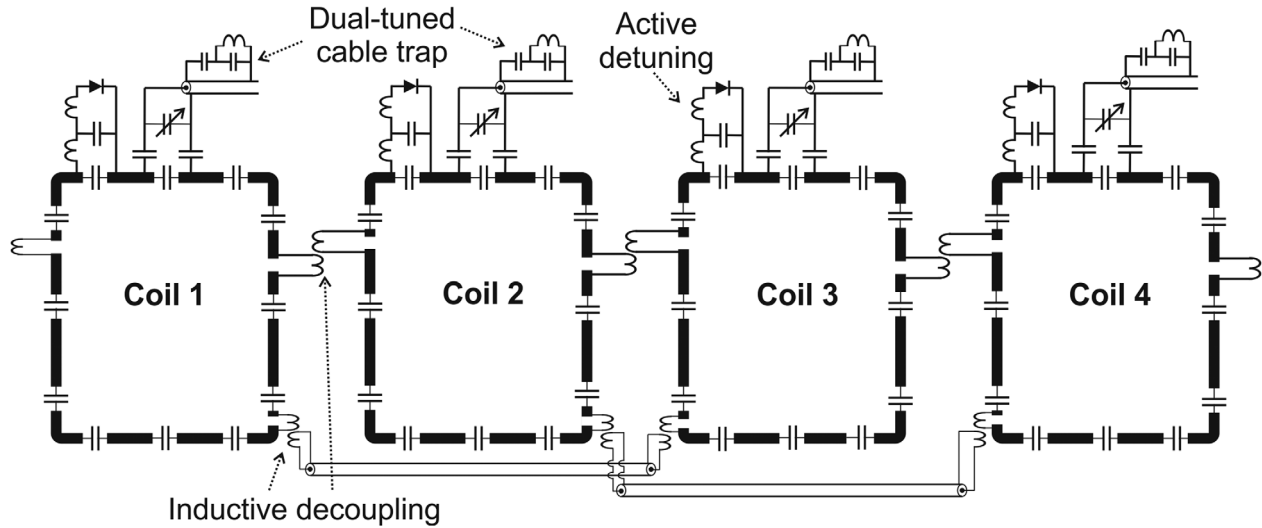
FIG. 1. 2D representation of the ^{23}Na transceiver array: The layout consists of four actively detunable loops of size 18 × 15 cm. The layout is scaled proportionately to show the large gaps between the loops with respect to the loop size.

MHz) was used at the coil input to reduce common mode currents (28). An active detuning circuit was implemented on a 100 Ω 90° T-network as shown in the schematic (Fig. 1) (29,30). An inside view of the implementation showing the ^{1}H dipole array and the ^{23}Na transceiver array is depicted in Figure 2. Coupling between the ^{23}Na loops and the ^{1}H dipoles was less than −43 dB.

To drive the coil in circularly polarized (CP) mode, four outputs of equal amplitude with relative phase offsets of 90° were generated using three quadrature hybrids as shown in the block diagram (Fig. 3a). A picture of the 1 × 4 hybrid splitter is shown in Figure 3b. A separate TR switch on each channel for transceive mode operation would occupy four receive channels and reduce the available number of channels for the receive array. Hence, the signal received from the transceiver array was added in phase before pre-amplification and fed to a single "combined-signal" channel (Fig. 3a). The additional loss in the receive path due to the signal combination before the pre-amplifier stage was approximately −0.5 dB. The subsequent reduction in SNR was

of less concern because the receive mode of the transceiver coil was mainly implemented to acquire a reference image for intensity correction (9). The "combined-signal" port of hybrid-4 (Fig. 3a) was terminated to 50 ohms during high power RF transmission and a protection circuit was added in front of the preamplifier to prevent high RF power from damaging it (Fig. 3c). The 1 × 4 hybrid splitter/combiner was realized on a RO4003C laminate (Rogers Corporation, AZ).

^{23}Na Receive Array

An SNR comparison for proton imaging at 3T between two size-matched 64-channel and 32-channel head coils demonstrated that central SNR remains unaffected when
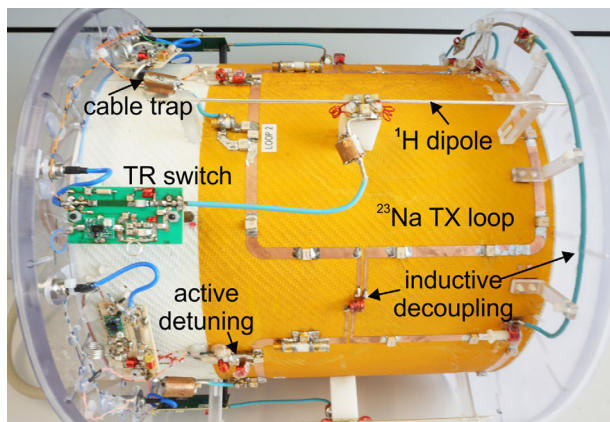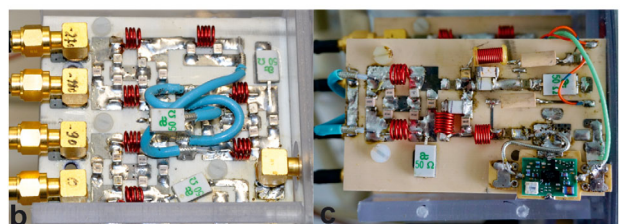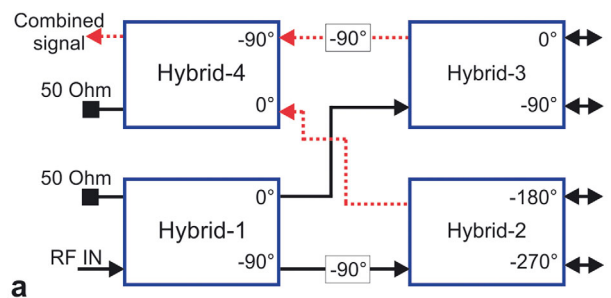

FIG. 3. The 1 × 4 hybrid splitter/combiner. **a**: Functional block diagram shows the combination of quadrature hybrids to generate four outputs with 90° phase offsets. The dotted line represents the received signal path. **b**: Implementation of the hybrid splitter. **c**: Picture of the hybrid combiner and preamplifier protection circuit.

FIG. 2. ^{23}Na transceive loops and ^{1}H dipoles: The dipoles are assembled above the ^{23}Na transceive loops on 25 mm spacers.
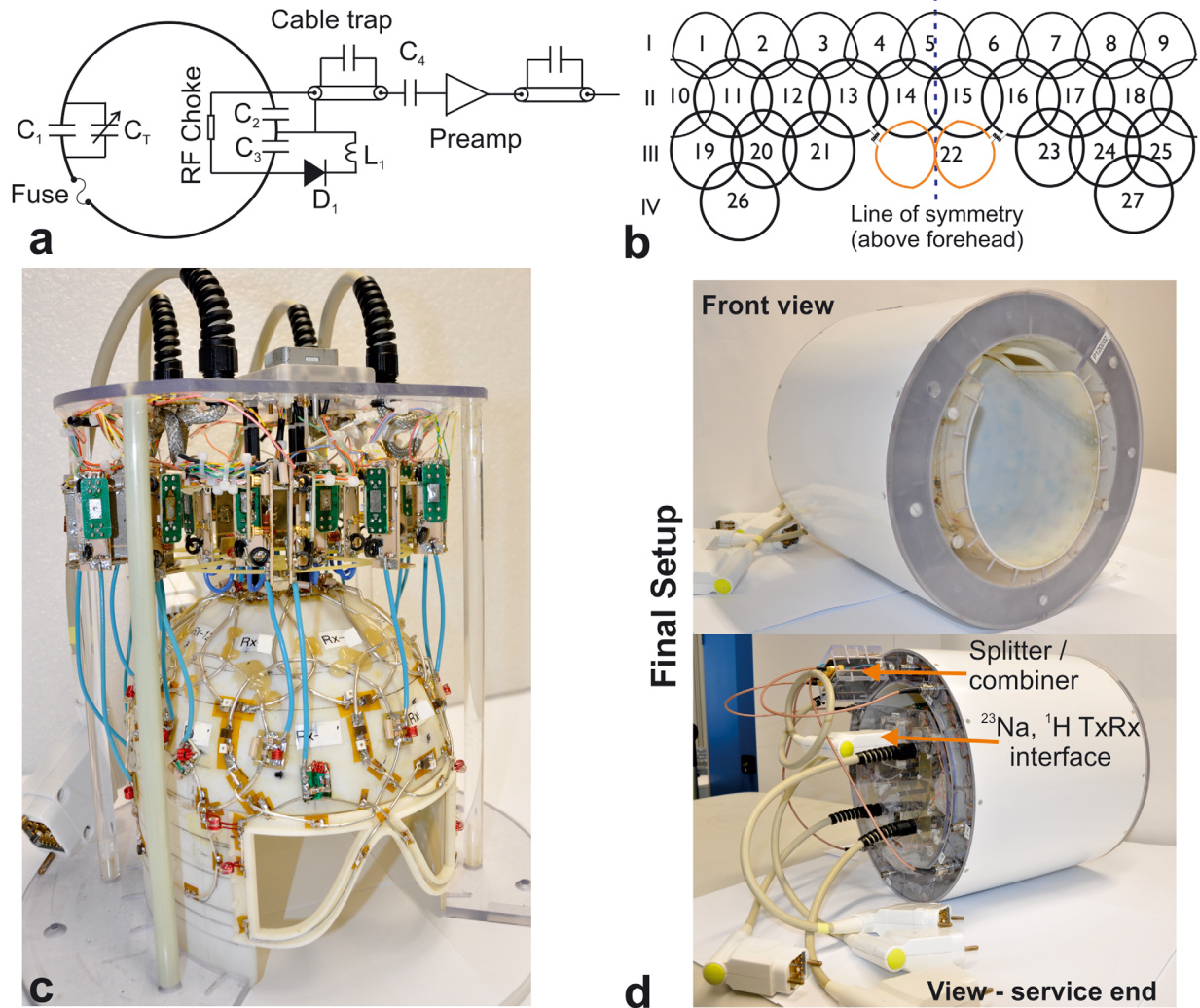
FIG. 4. a: Equivalent circuit of a single receive element. **b**: A 2-dimensional view of the receive coil layout. There are 26 circular loops and one "figure-8" coil (number 22) **c**: A photograph of the constructed receive array. The space inside the "figure-8" was used as eye cut-outs. **d**: Front view and view from the service-end of the fully assembled three layered coil. The service-end view shows the interfacing of the ^{23}Na and ^{1}H transceiver arrays to the scanner through the receive array assembly.

going to a higher number of receive channels even though the penetration depth of the individual loop elements decreases (18). Furthermore, it has been shown that a 32-channel receive array built on a tight fitting helmet can provide significant SNR improvement in the entire brain volume compared with a CP volume coil (17). These results are a motivation to build receive arrays with a higher number of receive elements, provided that sample noise dominance is maintained.

A 27-channel ^{23}Na receive array was constructed on a tight-fitting helmet (left/right: 185 mm, anterior/posterior: 220 mm, head/foot: 200 mm) fabricated using a 3D printer (Eden 250, Objet GmbH, Germany). The equivalent circuit of one receive element is shown in Figure 4a. The loops were constructed using 2 mm diameter silver plated copper wire (APX, Sarrians, France) and tuned to 105.7 MHz using two equally spaced fixed capacitors connected in series. For frequency adjustment, a variable capacitor C_T (2320-2, Johanson Manufacturing Corporation, NJ) was connected in parallel to a fixed capacitor

(C_1). The input capacitor was split further in series for impedance matching (C_2) and active detuning (C_3). Capacitor C_4 was used to adjust preamplifier decoupling. A PIN diode (MA4P7470F-1072T, M/A-COM, MA) in series with a hand wound inductor across C_3 completed the active detuning circuit. For secondary safety, in case of malfunction of the detuning circuitry, a protection fuse (Siemens Healthcare) was included.

Using the single receive element as a building block, 26 circular elements and a "figure-8" coil were arranged on the helmet as per the 2D view shown in Figure 4b. The 27 receive elements were arranged in four rows covering 180 mm along the z-direction. In each of the first two rows, nine elements formed two complete rings around the helmet. The 3rd row consisted of six loops and a "figure-8" coil above the eyes. The inner space in the "figure-8" coil acted as eye cut-outs (Fig. 4c). The "figure-8" coil was critically overlapped with two coils of the 2nd row (coils 14 and 15 in Figure 4b) and inductively decoupled with two more coils (coils 13 and 16 in

Figure 4b). There were two loops in the 4th row. The neighboring coils were critically overlapped as per the 2D scheme in Figure 4b to cancel mutual inductance (16). Coil tuning, impedance matching and adjacent element overlap were adjusted by loading the receive helmet with the head and shoulder phantom. While adjusting the impedance or the critical overlap between adjacent coils, all other elements were detuned. A pair of decoupled flux probes was used for measuring preamplifier decoupling, quality factor (Q) and active detuning.

The receive elements were connected to low input impedance preamplifiers (WanTcom Inc., MN). A pair of PIN diodes (MPP4203, Microsemi, MN) was added across the input of the high electron mobility transistor (HEMT) for high voltage protection. A cable trap was installed at the input as well as the output of the preamplifier. The control signal to actively detune the receive loops was fed through the RF cable using a bias-tee. The circuit boards with the receive electronics were mounted on a holder placed on top of the helmet, clearing the field of view (FOV) of the transceiver coil (Fig. 4c). This resulted in longer cables between the preamplifier and the input match capacitor for lower row elements. While additional cable length does not affect the impedance match, it shifts the preamplifier decoupling to lower frequencies. Reducing the value of capacitor C_4 compensated for this frequency shift. Furthermore, the long cables, especially the ones from the lower row elements to the preamplifiers were carefully routed away from the edges of the ^{23}Na transmit loops to minimize the interaction between the two ^{23}Na arrays.

Scanner Interface

Four of the 32 available receive channels were dedicated for ^{1}H imaging and the two ^{23}Na coils used the remaining 28 channels. In the standard configuration, the three arrays were assembled together and the coil was operated as a 32-channel coil. Alternatively, the ^{1}H dipole array could be plugged to the scanner together with the ^{23}Na transceiver array after demounting the ^{23}Na receive array. This modular feature was essential to quantify the influence of the receive array on the transmit efficiency of the ^{23}Na and ^{1}H transceive arrays. A photograph of the complete coil assembly is shown in Figure 4d.

Comparison Study

To validate the transmit and receive performance of the multinuclei imaging setup a conventional single tuned ^{23}Na birdcage coil was used as reference. The length and diameter of the 16-rung high pass birdcage coil were 21 cm and 25 cm, respectively. The birdcage coil was driven in quadrature using a home-built quadrature hybrid. The receive port of the quadrature hybrid was terminated to 50 ohms. Reception of the induced signal was accomplished by means of two TR switches installed between the outputs of the quadrature hybrid and the two feed points of the coil (31).

A head-only phantom filled with 2% w/w agar and 75 mM NaH$_2$PO$_4$ was built for the ^{23}Na SNR and transmit efficiency comparison study. The measured electrical properties were: permittivity (ε_r) = 80 and conductivity (σ) = 0.60 S/m. The same phantom was also constructed in the numerical domain.

Coil Simulation

Detailed models of the ^{23}Na transceiver array together with the ^{1}H dipole array and also of the reference birdcage coil was created and numerical simulations were performed using CST Studio Suite 2012 (CST, Darmstadt, Germany). The workflow presented in (32) was adopted for the numerical computation. The transmit coils were tuned in the RF circuit domain and the electromagnetic field distribution together with specific absorption rate (SAR) maps were calculated in the 3D EM domain. Peak averaged SAR over 10 g of tissue (SAR$_{10g}$) and safety excitation efficiency (SEE) ($B_1^+{}_{avg}$/$\sqrt{SAR_{10g}}$) were calculated for the two setups using the virtual family's "Duke" model (33). For in vivo measurements, the transmit power was limited based on the estimated SAR$_{10g}$ with an additional safety margin of 100%. Due to the geometrical complexity of the receive array and limitations in the 3D EM meshing, the receive array model was not incorporated in the numerical domain.

Transmit Field Characterization

The transmit field (B_1^+) of the ^{1}H dipoles was mapped using the actual flip angle imaging (AFI) technique (34) (FOV: 240 × 240 × 240 mm^3, matrix: 64 × 64 × 80, repetition times TR$_1$/TR$_2$: 12/100 ms, echo time (TE): 4 ms, bandwidth: 500 Hz/pixel, acquisition time: 7 min). B_1^+ mapping for ^{23}Na was performed with a phase sensitive mapping sequence (35). The sampling scheme was a stack of spirals with a nominal resolution of 3 × 3 × 3 mm^3. The k-space trajectories were calculated on the scanner by a time-optimal gradient design algorithm (36). The FOV was 250 mm and the acquisition time (TA) was 8 min. The field maps (simulated and measured) were normalized to the root-mean-square voltage measured by the scanner's RF supervision module. To assess the perturbation caused by the presence of the receive array, B_1^+ maps were acquired with and without the receive array in the transmit FOV. Because the tuning and matching condition of the ^{1}H and ^{23}Na transceiver arrays change when the ^{23}Na receive helmet is inserted or removed, the impedance match of the ^{1}H/^{23}Na transceive elements had to be adjusted for the two scan conditions. In both cases a match of better than −20 dB was achieved.

SNR Comparison

A pseudo multiple replica approach was used to estimate the achieved SNR (37). Noise data was acquired from each coil element without RF excitation and the standard deviation and correlation of the noise were determined. Based on these parameters synthetic correlated noise was generated and added to the k-space of a standard image acquisition, which consisted of a stack-of-spirals with the following imaging parameters: TE = 0.4 ms, TR = 50 ms, dwell time 5.5 μs, readout time 8 ms, 13 averages, 15 spiral interleaves per partition, 64
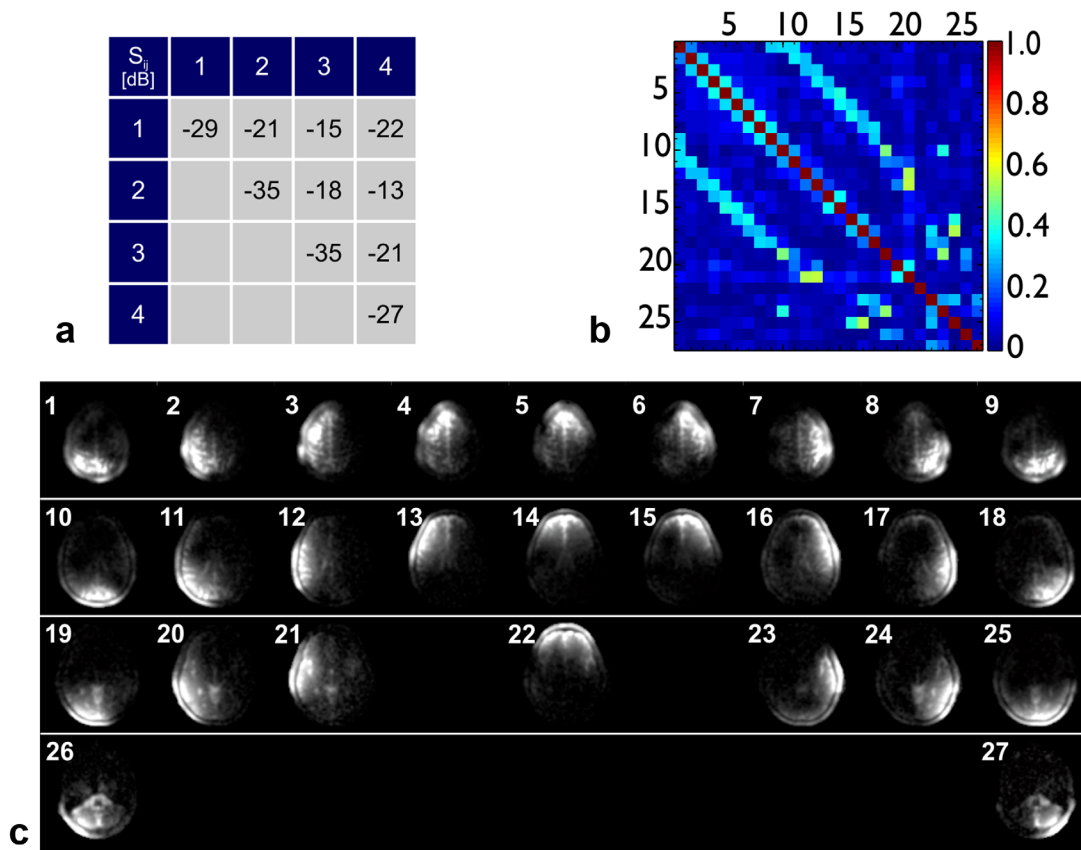
FIG. 5. a: S-parameter matrix of the four-channel ^{23}Na transceiver array measured in the presence of the actively detuned receive array. b: Noise correlation matrix of the ^{23}Na receive array. Average of all the off-diagonal values are 0.093 with maximum value of 0.54. c: Individual channel images acquired when all elements are active. The axial slices displayed pass through the middle of each row of coils on the receive helmet. The number on each image corresponds to the coil number displayed in Figure 4b.

partitions, resolution = $4 \times 4 \times 4$ mm^3, FOV = $240 \times 240 \times 256$ mm^3, nominal flip angle $40°$, TA = 10 min. Once the image was reconstructed, the process was repeated with a new set of synthetic noise. The standard deviation for each voxel through a stack of 500 replicas was calculated and used to generate SNR maps. Additionally, B_1^+ maps were acquired to correct for signal variations caused by deviations from the nominal flip angle. SNR differences due to signal saturation were neglected.

Imaging

Images acquired with phased arrays are degraded by the inhomogeneous sensitivity profile of the array elements. This modulation can be removed using the sensitivity encoding (SENSE) reconstruction formalism. The required coil sensitivity maps can be either obtained through self-calibration or preferentially deduced from a more homogenous reference image (9). In this study, the ^{23}Na coil sensitivity maps were calculated by dividing a low resolution image acquired with the receive array by a reference image from the transceiver array. The acquisition parameters for both images were identical: TE = 0.4 ms, TR = 45 ms, dwell time 3.6 μs, readout time 5 ms, 2 averages, 15 spiral interleaves per partition, 44 partitions, resolution = $4 \times 4 \times 5$ mm^3, TA = 1 min. Smooth-

ness of the sensitivity maps was enforced by locally fitting a low degree polynomial.

For ^{23}Na in vivo measurements, we scanned two healthy male volunteers (average age: 32 years) who had signed a written consent form approved by the institutional review board of the University of Tübingen. A 3D balanced steady state free precession (bSSFP) sequence with spiral readout was used to image the subject's brain. The sequence parameters were chosen as follows: TE = 2 ms, TR = 11 ms, dwell time 3 μs, readout time 3 ms, 10 averages, 100 spiral interleaves per partition, 56 partitions, FA = $40°$, Res = $2 \times 2 \times 4$ mm^3, FOV = $240 \times 240 \times 224$ mm^3 and TA = 10 min. The images were reconstructed on a standard PC using Matlab (The Mathworks, Natick, MA) by first performing Kaiser-Bessel gridding for each partition (38). Then, a 3D Hanning window was applied to the resampled signal to suppress high-frequency noise components. Finally, the filtered images were obtained by applying a 3D Fast Fourier transformation to the k-space.

To assess image quality achieved by the ^{1}H dipole array, gradient echo images were acquired with the following scan parameters: TE = 5 ms, TR = 1 s, 1.1 mm in-plane resolution, slice thickness = 2 mm, FOV = 220×220 mm^2, 30 slices and acquisition time of 3 min in each orientation.
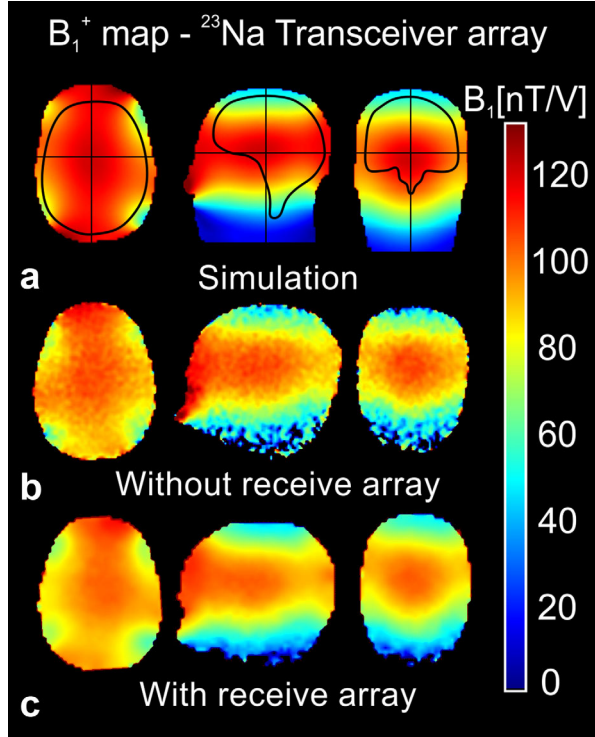
FIG. 6. ^{23}Na B_1^+ maps. **a**: Central axial, sagittal and coronal slices of the simulated field maps. A brain mask is superimposed to estimate the transmit efficiency. **b**: Measured field maps in the transceiver mode acquired without the receive array. In the superimposed volume, the measured mean B_1^+ is 13% weaker than in simulation. **c**: Field maps acquired in the presence of the 27-channel receive array. Measured B_1^+ in the center of the coil reduced from 105 nT/V to 100 nT/V with the receive array in the transmit FOV.

RESULTS

^{23}Na Transceiver Array

The unloaded Q (Q_{UL}) of a single ^{23}Na transceive loop with 12 series capacitors and the decoupling inductors was 248. Loaded Q (Q_L), measured by loading the transmit element with the head and shoulder phantom, was 147. Active detuning was −36 dB with 50 mA of DC. The S-parameter matrix of the four-element ^{23}Na transceiver array is shown in Figure 5a. Inductive decoupling circuits between the nonadjacent coils improved the isolation from −4.7 dB to at least −12 dB.

The phase error in the 1 × 4 hybrid splitter, designed to drive the array in CP mode, was within ± 1.5° and the insertion loss was 0.3 dB at 105.7 MHz. In transmit mode, the preamplifier protection circuit in the combined-signal port (Fig. 3a) provided better than 40 dB isolation.

Receive Array

Q_{UL}, measured on a 90 mm diameter representative circular loop constructed with components as shown in Figure 4a, was 224. For Q measurements, the coaxial cable attached to the coil input was removed. Q_L was 48 when the coil was loaded with the head and shoulder phantom placed at 8 mm from the coil. An impedance
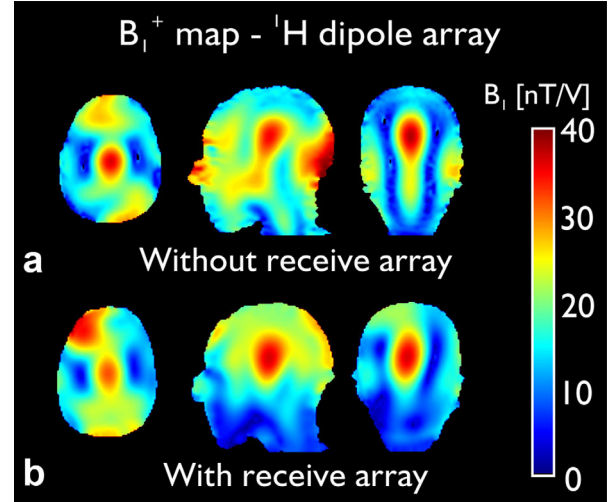

FIG. 7. ^{1}H B_1^+ maps. **a**: Measured B_1^+ map of the ^{1}H dipole array measured in presence of the actively detuned ^{23}Na transceive array, but without the 27-channel receive array. The B_1^+ profile is symmetric and the longitudinal coverage is sufficient to excite the whole brain. **b**: Addition of the ^{23}Na receive array leads to an altered B_1^+ distribution.

match of at least −15 dB was achieved on each coil element and active detuning was better than 35 dB. The isolation, measured in loaded condition, between adjacent overlapping coils was between −9 and −12 dB. The low input impedance preamplifiers provided an additional 15 to 18 dB decoupling. A single capacitor placed in parallel across the input for matching (Fig. 4a) resulted in a large capacitor value ($C_2 = 120$ pF) and a subsequent lower preamplifier decoupling. The noise correlation matrix of the receive array is shown in Figure 5b. The average of all the off-diagonal values was 0.093 and the maximum value in the matrix was 0.54. Uncombined bSSFP in vivo images, acquired with all receive elements active, are shown in Figure 5c to demonstrate the isolation between coil elements. The number on the individual images corresponds to the coil element numbering displayed in Figure 4b. Because the coil elements are arranged in multiple rows on the helmet, an axial slice through the middle of each row is shown.

Transmit Field Characterization

Figure 6a shows the simulated field maps for the ^{23}Na transceiver array in the head-only phantom. The crosshairs in the individual maps represent the displayed slices through the center of the coil in each scan plane. A brain mask was superimposed on the 3D B_1^+ map and the transmit efficiency was estimated in this volume. The numerical model predicted a mean transmit efficiency of 92 nT/V inside the brain mask. The actual field strength (Fig. 6b), measured without the receive array present, was approximately 13% weaker (80 nT/V) than predicted by the simulations. Except for this scaling factor, the simulated and measured B_1^+ field distributions match well. When the ^{23}Na receive array was added (Fig. 6c), the B_1^+ distribution remained nearly unaffected. In the center of the coil, the peak value was 105 nT/V in
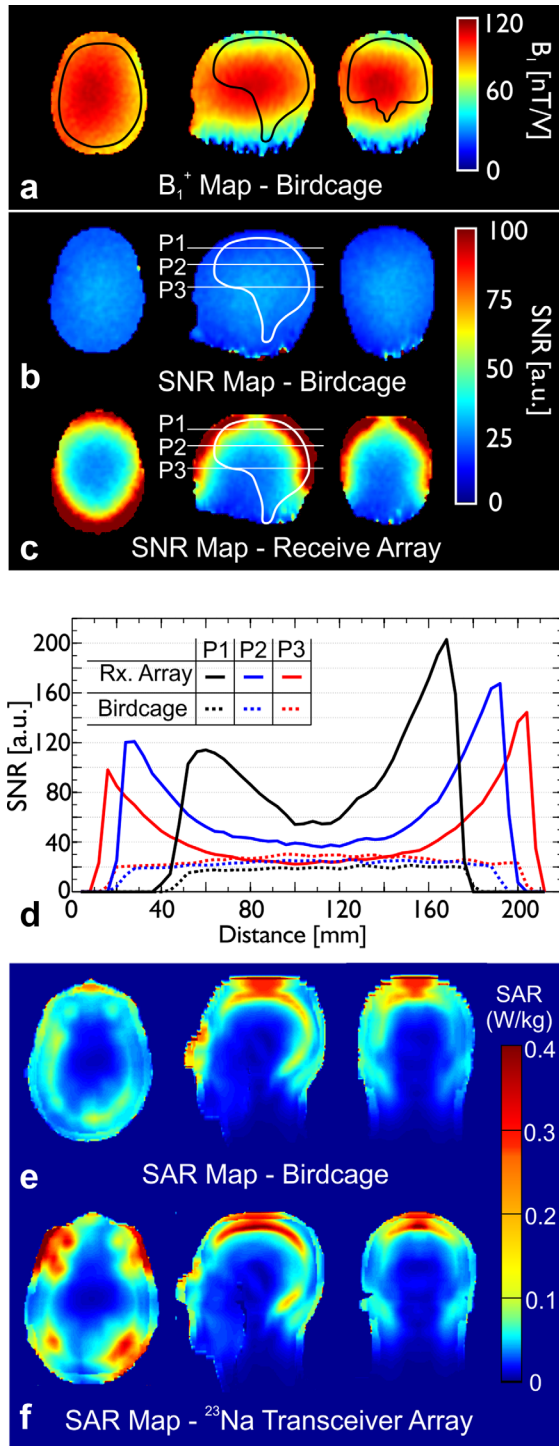
FIG. 8. **a**: Measured B_1^+ maps of the ^{23}Na birdcage coil. ^{23}Na transmit efficiency of the three layered coil is 17% weaker than the birdcage in the superimposed brain volume. For direct comparison to Figure 6, the same color map is used. **b**: SNR map of the ^{23}Na birdcage coil. **c**: SNR maps for the 27-channel receive array acquired with the same phantom. **d**: SNR profiles passing approximately through the middle of the top three rows of the receive array. In P1 and P2, the central SNR gain is a factor of 2.75 and 1.48, respectively. In P3, the maximum SNR for the birdcage is 28 and the minimum SNR for the array is 23. **e**: Estimated SAR_{10g} map for the birdcage in the "Duke" model. Maximum value: 0.34 W/kg. **f**: Estimated SAR_{10g} for ^{23}Na transceive array. Maximum value: 0.6 W/kg.

the transceive mode and 100 nT/V when the receive array was in place. In the brain mask the mean transmit efficiency was 80 nT/V demonstrating minimal loss due to the addition of the receive array. Note that the B_1^+ maps shown in the Figure 6c were acquired with the 27-channel receive array and hence exhibit higher SNR.

Figure 7a shows the B_1^+ distribution of the ^{1}H dipole array in the head and shoulder phantom. The AFI maps acquired in the presence of ^{23}Na transceiver array demonstrate sufficient longitudinal coverage and exhibited symmetric distribution as shown in the axial and coronal orientations. However, when the ^{23}Na receive array was inserted, the distribution was altered due to the low impedance ^{23}Na receive array elements and cables inside the transmit FOV (Fig. 7b). Altering the individual cable routing to minimize the influence on the ^{1}H transmit field is not only a laborious task, but can also compromise the performance of the ^{23}Na transceiver coil. Nevertheless, the image quality and coverage offered by the dipole array was sufficient for the intended purpose.

Comparison to Birdcage Coil

Figure 8a shows the B_1^+ map acquired with the reference birdcage coil using the head-only phantom. In the volume inside the brain mask, transmit efficiency of the three-layered coil is 17% weaker than the birdcage. Note that the birdcage is slightly smaller in diameter (25 cm versus 26 cm) and does not have loss contributions from the active detuning circuitry or from the presence of the ^{23}Na receive array in the transmit FOV.

The SNR maps shown in Figure 8b and 8c demonstrate the superior receive performance of the 27-channel ^{23}Na receive array compared with the single-tuned birdcage coil. The SNR gain was quantified using SNR profiles passing through the middle of each of the top three rows of the receive array (Fig. 8d). Profile P1, through the middle of the top row covering the dome of the helmet, revealed a 2.8-fold SNR improvement in the center of the slice. The SNR gain in profile P2, through the middle of the second row, was 1.5-fold in the center of the slice and significantly higher close to the surface coils. Along profile P3, the peak central SNR for the birdcage was 28. The minimum SNR for the receive array along profile P3 was 23 and the maximum SNR in the periphery was more than five times higher than the SNR achieved by the birdcage.

The estimated SAR_{10g} maps for the Duke model are shown in Figures 8e and 8f. Note that the maximum electric field is along the end-ring for the birdcage and along the edges of the loops for the ^{23}Na transceiver array. The peak SAR_{10g} and SEE (in the whole head of Duke model) for the birdcage and the ^{23}Na transceiver array were 0.34 W/kg; 1.46 µT/$\sqrt{(W/kg)}$ and 0.6 W/kg; 1.21 µT/$\sqrt{(W/kg)}$, respectively.

In Vivo Results

In vivo ^{23}Na images acquired using this coil configuration are shown in Figure 9. The homogeneous reference image from the ^{23}Na transceiver array and the corresponding slice acquired with identical parameters using the ^{23}Na receive array are shown in Figures 9a and 9b,
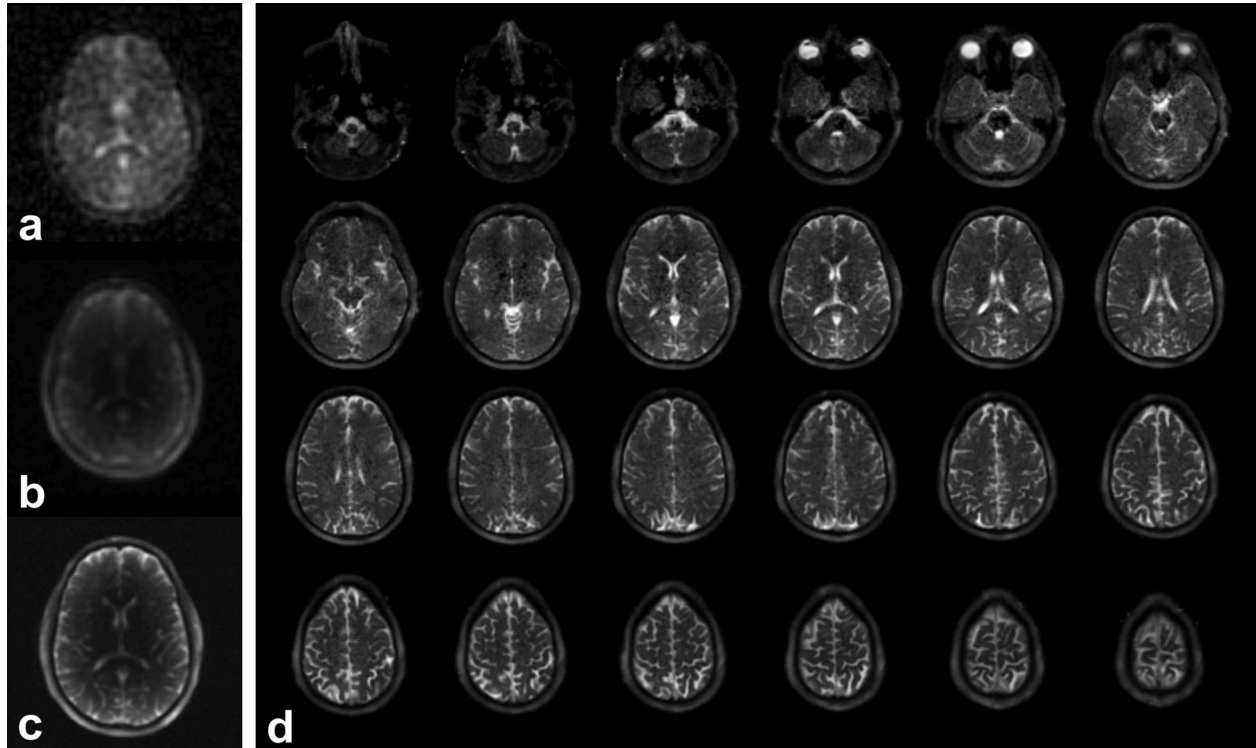
FIG. 9. In vivo ^{23}Na images. **a**: Reference image acquired with the four-channel ^{23}Na transceiver array. **b**: The same image as in (a), but acquired with the 27-channel receive array. **c**: bSSFP acquisition without intensity correction. (d) Sensitivity corrected bSSFP images. Scan parameters: TE = 2 ms, TR = 11 ms, FA = 40°, Resolution = 2 × 2 × 4 mm^3 and acquisition time = 10 min.

respectively. Even though the SNR of the reference images was moderate, they still provided sufficient information to calculate coil sensitivity maps. A single slice, without intensity correction, from the bSSFP acquisition using the receive array and reconstructed using root sum-of-squares is shown in Figure 9c. As expected, the signal intensity is higher close to the surface coils and weaker in the center.

Figure 9d shows multiple slices of the sensitivity corrected bSSFP image acquired in 10 min with a resolution of 2 × 2 × 4 mm^3. The intensity variation due to the coil sensitivity profile could be eliminated. Excellent spatial resolution with good SNR could be achieved, especially in the cortical brain. In the center of the brain, the reduced sensitivity of the 27-channel array and the SENSE reconstruction led to moderate but still acceptable noise enhancement.

In vivo ^{1}H images acquired with the dipole array in the presence of the two ^{23}Na arrays is shown in Figure 10. The asymmetry introduced by the ^{23}Na receive array
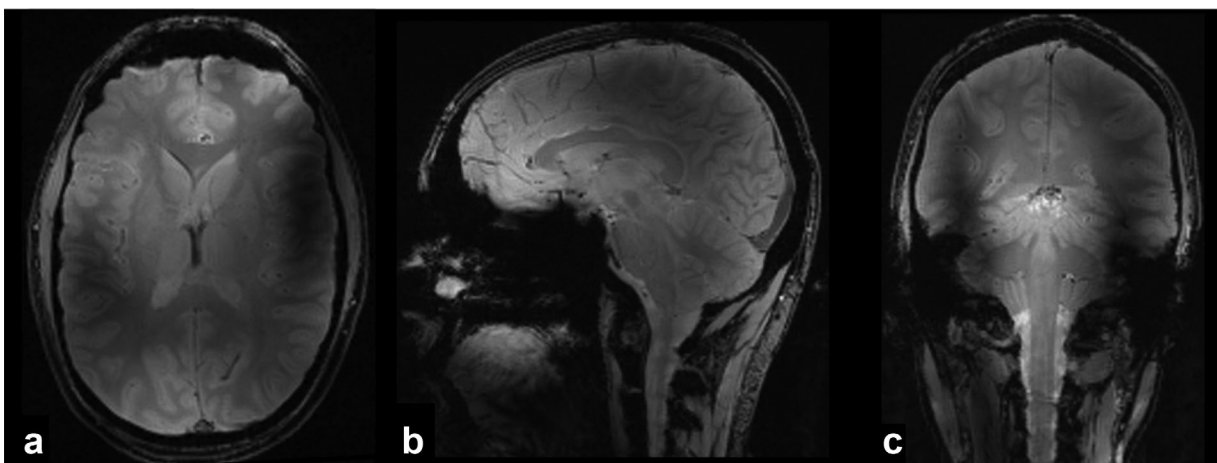

FIG. 10. **a–c**: In vivo gradient echo images acquired with the four-channel ^{1}H dipole array in the presence of the ^{23}Na transmit and receive arrays. In-plane resolution: 1.1 mm, slice thickness: 2 mm acquisition time: 3 min for each orientation.

as noticed in Figure 7b can be seen on the axial slice shown in Figure 10a. The ^{1}H dipoles provided whole brain coverage at 399.7 MHz as shown in the sagittal (Fig. 10b) and coronal slices (Fig. 10c). These results demonstrate the utility of the ^{1}H dipole array for the intended purpose of fast B_0 mapping and anatomical localization in the presence of the [23]Na transmit and receive arrays.

DISCUSSION AND CONCLUSION

The coil arrangement presented in the current work was conceived to fulfill design criteria such as maximizing coil performance at [23]Na frequency, acquire a homogeneous [23]Na reference image for intensity correction and ensuring whole brain coverage at the ^{1}H frequency for B_0 shimming and anatomical localization. Several alternatives were investigated to meet these requirements. Initial experiments using a combination of a 16-rung [23]Na birdcage coil and a four-element ^{1}H dipole array resulted in an almost total loss of the ^{1}H signal in the center of the birdcage due to the shielding effect of the rungs.

Ultimate SNR in center of a sphere was achieved with four coils evenly surrounding the volume (at 64 MHz) (39). More coils were required to reach the ultimate SNR in the center of the sphere at higher frequencies. Furthermore, the peripheral SNR approaches the ultimate achievable SNR with higher number of coils (39). As demonstrated in the SNR maps (Fig. 8d), significant gain in [23]Na SNR was achieved in almost the entire brain volume. In the center of the 27-channel receive array, the SNR was only marginally lower than the peak SNR of the birdcage. The coil elements in the receive array were arranged on the helmet surface to follow the contours of the brain anatomy, resulting in just two elements in the fourth row. Although it is impractical to build receive arrays covering spherical volumes, more coil elements covering the helmet surface in the fourth row, either by adding more receive channels or by rearranging the 27 coil elements should boost the central SNR.

The performance of the three-layered coil was validated and the experimental results show that the proof-of-concept coil meets the various demands of a multinuclei imaging setup. Transmit and receive performance of the coil at the [23]Na frequency was not compromised. The in vivo [23]Na images, acquired in only ten minutes, show level of detail not previously achieved. The challenging task of whole brain coverage for ^{1}H images, despite the high frequency and the presence of the [23]Na arrays, could be accomplished. Last but not least, this combination of three coil arrays can be readily adapted for other nuclei at 9.4T or for multinuclei applications at UHF.

ACKNOWLEDGMENT

REFERENCES

1. Ouwerkerk R, Bleich KB, Gillen JS, Pomper MG, Bottomley PA. Tissue sodium concentration in human brain tumors as measured with [23]Na MR imaging. Radiology 2003;227:529–537.
2. Thulborn KR, Davis D, Adams H, Gindin T, Zhou J. Quantitative tissue sodium concentration mapping of the growth of focal cerebral tumors with sodium magnetic resonance magnetic resonance imaging. Magn Reson Med 1999;41:351–359.
3. Pilkinton DT, Clark CM, Elliott MA, Witschey WR, Borthakur A, Reddy R. Sodium MR imaging detection of mild Alzheimer disease: preliminary study. J Neuroradiol 2009;30:978–984.
4. Thulborn KR, Gindin T, Davis D, Erb P. Comprehensive MR imaging protocol for stroke management: tissue sodium concentration as a measure of tissue viability in nonhuman primate studies and in human studies. Radiology 1999;213:156–166.
5. Keltner JR, Carlson W, Roos MS, Wong TS, Wong TL, Budinger TF. Electromagnetic fields of surface coil in vivo NMR at high frequencies. Magn Reson Med 1991;22:467–480.
6. Wiesinger F, Boesiger P, Pruessmann KP. Electrodynamics and ultimate SNR in parallel MR imaging. Magn Reson Med 2004;52:376–390.
7. Vaughan JT, Garwood M, Collins CM, et al. 7T vs. 4T: RF power, homogeneity and signal-to-noise comparison in head images. Magn Reson Med 2001;46:24–30.
8. Pohmann R, Scheffler K. Brain imaging with 7T vs. 9.4T: a direct comparison of MR parameters and SNR. In Proceedings of the 22nd Annual Meeting of ISMRM, Milan, Italy, 2014. Abstract 1421.
9. Qian Y, Zhao T, Wiggins GC, Wald LL, Zheng H, Weimer J, Boada FE. Sodium imaging of the human brain at 7T with 15-channel array coil. Magn Reson Med 2012;68:1808–1814.
10. Lu A, Atkinson IC, Claiborne TC, Damen FC, Thulborn KR. Quantitative sodium imaging with a flexible twisted projection pulse sequence. Magn Reson Med 2010;63:1583–1593.
11. Atkinson IC, Lu A, Thulborn KR. Preserving the accuracy and resolution of the sodium bioscale from quantitative sodium MRI during intrasubject alignment across longitudinal studies. Magn Reson Med 2012;68:751–761.
12. Romanzetti S, Mirkes CC, Fiege DP, Celik A, Felder J, Shah NJ. Mapping tissue sodium concentration in the human brain: a comparison of MR sequences at 9.4 Tesla. Neuroimage 2014;96:44–53.
13. Shen GX, Wu JF, Boada FE, Thulborn KR. Experimentally verified, theoretical design of dual-tuned, low-pass birdcage radiofrequency resonators for magnetic resonance imaging and magnetic resonance spectroscopy of human brain at 3.0 Tesla. Magn Reson Med 1999;41:268–275.
14. Shen GX, Boada FE, Thulborn KR. Dual-frequency, dual-quadrature, birdcage design with identical B1 pattern for sodium imaging of the human brain at 1.5 T. Magn Reson Med 1997;38:717–725.
15. Van de Moortele PF, Akgun C, Adriany G, Moeller S, Ritter J, Collins CM, Smith MB, Vaughan JT, Ugurbil K. B1 destructive interferences and spatial phase patterns at 7T with a head transceiver array coil. Magn Reson Med 2005;54:1503–1518.
16. Roemer PB, Edelstein WA, Hayes CE, Souza SP, Mueller OM. The NMR phased array. Magn Reson Med 1990;16:192–225.
17. Wiggins GC, Triantafyllou C, Potthast A, Reykowski A, Nittka M, Wald LL. 32-channel 3 Tesla receive-only phased array head coil with soccer-ball element geometry. Magn Reson Med 2006;56:216–223.
18. Keil B, Blau JN, Biber S, Hoecht P, Tountcheva V, Setsompop K, Triantafyllou C, Wald LL. A 64-channel 3T array coil for accelerated brain MRI. Magn Reson Med 2013;70:248–258.
19. Wiggins GC, Polimeni JR, Potthast A, Schmitt M, Alagappan V, Wald LL. 96-channel receive-only head coil for 3 Tesla: design, optimization and evaluation. Magn Reson Med 2009;62:754–762.
20. Wiggins GC, Brown R, Fleysher L, Zhang B, Stoeckel B, Inglese M, Sodickson DK. A nested dual frequency birdcage/stripline coil for sodium/proton brain imaging at 7T. In Proceedings of the 18th Annual Meeting of ISMRM, Stockholm, Sweden, 2010. Abstract 1500.
21. Brown R, Madelin G, Lattanzi R, Chang G, Regatte RR, Sodickson DK, Wiggins GC. Design of a nested eight-channel sodium and four-channel proton coil for 7T knee imaging. Magn Reson Med 2013;70:259–268.
22. Kaggie JD, Hadley R, Badal J, Campbell JR, Park DJ, Parker DL, Morell G, Newbould RD, Wood AF, Bangerter NK. A 3T sodium

and proton composite array breast coil. Magn Reson Med 2014;71: 2231–2242.

23. Mirkes CC, Hoffmann J, Shajan G, Pohmann R, Scheffler K. High resolution quantitative sodium imaging at 9.4 Tesla. Magn Reson Med 2015;73:342–351.

24. Wiggins GC, Zhang B, Lattanzi R, Chen G, Sodickson D. The electric dipole arrray: an attempt to match the ideal current pattern for central SNR at 7 Tesla. In Proceedings of the 2oth Annual Meeting of ISMRM, Melbourne, Australia, 2012. Abstract 541.

25. Shajan G, Hoffmann J, Budde J, Adriany G, Ugurbil K, Pohmann R. Design and evaluation of an RF front-end for 9.4T human MRI. Magn Reson Med 2011;66:596–604.

26. Beck BL, Jenkins KA, Rocca JR, Fitzsimmons JR. Tissue-equivalent phantoms for high frequencies. Concepts Magn Reson Part B 2004;20: 30–33.

27. Hayes CE, Edelstein WA, Schenk JF, Mueller OM, Eash M. An efficient, highly homogeneous radiofrequency coil for whole-body NMR imaging at 1.5T. J Magn Reson 1985;63:622–628.

28. Avdievich NI. Transceiver-phased arrays for human brain studies at 7T. Appl Magn Reson 2011;41:483–506.

29. Nabetani A, Watkins RD. Dynamic disabling switch development for 7T self-shielded birdcage coil. In Proceedings of the 12th Annual Meeting of ISMRM, Kyoto, Japan, 2004. Abstract 1574.

30. Avdievich NI, Bradshaw K, Kuznetsov AM, Hetherington HP. High-field actively detunable transverse electromagnetic (TEM) Coil with low bias voltage for high power RF transmission. In Proceedings of the 22nd Annual Meeting of ISMRM, Berlin, Germany, 2007. Abstract 238.

31. Sorgenfrei BL, Edelstein WA. Optimizing MRI signal-to-noise ratio for quadrature unmatched RF coils: two preamplifiers are better than one. Magn Reson Med 1996;36:104–110.

32. Hoffmann J, Shajan G, Scheffler K, Pohmann R. Numerical and experimental evaluation of RF shimming in the human brain at 9.4T using a dual-row transmit array. Magn Reson Mater Phys 2014;27:373–386.

33. Christ A, Kainz W, Hahn EG, et al. The virtual family–development of surfacebased anatomical models of two adults and two children for dosimetric simulations. Phys Med Biol 2010;55:N23–N38.

34. Yarnykh VL. Actual flip-angle imaging in the pulsed steady state: a method for rapid three-dimensional mapping of the transmitted radiofrequency field. Magn Reson Med 2007;57:192–200.

35. Allen SP, Morrell GR, Peterson B, Park D, Gold GE, Kaggie JD, Bangerter NK. Phase-sensitive sodium B_1 mapping. Magn Reson Med 2011;65:1126–1131.

36. Lustig M, Kim SJ, Pauly JM. A fast method for designing time-optimal gradient waveforms for arbitrary k-space trajectories. IEEE Trans Med Imaging 2008;27:866–873.

37. Robson PM, Grant AK, Madhuranthakam AJ, Lattanzi R, Sodickson DK, McKenzie CA. Comprehensive quantification of signal-to-noise ratio and g-factor for image-based and k-space-based parallel imaging reconstructions. Magn Reson Med 2008;60:895–907.

38. Jackson JI, Meyer CH, Nishimura DG, Macovski A. Selection of a convolution function for Fourier inversion using gridding. IEEE Trans Med Imaging 1991;10:473–478.

39. Wiesinger F, De Zanche N, Pruessmann KP. Approaching ultimate SNR with finite coil arrays. In Proceedings of the 22nd Annual Meeting of ISMRM, Miami Beach, Florida, USA, 2005. Abstract 672.

2.4 Publication No. 4

Rat Brain MRI at 16.4 T Using a Capacitively Tunable Patch Antenna in Combination with a Receive Array

G. Shajan, Jens Hoffmann, David Zsolt Balla, Dinesh K Deelchand, Klaus Scheffler and Rolf Pohmann, NMR Biomed. 2012 25: 1170–1176

Rat brain MRI at 16.4T using a capacitively tunable patch antenna in combination with a receive array

G. Shajan[a]*, Jens Hoffmann[a], Dávid Z. Balla[a], Dinesh K. Deelchand[b], Klaus Scheffler[a,c] and Rolf Pohmann[a]

For MRI at 16.4T, with a proton Larmor frequency of 698 MHz, one of the principal RF engineering challenges is to generate a spatially homogeneous transmit field over a larger volume of interest for spin excitation. Constructing volume coils large enough to house a receive array along with the subject and to maintain the quadrature symmetry for different loading conditions is difficult at this frequency. This calls for new approaches to RF coil design for ultra-high field MR systems. A remotely placed capacitively tunable patch antenna, which can easily be adjusted to different loading conditions, was used to generate a relatively homogeneous excitation field covering a large imaging volume with a transversal profile similar to that of a birdcage coil. Since it was placed in front of the animal, this created valuable free space in the narrow magnet bore around the subject for additional hardware. To enhance the reception sensitivity, the patch antenna was combined with an actively detunable 3-channel receive coil array. In addition to increased SNR compared to a quadrature transceive surface coil, we were able to get high quality gradient echo and spin-echo images covering the whole rat brain. Copyright © 2012 John Wiley & Sons, Ltd.

Keywords: patch antenna; remote transmission; MRI at 16.4T

INTRODUCTION

In magnetic resonance imaging, radio frequency (RF) coils are used to produce RF magnetic fields to excite the nuclei as well as for acquisition of the induced NMR signal. Volume coils that generate a uniform excitation field are often used in combination with single or multiple surface coils for detection. Receive coil arrays have become widespread in MRI due to the increased sensitivity offered by a multiple of mutually decoupled smaller coil elements arranged over a larger volume of interest (1, 2) as well the possibility to accelerate image acquisition using parallel imaging (3–5).

The push towards higher static magnetic (B_0) field strength in search of higher signal to noise ratio (SNR) increases the RF (B_1) field frequency. Several issues limit translating the RF coil designs that are highly successful at clinical field strengths to small animal imaging at 16.4T with a proton Larmor frequency of 698 MHz. In addition to the special care that must be taken to limit the radiative and reactive losses in coil designs specific to high frequencies, the principal issue is the challenges involved in generating a spatially homogeneous RF excitation field covering a larger field of view (FOV).

As RF coils approach wavelength dimensions, the phase change of the electric current on coil conductors cannot be ignored. In addition, electrically symmetric volume resonator structures (6), mainly used for producing a homogeneous excitation field, must be large enough to house the receive array and the subject. The larger coil conductors have large self-inductance and high resonance frequency is achieved by using smaller capacitance values and by series distribution of capacitors. Hence, minor variations in the component values along with stray capacitances can have a significant impact on the electrical

symmetry of volume resonators. Furthermore, the tune and match of the coil must be adjusted at the beginning of an experiment because the coil parameters are very sensitive to the size of the subject and its position inside the coil. Thus, it becomes a highly challenging task to build volume resonators for proton imaging at 16.4T and to maintain their quadrature symmetry such that they are robust enough across varying sizes and positions of the subject. Because of these difficulties and limited space, most RF coil designs for small animal MRI at such high field strengths are transceiver coils either with a single channel or as array, which constrain the use of spin-echo sequences due to the inhomogeneous transmit field (7,8).

---

* Correspondence to: G. Shajan, High-Field Magnetic Resonance Center, MPI for Biological Cybernetics, Spemannstr 41, 72076-Tuebingen, Germany. Phone: +49 7071601734, Fax: +49 7071601702.
  E-mail: shajan.gunamony@tuebingen.mpg.de

a G. Shajan, J. Hoffmann, D. Z. Balla, K. Scheffler, R. Pohmann
   High-Field Magnetic Resonance Center, Max Planck Institute for Biological Cybernetics, Tuebingen, Germany

b D. K. Deelchand
   Center for Magnetic Resonance Research, University of Minnesota, USA

c K. Scheffler
   Department for Neuroimaging, University of Tuebingen, Germany

It has recently been shown that a circularly polarized patch antenna can be used as a simple and robust substitute for conventional volume coils for spin excitation in the human brain at 7T and above, with the potential to provide a somewhat more uniform excitation in addition to the extended coverage along the direction of propagation (9,10). In the original approach, termed traveling wave imaging, the RF shield in the magnet bore acts as a waveguide to propagate signal from a remotely placed antenna to the subject, provided the cutoff frequency of the waveguide is lower than the Larmor frequency (11,12). Our 16.4T magnet bore has a cutoff frequency of 1.46 GHz for the dominant mode and hence does not support wave propagation at 698 MHz but causes considerable attenuation of the field with increasing distance from the antenna. However, it has been shown (9,13) that in such cases, the transmit efficiency can be strongly improved by moving the antenna close to the subject without affecting B_1^+ field homogeneity and the dimensions of the excited volume. As a consequence of the close proximity, the transmit antenna is strongly influenced by the load and thus a mechanism to easily tune and match the antenna to different loads, e.g. realized by using variable capacitors, is required (13,14). In this study, we used the spatially homogeneous near-field of this modified patch antenna for spin excitation in combination with a receive-only coil array for highly sensitive signal reception at 16.4T.

MATERIALS AND METHODS

Experiments were performed on a horizontal bore 16.4T magnet (Magnex Scientific, UK) interfaced to a BioSpec® spectrometer (Bruker BioSpin MRI GmbH, Germany). The gradient and shim coil system had a diameter of 120 mm and was capable of generating gradient strengths of 1000 mT/m within a switching time of 212 μs. The MR system had eight receive channels and a single RF power source with a maximum power output of 1 kW. Additional measurements were performed on a similar scanner with a Varian console and otherwise comparable configuration (Center of Magnetic Resonance Research, University of Minneapolis, Minnesota).

Tissue equivalent phantoms (15) having equal electrical properties as average brain or muscle tissue at 698 MHz were used for characterizing the coil parameters and for imaging experiments. *In vivo* measurements were performed on one healthy rat (850 g) under isoflurane anaesthesia (1.5%–2%). Animal experiments were in accordance with NIH animal protection guidelines and approved by the local authorities.

Transmit antenna design and construction

A conventional patch antenna consists of a radiating patch and a ground plane separated by a low loss dielectric substrate. In the original design, the size of the antenna depends mainly on the permittivity of the substrate as well as the operating frequency (16). A capacitively tunable patch antenna (13), that provides a mechanism to easily tune and match the antenna to different loads, was designed using a 6-mm thick alumina slab (99.7% purity, MicroCeram, Meissen, Germany) with a diameter of 110 mm. This substrate was selected due to its low loss and its high relative permittivity ($\varepsilon_r \approx 9.6$, loss factor $\tan\delta \approx 0.0003$), which was necessary to make the antenna sufficiently small to fit inside the magnet bore. The radiating patch, which was 60-mm in diameter, and the ground plane were realized using single sided

copper polyimide laminate (5-μm copper on 25-μm film, Novaclad® laminate, Sheldahl, MN, USA). To reduce eddy currents, the copper layer on the laminate was meshed using standard circuit board fabrication techniques to form a netted layer of copper (0.3-mm linewidth, 0.5-mm spacing).

For circular polarization, two coaxial line feeds with an angular offset of 90°, with their inner conductors attached to the radiating patch and their outer conductors connected to the ground plane of the patch antenna, were used. A capacitively terminated patch antenna can be best visualized as two linear microstrip half lambda transmission line elements (17) driven in quadrature. The equivalent circuit of one of those linear elements is shown in Figure 1a. The decoupling between the two feed-ports can be influenced by adjusting the balance between the tuning capacitors C_{T1} and C_{T2} and therefore, the current distribution on the patch (9). In transmit only mode, PIN diodes detuned the antenna during signal acquisition.

The reflection (S_{11}) and transmission (S_{21}) coefficients of the patch antenna were heavily influenced by the gradient coil when the antenna was moved into the bore. To avoid this, the antenna was wrapped with a 5-cm long copper laminate as shown in Figure 1b. Four slots were cut along the outer edge for routing the coaxial cables from the receive coil to the receiver electronics placed behind the antenna. To accomplish quadrature excitation, a homebuilt quadrature hybrid (Microstrip branch line coupler, Substrate: RO4003C, Rogers Corporation, AZ, USA) was used to split the transmit RF into two outputs of equal amplitude with a 90° phase shift. In transceiver mode operation, a low noise preamplifier with a circuit for protection from transmit RF was connected to the receive port of the quadrature hybrid to
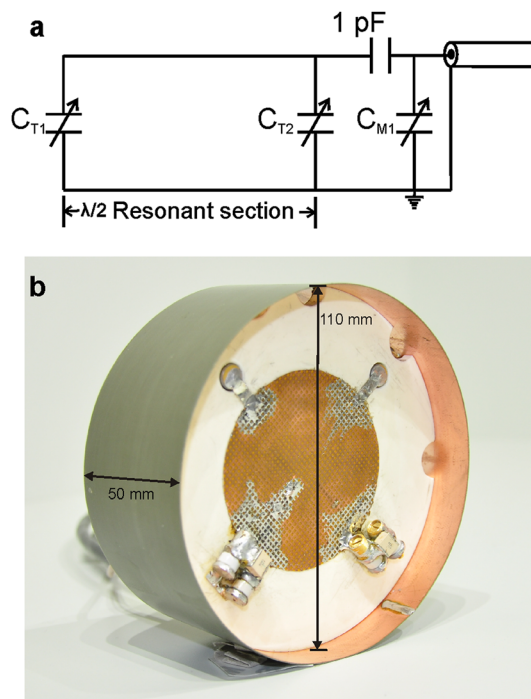

Figure 1. Capacitively tunable patch antenna. a) Equivalent circuit of one linear channel of the antenna. C_{T1} and C_{T2} are the tuning capacitors and C_{M1} is the matching capacitor. b) Picture of the tunable patch antenna with the radiating patch, outer shield and input circuit. The slots along the edges are provided to route the cables from the receive coil to the preamplifiers.

amplify the combined receive signal. The quadrature hybrid together with the TR switch and preamplifier were placed outside the service end of the magnet bore and two low loss cables (EZ_250_AL_TP, Huber + Suhner) of equal electrical length were used to connect the antenna drive ports to the hybrid.

FDTD simulations

FDTD simulations (XFDTD 6.5, Remcom, State College, PA, USA) were performed prior to the actual construction of the antenna to find suitable values for the antenna's physical dimensions, the permittivity of the substrate and the tuning capacitors. In addition, RF field behaviour was investigated for two different situations for comparison with experimental results: first, the patch antenna was modelled along with a tissue equivalent phantom ($\sigma = 0.9$ S/m, $\varepsilon_r = 56.5$, 40-mm diameter and 80-mm long) placed 2 cm in front of the antenna. In a second scenario, the phantom was replaced with a realistic rat model (Remcom) composed of 35 different tissue types with electrical properties valid at microwave frequencies. In both cases, the simulations included a detailed model of the patch antenna comprising the outer copper laminate, the RF shield, the four tuning capacitors as well as the two feed ports. Capacitors for impedance matching were not incorporated into the model. Perfectly matched layers (PML; 7 layers) were set as the boundary condition of the simulation domain. Broadband excitations were simulated to iteratively find the capacitances needed to shift the resonance frequency to 698 MHz and to decouple the two ports. As a result, all four capacitors were set to 3.13 pF in the case of the phantom and 3.06 pF for the rat mesh. Using a sinusoidal excitation of the two ports driven in quadrature, B_1^+ fields were recorded after the simulation converged to a steady state in which fields did not deviate by more than -30 dB from a pure harmonic variation. Results were scaled to a net input power of 1 Watt and exported to MATLAB (The MathWorks, Natick, MA, USA) for data analysis and presentation.

Receive coil construction

Three receive coil elements were assembled on a semi-cylindrical Teflon tube (2-mm wall thickness and 29-mm inner diameter) that snugly fit a rat head. Coil elements 1 and 3 were assembled on the two sides of the cylinder and element 2 was on the top as shown in Figure 2a. The coil elements were constructed using 2.5-mm wide silver strips. Each element had four capacitors in series and the input capacitor was further split to form the matching and active detuning circuit as shown in the schematic (Fig. 2b). To adjust the tune and match of the coil elements, a variable capacitor was provided in the coil input path. Using a pair of decoupled flux probes, the unloaded and loaded Q were measured for the single isolated loops without coaxial cables attached to the input. Unloaded Q for element 1, with the decoupling inductor, and element 2 were 178 and 202, respectively. The loaded Q, measured by loading the coil with a 26-mm diameter phantom filled with average brain tissue equivalent solution (15), was 59 and 62 for the respective loops.

Elements 1 and 3 were decoupled inductively (18) and -20 dB of isolation was achieved between the two elements. Geometrically overlapping element 2 with 1 and 3 resulted in an isolation of -15 dB (1). The decoupling inductor and the geometric overlap were optimized with the coil being loaded with the rat head phantom. The element layout adopted for the receive array
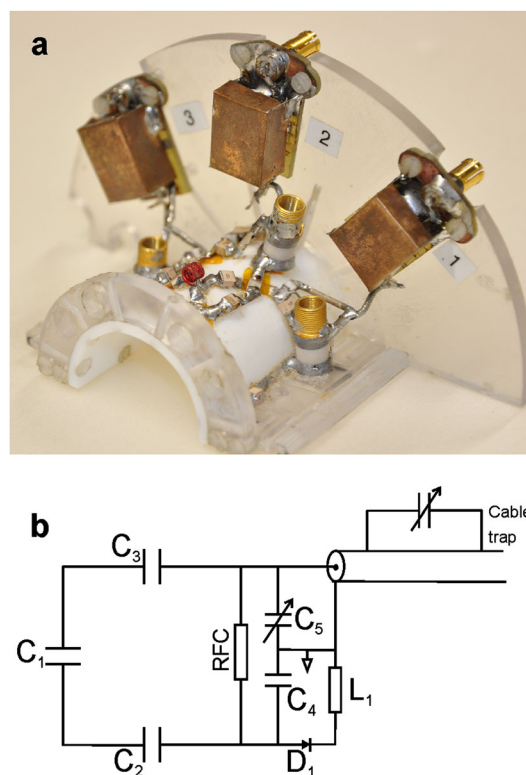

Figure 2. 3-Channel receive array. a) Picture of the receive coil array. The shielded cable trap is assembled on the vertical plate to minimize interferences with the transmit field. b) Equivalent circuit schematic of a single element of the receive coil. The bias current to detune the receive coil is fed to the diode D_1 through the RF choke (RFC). The input impedance of the coil is adjusted with the variable capacitor.

allowed for mutual decoupling of the three individual elements and hence additional decoupling strategies were not required. A shielded cable trap formed by winding a coaxial cable (Sucoform 47, Huber + Suhner) in the form of an inductor and tuned to 698 MHz by a capacitor between the turns of the coaxial cable ground shield was connected across the input matching capacitor. The cable traps were mounted above the level of the receive coil on a vertical acrylic sheet (Fig. 2a) to reduce the influence on the transmit field produced by the antenna. A PIN diode (MA4P7452F-1072T, MA-COM Technology Solutions Inc., Lowell, MA, USA) detuned the receive coil during transmit by creating high impedance across the coil input. The control signal available from the MR system to bias the PIN diode was inserted into the RF cable through a bias tee in the receiver board.

Receive system

A receiver setup that could support up to four receive channels was custom-built and mounted behind the antenna on the animal bed. The setup consisted of two stacked circuit boards, each with two plug-in preamplifiers and bias tee to insert DC into the RF cable. The 3-channel receive coil was connected to the receiver board using coaxial cables (K_02252_D-08, Huber + Suhner) routed through the slots provided in the transmit antenna. An additional cable trap was inserted between the interconnecting coaxial cable and the receive preamplifier. The fourth channel in the receiver board was not used for this receive array.

A two-stage low noise amplifier in cascode configuration consisting of a pHEMT (ATF-35143, Avago Technologies, San Jose, CA, USA) in common source (CS) mode followed by a BJT (BFR193, Infineon Technologies, Milpitas, CA, USA) in common base (CB) mode was designed. These preamplifiers were retuned versions of the two-stage 9.4 T preamplifier presented elsewhere (19) and had a noise figure of 0.65 dB with 27 dB gain at 698 MHz.

RESULTS

Tunable patch antenna in transceiver mode

Figures 3a and 3b show flip angle maps measured using the AFI method (20) through the middle of an average rat muscle tissue
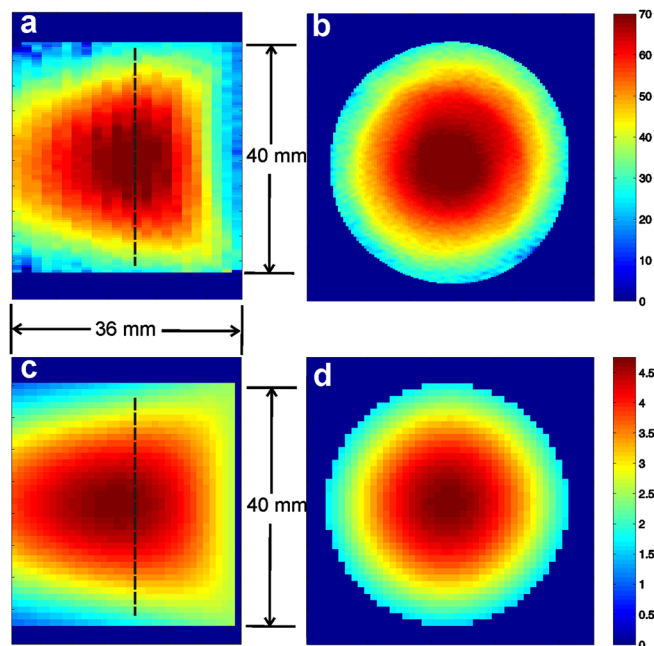

Figure 3. Validation of transmit performance. a) Measured flip angle map (degrees) in the coronal plane using a 40-mm diameter phantom. The transmit antenna was placed at a distance of 2 cm in front of the phantom. b) View of the transverse plane at the dotted line shown in Figure 3a. c, d) Simulated B_1^+ magnitude maps (μT) through approximately the same slice locations as shown in Figures 3a and 3b. The phantom model had similar dimensions and electrical properties as the phantom used in the measurements.

equivalent (15) phantom (40-mm diameter, 80-mm long) in the coronal and axial planes, respectively. The phantom was centered in the middle of the gradient system and 2 cm in front of the antenna, which was located to the right of the flask in the coronal view. The tunable patch antenna was driven in quadrature and operated in transceive mode. A maximum flip angle of 73° was obtained in the centre of the phantom using a 1-ms gauss pulse (2.69 kHz bandwidth). For comparison, the B_1^+ magnitude pattern in the same slice obtained from the FDTD simulation is displayed in Figures 3c and 3d. The simulation tool predicted that ∼80% of the net input power would be absorbed by the nearby phantom, whereas the rest would be radiated or dissipated. However, the percentage of absorbed power and hence the efficiency decreased with increasing distance between sample and antenna. The simulated B_1^+ pattern closely matched the measured flip angle map, which demonstrated that the antenna worked as expected and that the excitation field was well described by the results from the FDTD simulations. The B_1^+ field exhibited a region of constructive interference inside the phantom similar to that observed with conventional volume coils. Furthermore, the field tapered with increasing distance from the antenna but still penetrated several centimetres into the phantom. This demonstrates the strong influence of the load on transmit field propagation and thus motivates the utilization of this tunable patch antenna as a transmit coil for rodent head imaging.

To further characterize the transmit performance, the antenna was compared with a custom-built 8-element microstrip volume resonator (48-mm ID and 60-mm long) driven in quadrature. Figures 4a and 4b show axial views of the measured flip angle maps acquired using the tunable patch antenna and the microstrip volume resonator, respectively, for a 26-mm diameter phantom filled with average rat brain equivalent solution (15). RF power was calibrated to achieve a flip angle of approximately 70° in the centre of the phantom with a 1-ms Gauss pulse (2.69 kHz bandwidth) for both the setups. The tunable patch antenna required an additional 10 dB of RF power to achieve the same flip angle and was thus less efficient than the volume resonator, which is not surprising in view of its much larger excitation volume. For *in vivo* measurements, the anesthetized rat was placed on an animal holder, positioned 2 cm in front of the patch antenna, and centered in the middle of the gradient system. The impedance match on both orthogonal ports of the patch antenna was adjusted to better than -25 dB and the isolation
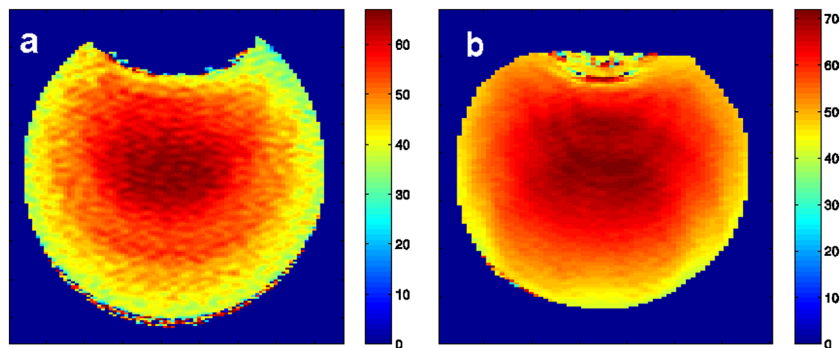

Figure 4. Comparison with volume resonator. a) Axial view of the flip angle map (degrees) on a 26-mm diameter phantom acquired with the tunable patch antenna. b) Flip angle map measured with a microstrip volume resonator tuned to the same phantom as used for Figure 4a. The RF power was calibrated to achieve a flip angle of 70 degrees in the centre of the slice.

between the two ports was better than -30 dB. Figure 5a shows an axial multislice gradient echo FLASH dataset acquired using the following parameters: TE = 2.5 ms, TR = 800 ms, FOV = 4 × 4 cm², slice thickness = 1 mm, matrix size = 256 × 256, flip angle: 40°, 1 ms Hermite pulse. Excellent image homogeneity free of B_1 artefacts was achieved not only across the brain but also over the whole rat head. The transmit antenna was able to reach a flip angle of 90° using a 500-μs block pulse with around one fourth of the available RF power.

At very high Larmor frequencies, it is common to use surface coils for both transmit and receive, and hence the use of spin-echo sequences for imaging larger volumes is constrained by the inhomogeneous B_1^+ field distribution. Due to the relatively homogeneous excitation field generated by the antenna, we were able to acquire spin-echo RARE images (Fig. 5b) over a 4-cm FOV along the z-axis covering the whole rat brain and even extending into the spinal cord.

To gain more insight into RF field behaviour, simulated B_1^+ fields are shown in Figure 6. A sagittal view through the setup, i.e. antenna, RF shield and rat mesh is depicted in Figure 6a along with the calculated B_1^+ field. Note that all tissues except for grey matter and skin are hidden to better visualize the field propagation inside the rat model. Obviously, there was no considerable field propagation effect along the narrow bore at this frequency, as apparent from the rapid decay of the transmit field outside the rat with increasing distance from the antenna (Fig. 6a). However, inside the rat body, the B_1^+ field penetrated much deeper towards the z-direction so that, in accordance with experimental results, a strong field could be created even beyond the rat brain. For example, the average B_1^+ magnitude in grey matter voxels across a single transverse slice dropped by only 30% from the most anterior to the most posterior part of the rat brain. The B_1^+ pattern in a single axial slice through the level of the brain centre is shown in Figure 6b. Similar to a quadrature excitation with a conventional volume coil, the field was strongest in the centre and dropped off smoothly towards the periphery to approximately 50% of the maximum value. This drop-off explains the increased image intensity in the centre of the rat head in Figure 5a. However, in the FLASH images, the effect was further amplified due to the characteristic receive sensitivity of the antenna, which was almost identical to the B_1^+ pattern in this case.

Receive only array

For image acquisition with high SNR, the antenna was combined with a 3-channel receive-only array. To validate the performance of the receive array, the SNR in the rat head phantom was compared with a quadrature transceiver surface coil built on a semi cylindrical acrylic tube with dimensions identical to the receive array former. The quadrature coil also had identical
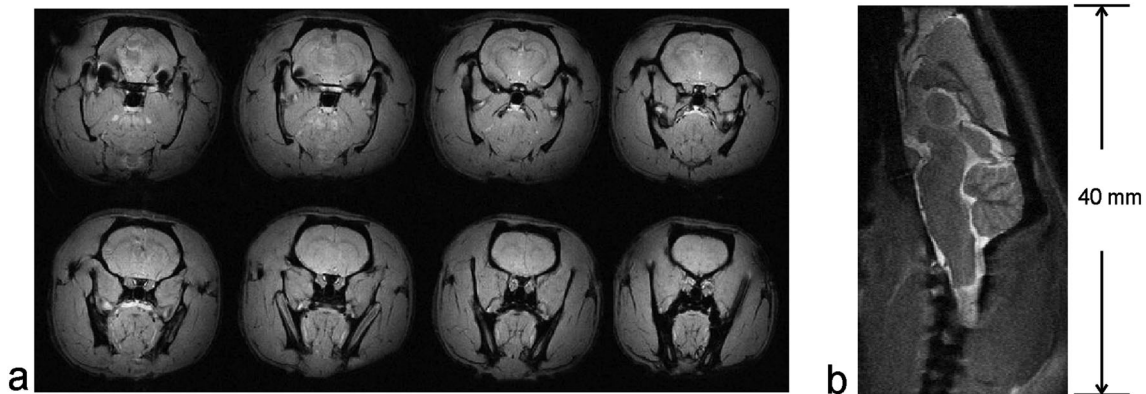

Figure 5. *In vivo* measurements using the tunable patch antenna. a) Axial FLASH images of the rat head with excellent image uniformity over the entire volume of interest. b) Sagittal spin-echo RARE images over the entire brain could be acquired due to the high excitation homogeneity achieved with this setup.
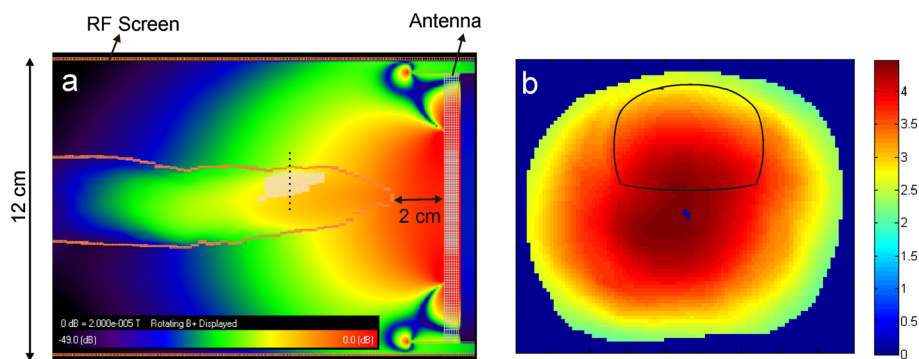

Figure 6. Simulated RF field behaviour in a rat model. a) Overview of the entire model. The gradient RF shield, the complete transmit antenna model, and a rat mesh along with the predicted B_1^+ field behaviour in dB scale are included. Note that all tissues except for grey matter and skin are hidden for better visualization of the B_1^+ field. The dotted line illustrates the location of the axial slice shown in Figure 6b. b) The B_1^+ pattern (μT) in a single axial slice through the middle of the brain. The black line illustrates the outline of the rat brain.

longitudinal coverage. For both setups, RF power was calibrated for a sample region, right below the middle element of the receive array, that is in an *in vivo* experiment occupied by the rat brain. Fully relaxed gradient echo images with identical imaging parameters (TE = 3.8 ms, TR = 15 s, FOV = 3 cm, slice thickness = 2 mm, excitation angle = 90°) were acquired in both configurations. In an ROI similar to the size and shape of the rat brain, the SNR of the 3-channel receive array was 37% better than the quadrature surface coil. SNR was calculated as the mean signal value from the chosen ROI divided by the standard deviation of the signals from voxels in an ROI placed in an artefact free background.

A 2-dimensional multislice gradient echo dataset of the *in vivo* rat brain obtained with the antenna in combination with the receive array is shown in Figure 7a. The coronal FLASH images were acquired with a flip angle of 40°, repetition time of 800 ms, echo time of 2.5 ms and in-plane resolution of 156 μm with 1-mm slice thickness. All four slices had the same window level and hence the top slice, which is closest to the coil, appeared brightest due to the higher sensitivity closer to the receive coil elements.

Figure 7b shows an axial multislice RARE dataset (TR = 1500 ms, TE = 8.26 ms, slice thickness = 1 mm, FOV = 4×4 cm^2, in-plane resolution = 156 μm). The 90° flip angle was achieved using a 3.3-ms Gaussian pulse with 8.6-dB attenuation at the output of the RF amplifier. As evident in these spin-echo images, the flip angles were close to the selected values for regions covering the whole rat brain due to the homogeneous transmit B_1 field achieved with our simple transmit antenna setup.

DISCUSSION

In this article, we presented the first application of a modified patch antenna in combination with a receive coil array for small animal imaging. Though the motivation for this work was originally from the traveling wave approach (11), which has the potential to more uniformly excite large volumes of interest at ultra-high field, the higher cut-off frequency of the narrow waveguide meant that wave propagation was not supported in our 16.4T MRI scanner. Hence, the subject was placed in the near-field of the patch antenna by moving the antenna towards the isocenter of the magnet.

Due to the increased attenuation along the z-axis, the B_1^+ field magnitude was expected to drop towards the caudal part of the rat, which was also evident in the simulation results shown in Figure 6a. However, aided by the propagation in tissue (Fig. 6a), the field homogeneity and transmit efficiency were sufficient to achieve 180° excitation across the few centimetres covering the entire rat brain in z-direction as it would have been possible with a close fitting volume resonator. Except for the increased roll-off of the B_1^+ field away from the antenna, the B_1^+ field in the axial view (Fig. 3, Fig. 4) looked similar to the circularly polarized quadrature transmit field produced by a birdcage coil.

Conventional volume coils for such high field strengths are, due to the narrow bore size, closely coupled to the load and hence the size and positioning of the load greatly influences the coil parameters like tune and match. Readjusting these parameters for different loading conditions disturbs the electrical symmetry and thereby the field homogeneity inside the resonator. For the presented setup, only slight changes in tune and match were necessary for different loads. Though less efficient compared to a volume resonator, the advantages of the tunable patch antenna lies in the design simplicity, the ability to excite larger sample volumes and the reduced sensitivity to changes in load. Hence, we find this transmit antenna a valuable alternative to the conventional volume resonators for spin excitation especially at very high Larmor frequencies.

The placement of the transmit antenna anterior to the rat frees up valuable space around the subject, which can be used for additional hardware for receive, stimulation, anaesthesia or other experimental requirements. The transmit antenna was easily combined with a conventional receive array for increased reception sensitivity, which could be invested in parallel imaging applications (14). Enhancements in transmit performance can be achieved by further optimizing the antenna design. For example, losses could be minimized by using air as a dielectric between radiating patch and ground. In addition, the transmit efficiency might be improved by varying the size of the patch, which could easily be done and would only require adjustments in the values of the terminating capacitors. Further improvements in receive performance are possible by increasing the number of receive elements.

While the performance of this coil combination was compared to a microstrip resonator as well as a quadrature surface coil,
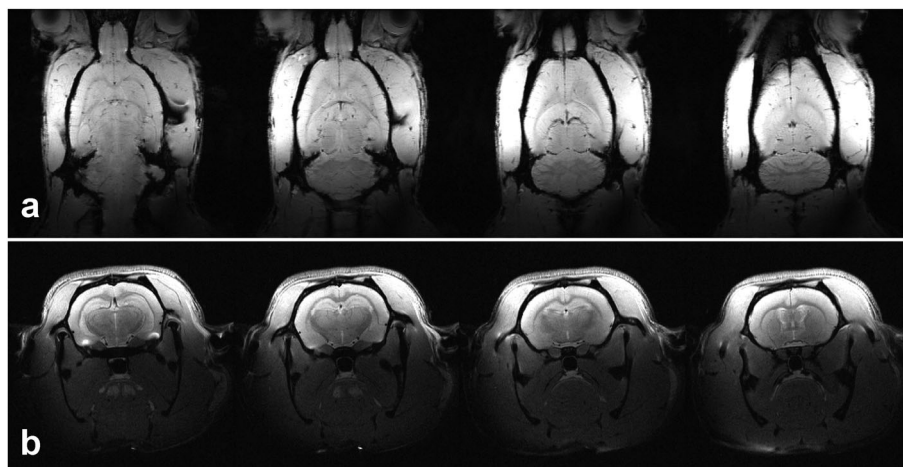

Figure 7. Receive array in combination with the tunable patch antenna *in vivo*. a) Multislice coronal gradient echo FLASH images covering the rat brain. Images were acquired with a slice thickness of 1 mm, TE = 2.5 ms, TR = 800 ms, FOV = 4×4 cm^2, matrix = 256×256. b) Multislice axial spin-echo RARE images acquired with the following parameters: FOV = 4×4 cm^2, TE = 8.26 ms, TR = 1500 ms, slice thickness = 1 mm, matrix = 256×256.

other possible RF coil options are multiport excitation and multi-element transceiver arrays. We believe that the setup presented is much simpler and more robust because of the additional hardware needs and cabling complexities associated with multi-element transceiver arrays in narrow bore ultra high field scanners.

Acknowledgements

REFERENCES

1. Roemer PB, Edelstein WA, Hayes CE, Souza SP, Mueller OM. The NMR Phased Array. Magn. Reson. Med. 1990; 16: 192–225.
2. Wiggins GC, Triantafyllou C, Potthast A, Reykowski A, Nittka M, Wald LL. 32-Channel 3 Tesla Receive-Only Phased-Array Head Coil With Soccer-Ball Geometry. Magn. Reson. Med. 2006; 56: 216–223.
3. Sodickson DK, Manning WJ. Simultaneous acquisition of spatial harmonics (SMASH): Fast imaging with radiofrequency coil arrays. Magn. Reson. Med. 1997; 38: 591–603.
4. Pruessmann KP, Weiger M, Scheidegger MB, Boesiger P. SENSE: Sensitivity encoding for fast MRI. Magn. Reson. Med. 1999; 42: 952–962.
5. Griswold MA, Jakob PM, Heidemann RM, Nittka M, Jellus V, Wang J, Kiefer B, Haase A. Generalized autocalibrating partially parallel acquisitions (GRAPPA). Magn. Reson. Med. 2002; 47: 1202–1210.
6. Hayes CE, Edelstein WA, Schenck JF, Mueller OM, Eash M. An efficient, highly homogeneous radiofrequency coil for whole-body NMR imaging at 1.5 T. J. Magn. Reson. 1985; 63: 622–628.
7. Behr VC, Weber T, Neuberger T, Vroemen M, Weidner N, Bogdahn U, Hasse A, Jakob PM, Faber C. High-resolution MR imaging of the rat spinal cord in vivo in a wide-bore magnet at 17.6 Tesla. MAGMA 2004; 17: 353–358.
8. Gareis D, Neuberger T, Behr VC, Jakob PM, Faber C, Griswold MA. Transmit-Receive Coil-Arrays at 17.6 T, Configurations for ^{1}H, ^{23}Na and ^{31}P MRI. Concepts Magn. Reson. Part B (Magn. Reson. Engineering) 2006; 29B: 20–27.
9. Hoffmann J, Shajan G, Pohmann R. Human Brain Imaging at 9.4 Tesla using a combination of Traveling Wave Excitation with a 15-channel Receive-Only Array. In *Proceedings of the 19th Annual Meeting of ISMRM*, Montreal, Canada, 2011; 164.
10. Wiggins G, Zhang B, Duan Q, Sodickson DK. Traveling Wave Imaging of the Human Head at 7 Tesla: Assessment of SNR, Homogeneity and B_1^+ Efficiency. In *Proceedings of the 17th Annual meeting of ISMRM*, Honolulu, Hawaii, USA, 2009; 2942.
11. Brunner DO, De Zanche N, Froehlich J, Paska J, Pruessmann KP. Traveling wave nuclear magnetic resonance. Nature 2009; 457: 994–998.
12. Glover P, Bowtell R. MRI rides the wave. Nature 2009; 457: 971–972.
13. Hoffmann J, Shajan G, Pohmann R. Capacitively tunable patch antenna for human head imaging at 9.4 T. In *Proceedings of the 18th Annual Meeting of ISMRM*, Stockholm, Sweden, 2010; 3802.
14. Shajan G, Hoffmann J, Balla DZ, Pohmann R. A 700 MHz Receive Array using Patch Antenna for Spin Excitation. In *Proceedings of the 18th Annual Meeting of ISMRM*, Stockholm, Sweden, 2010; 3803.
15. Beck BL, Jenkins KA, Rocca JR, Fitzsimmons JR. Tissue-Equivalent Phantoms for High Frequencies. Concepts Magn. Reson. Part B 2004; 20B: 30–33.
16. Zhang B, Wiggins G, Duan Q, Sodickson DK. Design of a patch antenna for creating traveling waves at 7 T. In *Proceedings of the 17th Annual Meeting of ISMRM*, Honolulu, Hawaii, USA, 2009; 4746.
17. Lee RF, Hardy CJ, Sodickson DK, Bottomley PA. Lumped-Element Planar Strip Array (LPSA) for Parallel MRI. Magn. Reson. Med. 2004; 51: 172–183.
18. Kokubunji TN, Soka TT, Kashiwa YM, Akishima EY, Katakura K. RF Probe for MRI. US patent 5,489,847, 1994.
19. Shajan G, Hoffmann J, Budde J, Adriany G, Ugurbil K, Pohmann R. Design and Evaluation of an RF Front-End for 9.4 T human MRI. Magn. Reson. Med. 2011; 66: 596–604.
20. Yarnykh VL. Actual Flip-Angle Imaging in the Pulsed Steady State: A Method for Rapid Three-Dimensional Mapping of the Transmitted Radiofrequency Field. Magn. Reson. Med. 2007; 57: 192–200.

Chapter 3

Discussion

This thesis focused on the design of RF coil arrays and RF hardware for 9.4T whole body human and 16.4T animal MRI scanners. A variety of application specific coils in different configurations were built to meet the requirements of the different projects. In this chapter, the different types of coils presented in this work are discussed in the context of the evolution of coil designs specific to UHF and the work published by other research groups.

3.1 Progress of RF coil design in UHF

Considering the initial concerns on RF power requirements, dielectric resonances, RF penetration and suitability of coil designs routinely used for clinical MR frequencies, RF coil technology has made remarkable progress in addressing RF related challenges in MRI at UHF. Due to advancements in RF design and image acquisition strategies, images with significantly superior SNR and contrast are routinely being acquired at 7T and even at 9.4T compared to the early 4T head and body images which exhibited strong intensity variations across slices (Barfuss et al. 1990; Bomsdorf et al. 1988). The first 4T images were acquired with birdcage resonators (Hayes et al., 1985) which turned out to be suboptimal at field strengths where the sample dimensions approached the wavelength. TEM resonators, first proposed by Roeschmann (Roeschmann 1988) were considered an alternative option for high frequency applications because of the transmission line based distributed circuit approach and the shielded cavity. The TEM resonator was further advanced by Vaughan (Vaughan et al., 1994) and the design was successfully implemented for head imaging at 4T and later also at 7T (Vaughan et al., 2001). Furthermore, 4T body images of good quality and contrast were demonstrated by driving a TEM resonator through a 4-port quadrature splitter (Vaughan et al., 2004).

The experimental findings suggested that, despite the technical challenges, the expected increase in SNR and spectral resolution due to the high field could ultimately be realized. The central brightening effect as originally attributed to dielectric resonance

(Barfuss et al. 1990) is a fundamental phenomenon dependent on sample dimensions and wavelength in tissue. Several studies showed later on that the dielectric resonance effect is sufficiently dampened due to the conductivity and heterogeneity of the human tissue (Collins et al., 2005; Yang et al., 2002). A UHF volume resonator with a uniform B_1 field profile when empty will produce non-uniform distribution of B_1 when loaded with a human head. The B_1^+ field adds constructively in the center, being equidistant from each coil element and leads to partial cancellation outside of the center. An analogous interference can be expected in the receive mode when using a volume coil in transceive mode, leading to an inhomogeneous intensity distribution across the image (Van De Moortele et al. 2005). If the volume coil is broken up in a way that the signal from each coil element is collected on separate receive channels and combined as in a receive array (Roemer at al., 1990), the SNR loss in the periphery can be restored leading to a flatter looking image (Adriany et al., 2005). In addition, these types of coils make it possible to further homogenize or shape the RF field using static and dynamic RF shimming applications because the coils allow control over the amplitude and phase of the current to each coil element. Thus, coil designs for UHF applications migrated from the routinely used volume resonator excitation coils in clinical scanners to transceiver array designs with multi-port excitation and array reception.

3.2   Microstrip arrays

Microstrip transmission line (MTL) elements consist of a thin conducting strip and a ground plane separated by a low loss dielectric. Typically they resonate at a wavelength of λ/4 or at integral multiples of λ/4. The physical length of the resonant elements depends on the frequency and the relative permittivity (ε_r) of the dielectric substrate because the RF wavelength scales by $\sqrt{\varepsilon_r}$. Planar strip arrays (PSA) with microstrip elements as fundamental building blocks were proposed as an alternative to conventional loop arrays because of the intrinsic decoupling offered by the quarter wave transmission lines (Lee et al., 2001). Since the electric field is concentrated within the substrate, the loss associated with the electric field is minimized. Though the original design was validated at 1.5T, the design was well suited for high field applications, as also suggested in the original article, because of the distributed nature of the MTL

element. The individual elements can be easily tuned to different frequencies by adjusting the element length, substrate type and dielectric thickness. An improved and more practical version of the PSA is the lumped planar strip array (LPSA) where the physical length of the microstrip element is fixed and the electrical length is altered by terminating the ends of the microstrip with capacitors (Lee et al., 2004). Now the resonance frequency of the λ/2 resonators can be adjusted by tuning the capacitors across the strip and the ground plane.

Meanwhile, MTL based coil arrays were increasingly applied for 7T applications (Zhang et al., 2001). Coil arrays with microstrip loops and straight MTL segments were presented and the utility of MTL arrays for RF shimming applications was demonstrated (Adriany et al., 2005). Conventional MTL resonators and inverted MTL resonators were constructed and the performance was compared to birdcage and TEM resonators at 4T and 7T (Zhang et al., 2003; Zhang et al., 2005). MTL based designs also found applications in body imaging at 7T (Metzger et al. 2008). More 7T MTL designs in several different flavors and features were presented: geometrically adjustable arrays to improve the transmit efficiency (Adriany et al., 2008), center-fed microstrip elements to extend the longitudinal coverage and reduce the cabling issues (Brunner et al. 2007) and meander elements to improve the intrinsic decoupling are some of them (Orzada et al. 2009).

In the first publication on human MRI at 9.4T, both eight and 16 channel microstrip arrays were discussed. The eight element version did not use decoupling circuits because the physical separation between the adjacent coil elements and the large sample loading at 400 MHz was sufficient to dampen the coupling. Static RF shimming capability was also demonstrated with the 8-channel array (Vaughan et al., 2006).

The third 9.4T human MR scanner was installed at the MPI, Tuebingen and the RF coil program started in fall of 2007 with the aim to develop customized RF solutions for the 9.4T human scanner and the 16.4T animal scanner. The uniqueness of the scanner frequencies meant that it was almost impossible to find vendors to supply robust solutions for critical components like preamplifiers and TR switches. RF hardware, being the front-end, has a significant bearing on the quality of the acquired image.

Preamplifiers with electrical and mechanical specifications matching the industry standards at 3T were developed. In addition, TR switches with low loss and enhanced protection from high-power transmit RF were custom built (Shajan et al., 2011). MTL arrays being the design of choice at that time for applications above 3T, a 16-channel elliptic transceiver array was developed (Shajan et al., 2011, see section 2.1). Coupling between adjacent coil elements was cancelled using decoupling capacitors. The high sample loading at 400 MHz dampened the coupling to the next-neighboring elements. The custom-built setup provided excellent and robust RF performance as evident from the high quality susceptibility weighted images acquired with this setup (Budde et al., 2011).

3.3 Dual row arrays

Conventional circularly polarized (CP) mode excitation of a volume transmit array for human brain imaging at UHF produces a central brightening effect and signal cancellation at approximately a quarter wavelength away from the center of the coil. While this can be visualized on a field map plotted in the transversal plane, there is also significant cancellation along the sagittal/coronal plane, especially in the lower brain. A field map acquired with the microstrip coil (Shajan et al., 2011) in CP mode is shown in figure 1. Even though the microstrip elements are 14 cm long, significant excitation of the whole brain is severely limited due to the field drop outs. Furthermore, static and dynamic RF shimming techniques are less effective in extending the longitudinal coverage with single row coil arrays. Such arrays do not provide sufficient degrees of freedom to orient the B_1^+ field along the Z-direction. These limitations were addressed with the idea to distribute the single transmit coil elements not only over the radius of the coil, but also along the z-direction, forming coils with two or more rows of coil elements.

Unique coil layouts with 3D RF shimming capability were proposed to improve image homogeneity and achieve whole brain coverage at very high frequencies and field strengths (Adriany et al., 2007; Avdievich et al., 2011; Gilbert et al., 2012, 2011). Later on, numerical models of dual and multi-row coil arrays were comprehensively analyzed

to establish the suitability of dual-row coil arrangements for UHF applications (Kozlov et al., 2011a, 2011b). The dual-row microstrip array (Adriany et al., 2007) and the loop based multi-row arrays (Avdievich et al., 2011; Gilbert et al., 2012, 2011) were transceiver arrays and did not optimize the receive performance.
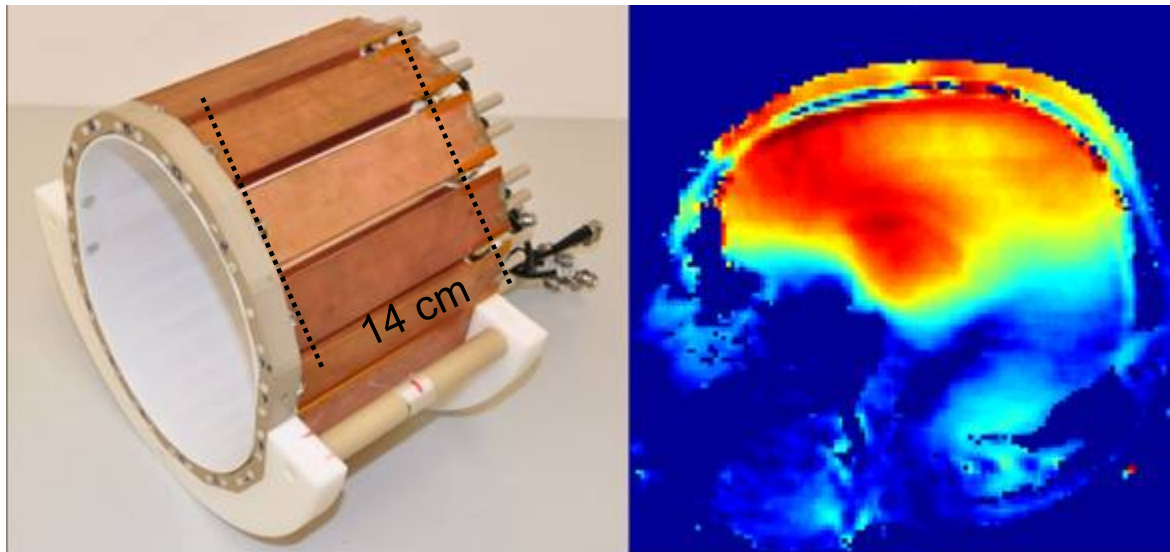

Figure 1: Left: Field map of the 16-element microstrip array in CP mode. Right: Significant field drop out in the lower brain are apparent in the sagittal plane.

State of the art MR systems are delivered with 32 receive channels and multi-channel receive arrays constructed on form-shaped coil housing maximize receive performance (Keil et al., 2013; Wiggins et al., 2006). To take advantage of the higher intrinsic SNR available at UHF (Keltner et al. 1991), the receive performance must be optimized. Hence, an optimum RF setup for UHF brain imaging must combine a dual-row parallel transmit technique with parallel receive technology. A 16-element transmit array in combination with a 31-element receive array for UHF brain imaging was first demonstrated by this author (Shajan et al., 2014; Shajan et al., 2012, see section 2.2). The coil combination achieved significant gain in SNR compared to a 16-element microstrip transceiver array. A subsequent study comparing coil performance and MR parameters across different field strengths demonstrated a deterioration of the B_1 homogeneity and transmit efficiency at 9.4T (Pohmann et al., 2015). However, the SNR gain was distinctly supra-linear. Though the findings in that study were as predicted by

numerical analysis, it is important to note that this ambitious coil setup met its objective. Also important is the fact that the original design was meant for a head gradient insert and hence the construction of the complicated coil structure was hindered by significant space constraints.

The construction of both microstrip based and loop based multi-row coil arrays is challenging because of the coupling between the elements of the different rows and through the cable that feeds the lower row elements. If one row is rotated with respect to the other row, each element of the upper row can be decoupled with two elements of the lower row. Row rotation also reduces the coupling between the diagonal elements of adjacent rows because it increases the physical separation. Routing of the feed cables to lower row elements is the most significant design consideration. Not the shortest path to the lower row, instead, routing the cables through the virtual ground of the upper row elements provides the best results. Similarly, the cables in the receive helmet must be carefully routed so that the transmit coil remains unaffected. The influence of the receive array on the transmit coil is visualized by acquiring field maps with and without the receive array physically present in the FOV. Combining transmit and receive arrays takes advantage of both parallel transmit and parallel receive methods enabling B_1^+ correction as well as providing high SNR. Not just for 9.4T, this coil arrangement is beneficial for ^{1}H imaging in all UHF scanners (≥ 7T).

3.4 Methods development and applications

Not only application specific customized RF hardware is important for MRI at 9.4T, it must also be accompanied by strategies for RF field management and by techniques and methods optimized for imaging at this field strength. This section gives a short overview over some of the studies that focus on these aspects, using the hardware presented in the previous chapters.

3.4.1 RF field management

MR imaging at 9.4T enters a regime where the high Larmor frequency leads to complex behavior of the RF field in biological tissue. This issue is significantly more severe at 9.4T than at 7T and transmit arrays with elements in multiple rows are needed to

distribute the B_1^+ in the cerebrum, cerebellum and brainstem (Adriany et al., 2007). RF field management plays a significant role in the utilization of three-dimensional transmit arrays. Static RF shimming or dynamic parallel transmission approaches are used to manage the B_1^+ field in the desired target areas with respect to homogeneity, power efficiency or SAR (Hoffmann et al., 2013b).

Due to the increase in energy deposition with frequency, transmit array designs are accompanied with numerical simulations in order to assess local SAR as a function of forward power and RF shim setting. Moreover, the power limits to comply with local and global SAR limits for in vivo scans are set based on simulation results. An excellent match between simulation and measurement was achieved (Hoffmann et al., 2013b), which was essential to ensure patient safety.

The static RF shimming capabilities of the dual-row RF coil setup were analyzed numerically and validated experimentally with regard to the possibility to achieve whole brain void-free excitation even at a field strength as high as 9.4T.
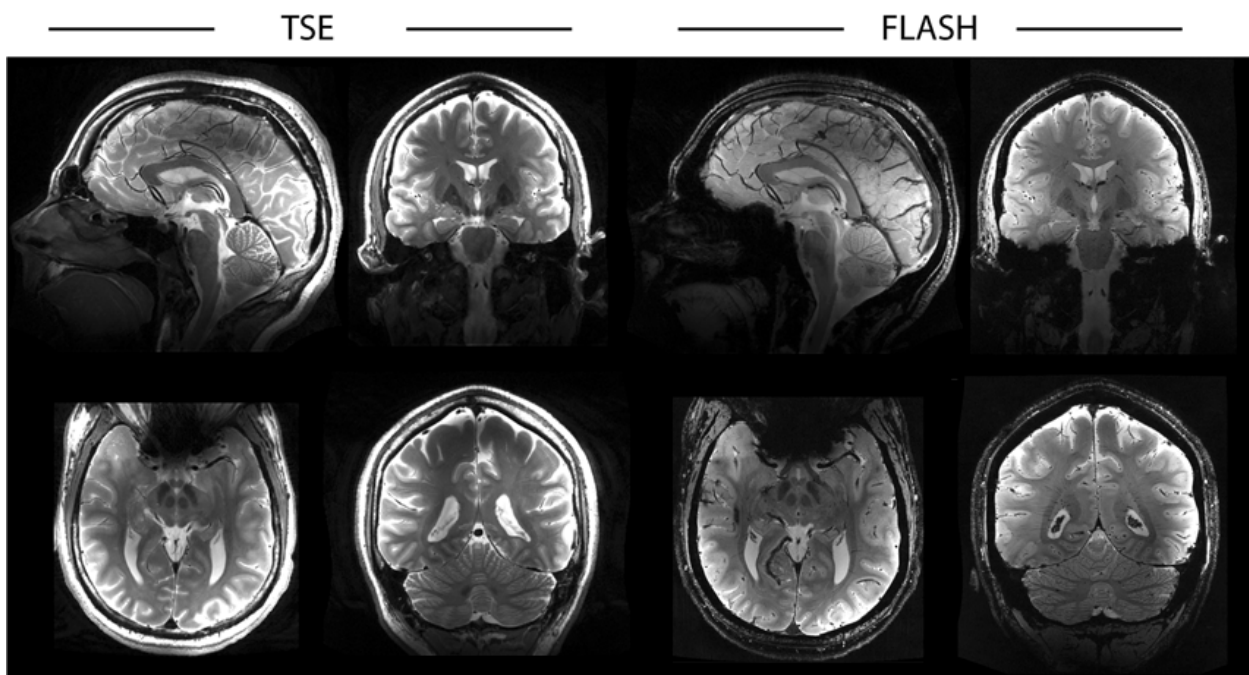

Figure 2. Slice-by-slice phase-only shimmed TSE and FLASH images acquired from different subjects at 9.4T using the 16-channel transmit and 31-channel receive array setup (Shajan et al., 2014). Reprinted with permission from (Hoffmann et al., 2013b).

3.4.2 Travelling wave imaging with high SNR

The traveling wave approach has the possibility to excite a large volume of interest at high Larmor frequencies (Brunner et al., 2009). However, one of its limitations is its poor receive sensitivity due to the large distance to the sample. Combining a tight fitting receive array with traveling wave excitation provides extended longitudinal coverage as well as a significantly higher SNR (Hoffmann et al., 2013a). Furthermore, this approach leaves free space around the head, which improves patient comfort as well placement of additional hardware.
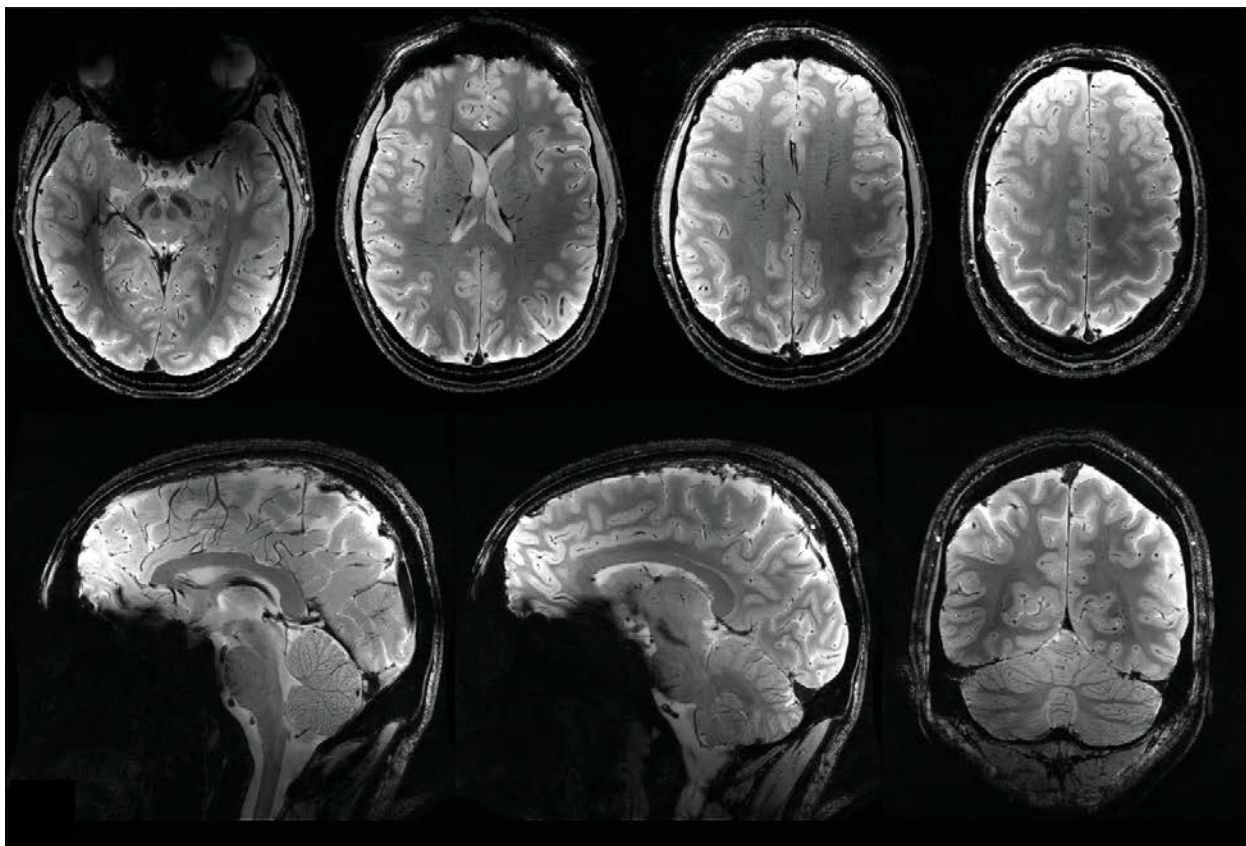
Figure 3. Two-dimensional FLASH images illustrate coverage, signal intensity distribution and image contrast. TR/TE = 400/10 ms, two averages, bandwidth = 80 Hz/pixel, flip angle = 25° in center of brain. Sagittal images: FOV = 215 x 215 mm^2, slice thickness (THK) = 1.5 mm. Coronal image: FOV = 177 x 210 mm^2, THK = 1.5 mm. Axial image: FOV = 166 x 205 mm^2, THK = 1 mm. Reprinted with permission from (Hoffmann et al., 2013a).

3.4.3 Contrast mechanisms

The sensitivity to susceptibility variations is known to increase with field strength. However, this also opens up new possibilities for improving image contrast. Potential benefits of 9.4T for T_2*, phase and susceptibility weighted contrast mechanisms were investigated (Budde et al. 2011). Imaging was performed using the 16-channel microstrip array setup (Shajan et al., 2011). White matter structures not visible in conventional images were identifiable in the T2* images. Phase images with excellent grey and white matter contrast with an in-plane resolution of 130μm was acquired. Due to the high sensitivity to susceptibility differences at 9.4T, susceptibility weighted imaging (SWI) was able to depict venous structures with high level of detail. In comparison to 3T, performance enhancement at 9.4T in terms of improved contrast as well as supra-linear SNR gain was achieved (Budde et al. 2011).
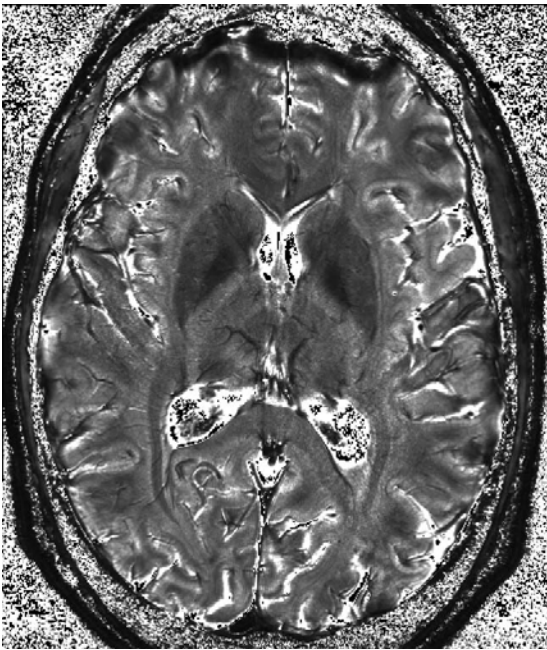

Figure 4. One slice of a T_2* map with an in-place resolution of 0.35 mm and slice thickness of 2 mm. Reprinted with permission from (Budde et al. 2011)
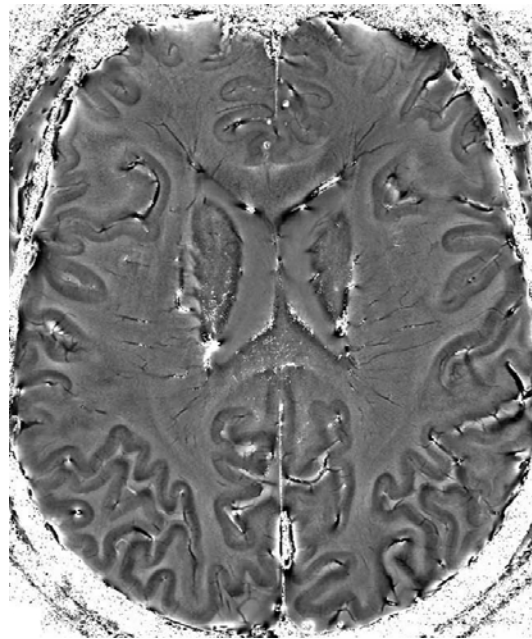
Figure 5. Filtered phase image computed with combined complex and phase filtering, displaying excellent contrast   between gray and white matter throughout the entire image, with an in-plane resolution of 200 μm. Reprinted with permission from (Budde et al. 2011)
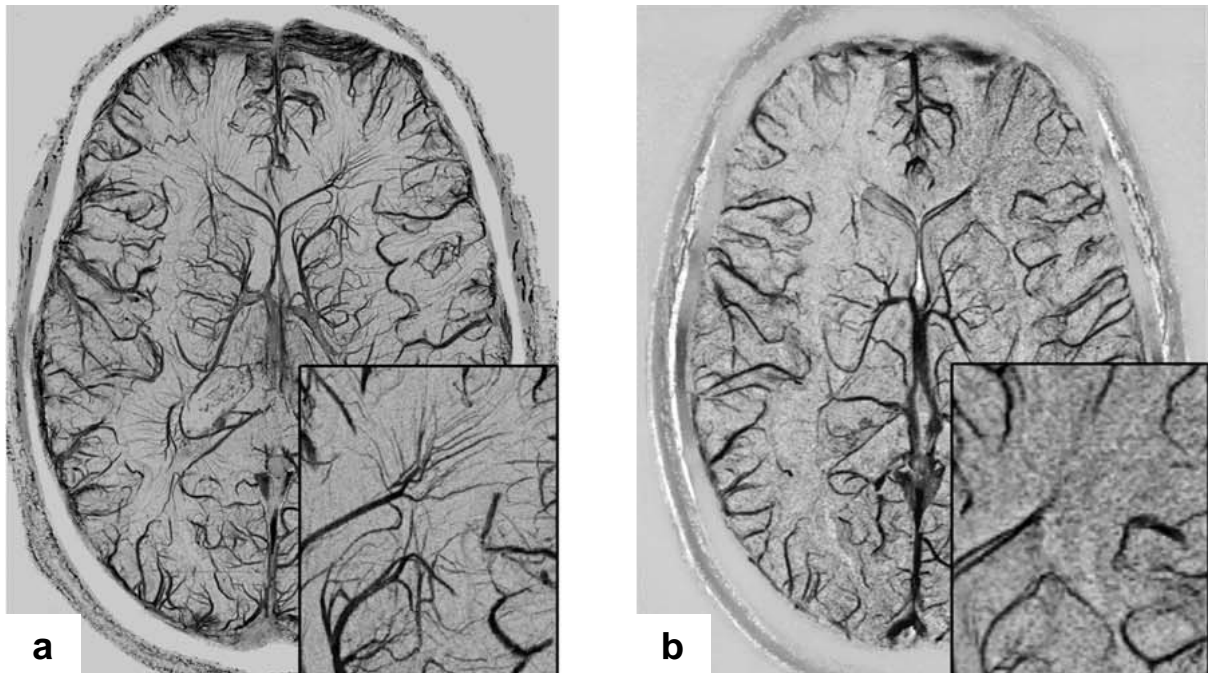
Figure 6. Minimum intensity projections of susceptibility weighted images. (a) is acquired at 9.4T with an in-plane resolution of 175 μm and (b) is from 3T with the same resolution. The 9.4T images field show much more details than the 3T images. Reprinted with permission from (Budde et al. 2011)

3.4.4 Functional MRI at 9.4T

The increased SNR and higher blood oxygen level dependent (BOLD) signal at ultra-high field boosts the possible resolution in functional MRI (fMRI) studies. The specificity of human functional MRI were investigated at 9.4T using both gradient-echo (GRE) and spin-echo (SE) based echo-planar imaging (EPI) (Budde et al., 2014a). First fMRI data from human subjects at 9.4T were analyzed to estimate the potential gain that can be achieved by increasing the field strength and to demonstrate the feasibility of human functional MRI at 9.4T with high spatial specificity (Budde et al., 2014a).
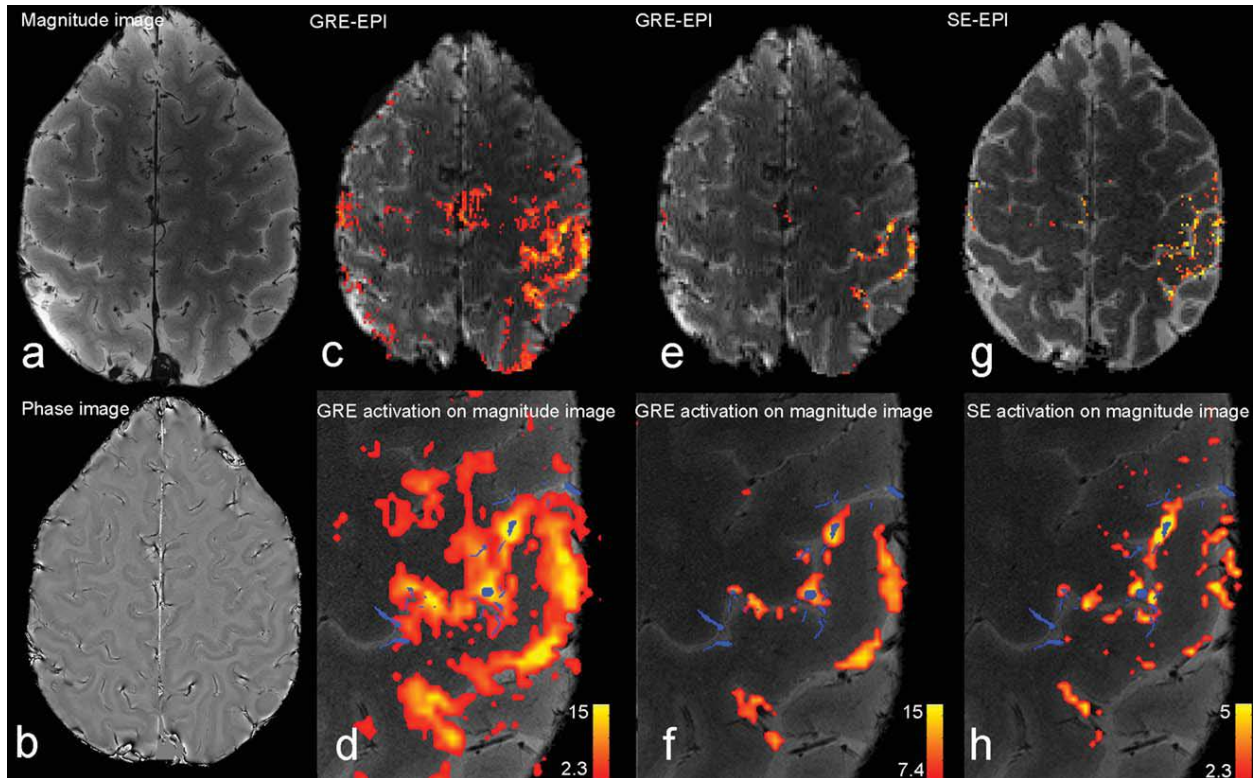
Figure 7. Anatomical and functional images from one volunteer. Anatomical images are shown in magnitude (a) and phase (b) representation. SE-EPI (g) and GRE-EPI (c, e) images were acquired with a resolution of 1.0 mm^3 and show clear activations of the motor and somatosensory cortex. In (c), all activated voxels are displayed, whereas in (e) the z-statistical threshold is set to yield equal numbers of activated voxels for SE-EPI and GRE-EPI. Zoomed images of the activation, registered to the high-resolution anatomical data, are shown in (d), (f), and (h). The locations of the veins are overlaid in blue. The color bar shows the z-score and scaling is equal in whole brain and zoomed images. Reprinted with permission from (Budde, et al., 2014a).

3.4.5 Acquisition weighted imaging at 9.4T

The principal reason behind increasing the strength of the static magnetic field is the promise of increase in SNR, which could then be invested in boosting the spatial resolution of in-vivo images. To realize the full potential of ultra-high field MRI, imaging techniques that are optimized to obtain highest possible SNR must be applied along with RF instrumentation designed to maximize receive sensitivity. These techniques could then be used for neuroscientific applications like noninvasive identification of

small anatomical structures in cortex or deep brain structures (Logothetis et al., 2002), or in medical applications where small-scale pathologies are examined as in the case of multiple sclerosis (Hammond et al. 2008). Ultra-high resolution human brain images with voxel volume of $0.014mm^3$ were acquired using the SNR optimized 31-channel receive array (Shajan et al., 2014) in combination with acquisition weighting technique which provided further 20% increase in image SNR (Budde et al., 2014b).
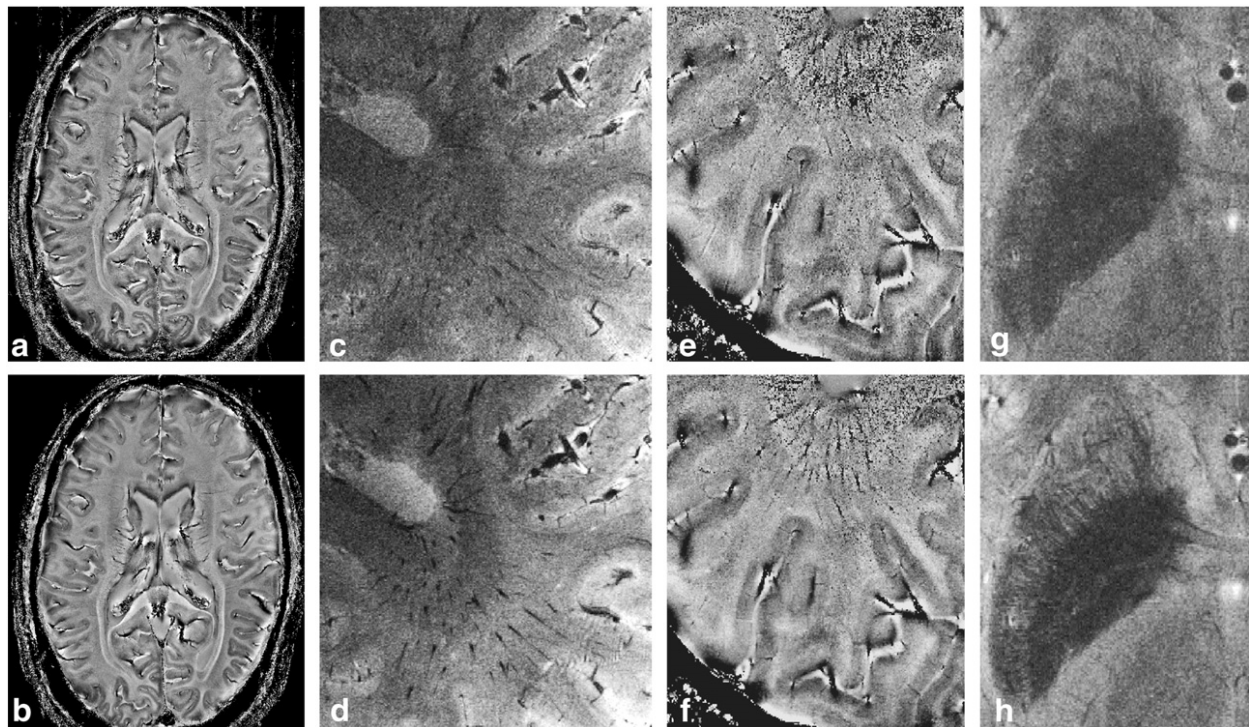

Figure 8. Comparison of in vivo high resolution (0.2 mm in plane) images acquired with conventional (top row) and acquisition-weighted (bottom row) imaging. a–b:Whole brain phase images, acquired with a slice thickness of 1 mm. c,d: Magnitude images (slice thickness 0.5 mm), demonstrating the improved visibility of small veins due to improved SNR with the weighted sequence. e,f: Phase images, showing a distinct SNR increase, especially visible in the interior whitematter. g,h:Magnitude image of the putamen (averaged over three slices). The acquisition-weighted images show a clearly improved representation of the fine structure. Reprinted with permission from (Budde, et al., 2014b).

3.4.6 Arterial spin labeling at 9.4T

The higher intrinsic SNR together with the longer longitudinal relaxation times at UHF can potentially benefit arterial spin labeling (ASL) at this field strength. To this end, the feasibility of multi-slice pulsed arterial spin labeling (PASL) of the human brain at 9.4 T was investigated (Bause et al. 2015). Quantitative, functional and high-resolution (1.05 x 1.05 x 2mm^3) ASL experiments were performed to demonstrate the potential of arterial spin labeling at 9.4T. In comparison to 3T, 23% lower perfusion in gray matter and 17% lower perfusion in white matter was observed at 9.4T. Functional and quantitative perfusion-weighted images showing a high degree of detail were obtained using the dual-row transmit 31-channel receive array (Shajan et al., 2014), even with the limitation of field inhomogeneity and SAR that are typical to UHF (Bause et al. 2015).
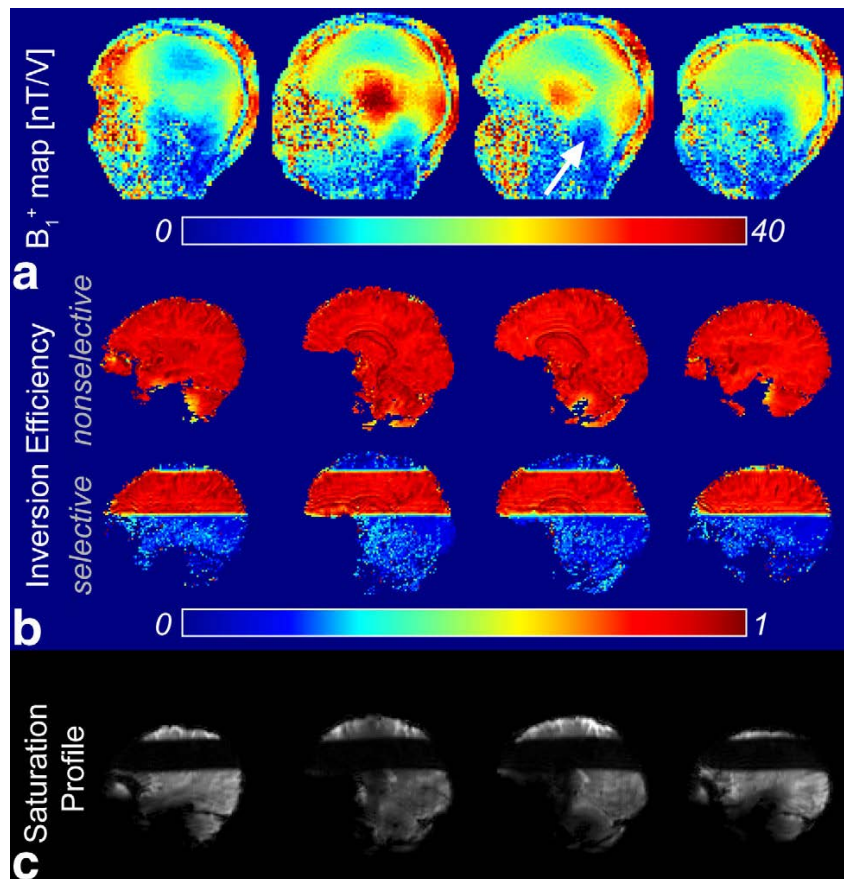

Figure 9. a: Measured transmit field (four sagittal slices of the 3D volume are shown) at 9.4 T. The white arrow indicates the area with very low transmit field strength in the cerebellum. b:

Fitted efficiency of the selective and nonselective inversion in the brain. c: Measured slab profile of the WET saturation with optimized flip angles. Reprinted with permission from (Bause et al. 2015).

3.5   Sodium imaging at 9.4T

In addition to protons, several other nuclei in the human brain are visible for MR and play an important part in physiological processes. Sodium, as one of the key nuclei in cell physiology, is of special interest for neuroscientific and medical applications. However, its concentration and NMR sensitivity are low compared to those of protons. Hence it is essential to maximize the coil performance at the sodium frequency. In addition, ^{1}H imaging capability is a desirable feature as part of a sodium coil for B_0 shimming to maximize the homogeneity of the static magnetic field. Furthermore, the gyromagnetic ratio ϒ of sodium is 3.8 times lower than that of ^{1}H resulting in a much lower Larmor frequency for sodium. Since coil loading is a function of frequency and size of the coil, increasing the number of coil elements in the array is not always beneficial. These considerations complicate the design and implementation of RF coils meant for sodium imaging. A dual-frequency RF coil setup consists of more than one coil. The low frequency coil is always placed close to the sample to maximize sensitivity. However, the low frequency coil has low impedance at the ^{1}H frequency and acts as a shield to the external coil. Nevertheless, the principal design aim is to maximize the coil performance at the sodium frequency and have sufficient ^{1}H signal for B_0 shimming.

Several dual-tuned or dual frequency setups have been proposed for multi-nuclei imaging. Intrinsically orthogonal coil elements, with different B_1^+ field patterns, for the two different frequencies is one approach. Dual-tuned coils use the same resonant structure to resonate at two different frequencies (Schnall et al., 1985). While this structure generates similar B_1^+ field patters, the additional lumped components affect the transmit efficiency. By appropriate choice of components, the loss in the lower frequency (x-nuclei frequency) is limited to less than 20% while incurring up to 50% loss in the ^{1}H frequency. Several design variants of dual-tuned or dual-frequency setups have been published all with the aim to maximize coil performance at the lower

frequency and to minimize the ^{1}H frequency loss. Nested coils (Brown et al., 2013; Wiggins et al., 2010) and composite coils (Kaggie et al. 2014) are some of them.
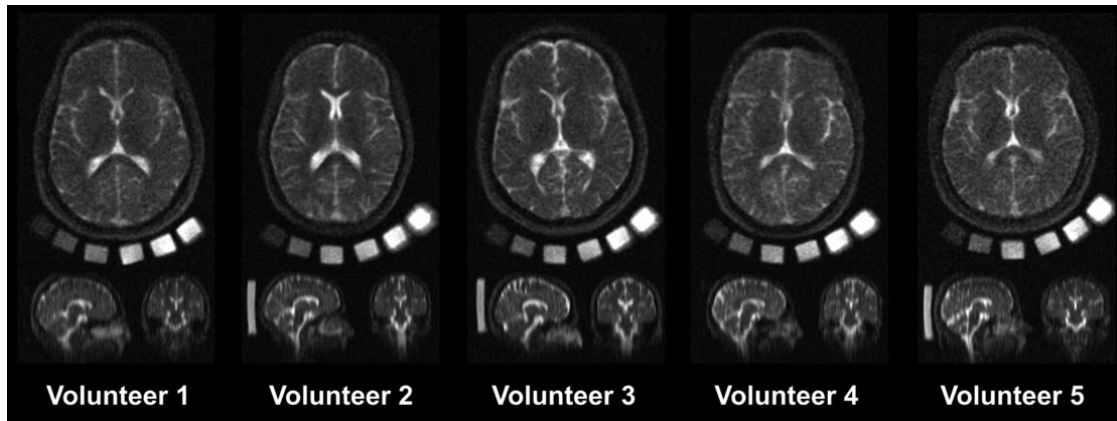

Figure 10. Axial, sagittal and coronal sodium images of five subjects before B_0 and B_1 correction. Reprinted with permission from (Mirkes et al., 2014).

In the example shown in figure 10 from (Mirkes et al., 2014), a proton patch antenna was combined with a sodium birdcage coil to provide proton signal without compromising the efficiency of the X-nucleus coil. Sodium density weighted images with a nominal resolution of 1 x 1 x 5 mm^3 were acquired within 30 min with an ultrashort echo time sequence. The methods used for signal calibration as well as for B_0, B_1 and off-resonance correction were verified on a phantom and five healthy volunteers (Mirkes et al., 2014).

To improve the SNR further, the three layered coil (Shajan et al., 2015), with maximum possible number of receive elements for ^{23}Na receive array was developed. While the SNR in the center of the brain is slightly lower than for a single tuned birdcage coil, it quickly outperforms the birdcage over the entire brain volume. This result also underlines the importance of coil arrangement and choice of loop dimensions for low frequency coil design. The unloaded to loaded Q ratio decreases with frequency and hence the SNR in the deep brain can suffer due to the smaller size of the coil elements. Coil arrangement on the helmet surface is another important factor because arranging coils in the frontal part also contributes to the central SNR. The in vivo example

presented in the article was acquired in only ten minutes and shows a level of detail not previously achieved. Whole brain coverage was achieved even at 400 MHz using a four channel dipole array for B_0 shimming purposes. Though the presence of the sodium transmit and receive array alters the B_1^+ distribution of the dipoles, the shielding effect is minimized by using a 4-element loop array instead of a conventional birdcage resonator. Furthermore, careful choice of cable routing in the multi-element receive array keeps the influence on the ^{1}H frequency to a minimum. The three-layered design approach is well suited for multi-nuclei imaging at ultra-high field as also demonstrated through the 9.4T ^{31}P setup (Shajan et al., 2015).

Several research groups are actively involved in the design of sodium coils and significant gain in SNR has been achieved using innovative coil combinations. The next big leap in this topic would be a coil combination that provides optimum sodium SNR as achieved in some of the setups (Qian et al., 2012; Shajan et al., 2015) but also optimum performance at the ^{1}H frequency.

3.6 RF Coils for MRI at 16.4T

The introduction of whole body high field human MR scanners with field strengths of up to 10.5T and up to 21T for animal research has pushed the limits of achievable SNR. The 16.4T MR scanner installed in our lab had the strongest animal MR magnet at that time. RF coil design for small animal imaging presents a completely different set of challenges. The coil dimensions are much smaller compared to coils for human applications and so the loss factor has a different dimension. While the 9.4 T human ^{1}H coils are sample noise dominant, in small coils for animal imaging applications, sample loss as well as coil loss must be taken in to account. With manufacturers offering up to 16 digital receive channels, it is not always advantageous to arrange a large number of coils on to a small volume because small coil dimensions will lead to penetration issues and the resistive loss from the coil components cannot be ignored. Other major design considerations are the lack of space in the small animal magnets and the possibility to tune and match the coils which are highly sensitive to load variations and to the shielding effect by the bore of the small magnets.

In the traveling wave approach, a remotely placed antenna is used for spin excitation (Brunner et al., 2009). A 3-channel receive array in combination with a patch antenna for imaging at 16.4 T is an extension of this setup. The near field of a tunable patch antenna (Hoffmann et al., 2010) is used for spin excitation. The transmit homogeneity and excitation patterns were comparable to those of a microstrip volume resonator. Significant is the open space this setup provides around the sample which improves access to the sample and provides space for the receive array. High-quality gradient-echo and spin-echo images were acquired to prove its utility. The setup is scalable to other frequencies for small animal imaging applications in small bore magnets.

Conclusion

In conclusion, the different studies presented in this thesis demonstrate the importance of developing customized anatomy specific RF coils for optimum performance. The quality of results depends not only on the design and implementation of the RF coil but is also heavily influenced by the performance of the receive hardware behind each coil element. The various coil implementations sought to find optimal solutions for the quality and reliability aspects of RF components like preamplifiers, TR switches and hybrids to ensure maximum gain in SNR. Precise numerical models were developed for the different coils (Hoffmann et al., 2013). Excellent match between simulation and measurement was achieved (Shajan et al., 2015a; Shajan et al., 2015b) which is an essential aspect not only to ensure that the coil performance is as expected but also for the safety of the subjects.

Chapter 4

SUMMARY

Choice of RF coil technology, the engineering behind its implementation and its performance are significant components towards realizing the promise of ultra-high field (UHF, ≥7T) MRI. A generic excitation coil, similar to the body coil in the clinical scanners, is not available in UHF MR systems due to the complex RF field behavior as the sample dimensions become comparable to the wavelength. Hence, dedicated and application specific RF coil solutions are important at UHF.

Transceiver arrays with microstrip coil elements have been the design of choice in most of the early UHF MR research sites. Design simplicity, small resistive and radiative losses and distinct sensitivity patterns of coil elements that aided RF shimming performance are the deciding factor behind this trend. A 16-channel microstrip transceiver array was developed together with the front-end electronics, which was shown to provide excellent image quality. This setup was then used to demonstrate the feasibility of novel contrast mechanisms at 9.4T. However, the high voltage across the terminating capacitor and the sensitivity towards load variations resulted in reliability issues and additional set up time, respectively.

To extend the longitudinal coverage and to achieve whole brain excitation even at 9.4 T, a dual-row transmit array was designed. In combination with a tight fitting receive array, it provided optimum SNR and 3D RF shimming capability. Integration and control of in-built TR switches and interactions due to the independent receive array were effectively managed. Despite the complexity of this coil combination, an excellent agreement with the numerical model was achieved through precise RF engineering. The dual-row transmit in combination with a receive array is a valuable configuration, which can be applied not only for 9.4T, but will also be used for other ultra-high field MRI applications at field strengths like 7T and 10.5T.

Multi-nuclei imaging at UHF is equally challenging because of the need to incorporate B_0 shimming capability at the ^1H frequency. Transmit efficiency equivalent to a

conventional birdcage coil and significantly high ^{23}Na SNR was achieved using a novel three-layered coil arrangement. In addition, B_0 shimming capability at the ^{1}H frequency was achieved. This new design approach is easily adaptable for other multi-nuclei applications at field strengths ≥ 7T.

In the 16.4T animal scanner, with a proton Larmor frequency of 700 MHz, one of the principal RF engineering challenges is to generate a spatially homogeneous transmit field over a larger volume of interest for spin excitation. Constructing volume coils large enough to house a receive array along with the subject and to maintain quadrature symmetry for different loading conditions is difficult at this frequency. Motivated by the travelling wave approach, a remotely placed capacitively tunable patch antenna that is easily adjustable to different loading conditions was used to achieve homogeneous spin excitation. The tunable antenna in combination with a receive array provided increased SNR and created valuable real estate in the narrow magnet bore around the subject for additional hardware.

All coils developed for human applications were put through extensive compliance testing as per the self-developed validation procedure for patient safety. The RF coil designs for human use presented in this thesis work are all meant for brain imaging applications catering to the research focus of the institute. Design approaches that are successful in imaging the human brain are not necessarily effective for body applications because the body dimensions can be a few times larger than the dimensions of the head. Attempts to image the body at 9.4T would be even more challenging and could lead to several interesting RF coil combinations.

Zusammenfassung

Um die Möglichkeiten der Ultrahochfeld-MR vollständig auszuschöpfen, spielt die für die Hochfrequenzspule verwendete Technologie, ebenso wie ihre technische Realisierung und somit letztlich ihre Leistung, eine entscheidende Rolle. Eine vielseitig verwendbare, große Anregungsspule, wie etwa die Ganzkörperspule in klinischen Geräten, ist in UHF Systemen aufgrund des komplexen Verhaltens hochfrequenter elektromagnetischer Felder mit Wellenlängen derselben Größenordnung wie das gemessene Objekt nicht möglich. Speziell für bestimmte Anwendungen angepasste Hochfrequenzspulen stellen deshalb einen wichtigen Faktor in der Ultrahochfeld-MR dar.

Frühe Ultrahochfeldanwendungen nutzten Transceiver Arrays aus Microstrip-Elementen zu Anregung und Empfang. Ihr einfaches Design, ihre geringen Verluste durch Widerstand und Abstrahlung, sowie die klar lokalisierten Empfindlichkeitsprofile der einzelnen Elemente, die die Anpassung des Anregungsprofils durch RF-Shimming ermöglichen, waren die entscheidenden Faktoren dafür. So wurde auch im Rahmen dieser Arbeit ein 16-Kanal Microstrip Transceiver Array zusammen mit der benötigten Elektronik entwickelt. Mit diesem Aufbau war es möglich, MR Bilder von hervorragender Qualität aufzunehmen. Er wurde unter anderem dazu verwendet, neue Kontrastmechanismen bei 9.4 T aufzuzeigen. Allerdings führten die hohen Spannungen an den Abschluss-kondensatoren zu Einschränkungen in der Verlässlichkeit der Spule, und ihre starke Empfindlichkeit gegenüber Beladungsänderungen erhöhte die Vorbereitungszeit vor jeder Probandenmessung.

Um außerdem den sichtbaren Bereich in Längsrichtung zu erweitern und somit eine Abdeckung des gesamten Gehirns auch bei 9.4 T zu erreichen, wurde ein Sende-Array mit zwei Reihen von Elementen entwickelt, das in Kombination mit einem enganliegenden Empfangs-Array ein hervorragendes SNR in Verbindung mit weitreichenden Möglichkeiten zum RF-Shimming ermöglichte. TR-Switches zum Umschalten zwischen Sende- und Empfangsfunktion wurden in effizienter Form in die Spule integriert und die Wechselwirkungen zwischen Sende- und Empfangselementen wurden erfolgreich kontrolliert.

Trotz der hohen Komplexität dieser Spule konnte dank hochpräziser Konstruktion eine weitgehende Übereinstimmung zwischen dem gemessenen Sendefeld und den Ergebnissen einer Simulation erreicht werden. Diese Verbindung aus einem zweireihigen Sende- und einem Empfangsarray bildet eine vielversprechende Spulenkombination, die nicht nur für die Feldstärke von 9.4 T geeignet ist, sondern auch für 7 T und 10.5 T eingesetzt werden wird.

Die Aufnahme von MR-Signalen anderer Kerne als dem Wasserstoff stellt eine weitere Herausforderung dar, da auch Aufnahmen in der Protonenfrequenz, etwa zum B_0-Shimmen, möglich sein müssen. Mit einem neuartigen Spulendesign in drei Ebenen wurde eine ^{23}Na-Spule entwickelt, die eine ähnliche Sendeeffizienz wie eine Birdcage-Spule mit einem hohen SNR in der Natrium-Frequenz verbindet, und zusätzlich Protonenbilder ermöglicht. Auch dieses Design kann leicht für andere Feldstärken ab 7 T erweitert werden.

Mit einer Larmorfrequenz von 700 MHz besteht das Hauptproblem für Messungen am 16,4 T Kleintiertomographen darin, ein räumlich homogenes Sendefeld über ein größeres Volumen zu erzeugen. Die Entwicklung einer Volumenspule, deren Größe ausreicht, um zusätzlich zum Messobjekt auch noch ein Empfangsarray unterzubringen, und trotzdem für verschiedene Beladungen die Quadratur-Bedingung zu erfüllen, ist bei so hohen Frequenzen schwierig. Die Entwicklung der ‚Travelling Wave‘ Technik war für uns der Anstoß, eine Patchantenne zu entwickeln, die hinter der Probe aufgestellt und kapazitiv an verschiedene Beladungen angepasst werden kann. In Verbindung mit einem Empfangsarray konnten so Daten mit guter Anregungshomogenität und hohem Signal-zu-Rausch Verhältnis aufgenommen werden, wobei um die Probe genügend Platz für andere Hardware blieb.

Alle Spulen, die für Anwendungen am Menschen gedacht sind, wurden strengen und weitreichenden Sicherheitstest unterzogen, für die eigens ausführliche Richtlinien aufgestellt wurden. Die im Rahmen dieser Doktorarbeit entwickelten Spulen sind für Bildgebung am Gehirn gedacht und dienen somit dem neurowissenschaftlichen Forschungsschwerpunkt des Institutes. Das Design einer Spule für die Kopfbildgebung kann allerdings wegen der unterschiedlichen Ausdehnungen nicht direkt auf

Anwendungen im restlichen Körper übertragen werden. Messungen am Oberkörper bei 9,4 T würden weitere anspruchsvolle und interessante HF-Spulenkombinationen benötigen.

5.0 BIBLIOGRAPHY

Abduljalil, A M, A Kangarulu, X Zhang, R E Burgess, and P M Robitaille. 1999. "Acquisition of Human Multislice MR Images at 8 Tesla." *Journal of Computer Assisted Tomography* 23 (3): 335–40.

Adriany, G, A Gozubuyuk, E Auerbach, P F Van de Moortele, P M Andersen, J T Vaughan, and K Ugurbil. 2007. "A 32 Channel Transmit/receive Transmission Line Head Array for 3D RF Shimming." *Proceedings of the Joint Annual Meeting ISMRM-ESMRMB, Berlin, Germany*, 166.

Adriany, Gregor, Pierre Francois Van De Moortele, Johannes Ritter, Steen Moeller, Edward J. Auerbach, Can Akgün, Carl J. Snyder, Thomas Vaughan, and Kamil Ugurbil. 2008. "A Geometrically Adjustable 16-Channel Transmit/receive Transmission Line Array for Improved RF Efficiency and Parallel Imaging Performance at 7 Tesla." *Magnetic Resonance in Medicine* 59 (3): 590–97.

Adriany, Gregor, Pierre Francois Van De Moortele, Florian Wiesinger, Steen Moeller, John P. Strupp, Peter Andersen, Carl Snyder, et al. 2005. "Transmit and Receive Transmission Line Arrays for 7 Tesla Parallel Imaging." *Magnetic Resonance in Medicine* 53 (2): 434–45.

Avdievich, Nikolai I, J W Pan, and H P Hetherington. 2011. "Improved Longitudinal Coverage for Human Brain at 7T: A 16 Element Transceiver Array." *Proceedings of the 19th Annual Meeting of ISMRM, Montreal, Canada*, 328.

Barfuss, H, H Fischer, D Hentschel, R Ladebeck, a Oppelt, R Wittig, W Duerr, and R Oppelt. 1990. "In Vivo Magnetic Resonance Imaging and Spectroscopy of Humans with a 4 T Whole-Body Magnet." *NMR in Biomedicine* 3 (1): 31–45.

Bause, Jonas, Philipp Ehses, Christian Mirkes, G. Shajan, Klaus Scheffler, and Rolf Pohmann. 2015. "Quantitative and Functional Pulsed Arterial Spin Labeling in the Human Brain at 9.4 T." *Magnetic Resonance in Medicine*. doi:10.1002/mrm.25671.

Bloch, F, W W Hansen, and Packard M. 1946. "Nuclear Induction." *Physical Review* 69: 127.

Bomsdorf, H, T Helzel, D Kunz, P Röschmann, O Tschendel, and J Wieland. 1988. "Spectroscopy and Imaging with a 4 Tesla Whole-Body MR System." *NMR in Biomedicine* 1 (3): 151–58.

Bottomley, P A, H R Hart, and W A Edelstein. 1984. "Anatomy and Metabolism of the Normal Human Brain Studied by Magnetic Resonance at 1.5 Tesla." *Radiology*, no. 150: 441–46.

Brown, Ryan, Guillaume Madelin, Riccardo Lattanzi, Gregory Chang, Ravinder R. Regatte, Daniel K. Sodickson, and Graham C. Wiggins. 2013. "Design of a Nested Eight-Channel Sodium and Four-Channel Proton Coil for 7T Knee Imaging." *Magnetic Resonance in Medicine* 70 (1): 259–68.

Brunner, David O, Nicola De Zanche, Jürg Fröhlich, Jan Paska, and Klaas P Pruessmann. 2009. "Travelling-Wave Nuclear Magnetic Resonance." *Nature* 457 (7232): 994–98.

Brunner, Do, N Zanche, J Froehlich, D Baumann, and Kp Pruessmann. 2007. "A Symmetrically Fed Microstrip Coil Array for 7T." *Proceedings of the Joint Annual Meeting ISMRM-ESMRMB, Berlin, Germany*, 448.

Budde, Juliane, G. Shajan, Jens Hoffmann, Kâmil Uğurbil, and Rolf Pohmann. 2011. "Human Imaging at 9.4 T Using T2*, Phase, and Susceptibility-Weighted Contrast." *Magnetic Resonance in Medicine* 65 (2): 544–50.

Budde, Juliane, G. Shajan, Klaus Scheffler, and Rolf Pohmann. 2014. "Ultra-High Resolution Imaging of the Human Brain Using Acquisition-Weighted Imaging at 9.4T." *NeuroImage* 86: 592–98.

Budde, Juliane, G. Shajan, Maxim Zaitsev, Klaus Scheffler, and Rolf Pohmann. 2014. "Functional MRI in Human Subjects with Gradient-Echo and Spin-Echo EPI at 9.4 T." *Magnetic Resonance in Medicine* 71 (1): 209–18.

Collins, Christopher M., Wanzhan Liu, Weston Schreiber, Qing X. Yang, and Michael B. Smith. 2005. "Central Brightening due to Constructive Interference With, Without, and despite Dielectric Resonance." *Journal of Magnetic Resonance Imaging* 21 (2): 192–96.

Damadian, R. 1971. "Tumor Detection by Nuclear Magnetic Resonance." *Science*, no. 171: 1151–53.

Ernst, R R. 1966. "Nuclear Magnetic Double Resonance with an Incoherent Radiofrequency Field." *Journal of Chemical Physics* 45: 3845.

Gilbert, Kyle M., Jean Guy Belliveau, Andrew T. Curtis, Joseph S. Gati, L. Martyn Klassen, and Ravi S. Menon. 2012. "A Conformal Transceive Array for 7 T Neuroimaging." *Magnetic Resonance in Medicine* 67 (5): 1487–96.

Gilbert, Kyle M., Andrew T. Curtis, Joseph S. Gati, L. Martyn Klassen, and Ravi S. Menon. 2011. "A Radiofrequency Coil to Facilitate B1+ Shimming and Parallel Imaging Acceleration in Three Dimensions at 7 T." *NMR in Biomedicine* 24 (7): 815–23.

Haacke, E M, R W Brown, M R Thompson, and R Venkatesan. 1999. *Magnetic Resonance Imaging Physical Principles and Sequence Design*. John Wiley and Sons.

Hahn, E L. 1950. "Spin Echoes." *Physical Review1* 80: 580–94.

Hammond, Kathryn E., Meredith Metcalf, Lucas Carvajal, Darin T. Okuda, Radhika Srinivasan, Dan Vigneron, Sarah J. Nelson, and Daniel Pelletier. 2008. "Quantitative in Vivo Magnetic Resonance Imaging of Multiple Sclerosis at 7 Tesla with Sensitivity to Iron." *Annals of Neurology* 64 (6): 707–13.

Hayes, C E, and L Axel. 1985. "Noise Performance of Surface Coils for Magnetic Resonance Imaging at 1.5 T." *Medical Physics*.

Hayes, Cecil E, William a Edelstein, John F Schenck, Otward M Mueller, and Matthew Eash. 1985. "An Efficient , Highly Hokogeneous Radiofrequency Coil for Whole-Body NMR Imaging at 1 . 5 T." *Journal of Magnetic Resonance* 63: 622–28.

Hoffmann, Jens, G Shajan, and Rolf Pohmann. 2010. "Capacitively Tunable Patch Antenna for Human Head Imaging at 9.4 Tesla." *Proceedings of the 18th Annual Meeting of ISMRM, Honolulu, USA*, 3802.

Hoffmann, Jens, G. Shajan, Juliane Budde, Klaus Scheffler, and Rolf Pohmann. 2013. "Human Brain Imaging at 9.4 T Using a Tunable Patch Antenna for Transmission." *Magnetic Resonance in Medicine* 69 (5): 1494–1500.

Hoffmann, Jens, Gunamony Shajan, Klaus Scheffler, and Rolf Pohmann. 2013. "Numerical and Experimental Evaluation of RF Shimming in the Human Brain at 9.4T Using a Dual-Row Transmit Array." *Magnetic Resonance Materials in Physics, Biology and Medicine*, doi: 10.1007/s10334-013-0419-y.

Hoult, D I, and B Bhakar. 1997. "NMR Signal Reception: Virtual Photons and Coherent Spontaneous Emission." *Concepts In Magnetic Resonance* 9 (5): 277–97.

Hoult, D. I. 2000. "The Principle of Reciprocity in Signal Strength calculations—A Mathematical Guide." *Concepts in Magnetic Resonance* 12 (4): 173–87.

Hoult, D.I, and R.E Richards. 1976. "The Signal-to-Noise Ratio of the Nuclear Magnetic Resonance Experiment." *Journal of Magnetic Resonance (1969)* 24 (1): 71–85.

Kaggie, Joshua D., J. Rock Hadley, James Badal, John R. Campbell, Daniel J. Park, Dennis L. Parker, Glen Morrell, Rexford D. Newbould, Ali F. Wood, and Neal K. Bangerter. 2014. "A 3 T Sodium and Proton Composite Array Breast Coil." *Magnetic Resonance in Medicine* 71 (6): 2231–42.

Keil, Boris, James N. Blau, Stephan Biber, Philipp Hoecht, Veneta Tountcheva, Kawin Setsompop, Christina Triantafyllou, and Lawrence L. Wald. 2013. "A 64-Channel 3T Array Coil for Accelerated Brain MRI." *Magnetic Resonance in Medicine* 70 (1): 248–58.

Keltner, J R, Carlson J W, Roos M S, Wong S T S, Wong T L, and Budinger T F. 1991. "Electromagnetic Fields of Surface Coil in Vivo NMR at High Frequencies." *Magnetic Resonance in Medicine* 22: 467–80.

Kozlov, Mikhail, and Robert Turner. 2011a. "Analysis of RF Transmit Performance for a 7T Dual Row Multichannel MRI Loop Array." *Proceedings of the Annual International Conference of the IEEE Engineering in Medicine and Biology Society, EMBS*, 547–53.

Lauterbur, P C. 1973. "Image Formation by Induced Local Interactions: Examples of Employing Nuclear Magnetic Resonance." *Nature*, no. 242: 190–91.

Lee, Ray F., Christopher J. Hardy, Daniel K. Sodickson, and Paul a. Bottomley. 2004. "Lumped-Element Planar Strip Array (LPSA) for Parallel MRI." *Magnetic Resonance in Medicine* 51 (1): 172–83.

Lee, Ray F., Charles R. Westgate, Robert G. Weiss, David C. Newman, and Paul a. Bottomley. 2001. "Planar Strip Array (PSA) for MRI." *Magnetic Resonance in Medicine* 45 (4): 673–83.

Logothetis, Nikos K., Hellmut Merkle, Mark Augath, Torsten Trinath, and Kâmil Uğurbil. 2002. "Ultra High-Resolution fMRI in Monkeys with Implanted RF Coils." *Neuron* 35 (2): 227–42.

Mansfield, P, and P K Grannell. 1973. "NMR '"diffraction"' in Solids." *Solid State Physics*, no. 6: L422–26.

Mcfarland, E W, and B R Rosen. 1986. "NMR Instrumentation and Hardware Available at Present and in the Future." *Cardiovascular Interventional Radiology*, no. 8: 238–50.

Metzger, Gregory J., Carl Snyder, Can Akgun, Tommy Vaughan, Kamil Ugurbil, and Pierre Francois Van De Moortele. 2008. "Local B1+ Shimming for Prostate Imaging with Transceiver Arrays at 7T Based on Subject-Dependent Transmit Phase Measurements." *Magnetic Resonance in Medicine* 59 (2): 396–409.

Mirkes, Christian C., Jens Hoffmann, G. Shajan, Rolf Pohmann, and Klaus Scheffler. "High-Resolution Quantitative Sodium Imaging at 9.4 Tesla." *Magnetic Resonance in Medicine*. doi:10.1002/mrm.25096.

Orzada, S, H H Quick, M E Ladd, A Bahr, T Bolz, P Yazdanbakhsh, K Solbach, and a K Bitz. 2009. "A Flexible 8-Channel Transmit/receive Body Coil for 7 T Human Imaging." *Proceedings of the 17th Annual Meeting of ISMRM, Honolulu, USA*, 2999.

Pohmann, Rolf, Oliver Speck, and Klaus Scheffler. 2015. "Signal-to-Noise Ratio and MR Tissue Parameters in Human Brain Imaging at 3 , 7 , and 9.4Tesla Using Current Receive Coil Arrays" doi:10.1002/mrm.25677.

Posin, J P, M Arakawa, and L E Crooks. 1985. "Hydrogen MR Imaging of the Head at 0.35 T and 0.7 T: Effects of Magnetic Field Strength." *Radiology*, no. 157: 679–83.

Purcell, E M, H C Torrey, and R B Pound. 1946. "Resonance Absorption by Nuclear Magnetic Moments in a Solid." *Phys Rev*, 37–38.

Qian, Yongxian, Tiejun Zhao, Graham C. Wiggins, Lawrence L. Wald, Hai Zheng, Jonathan Weimer, and Fernando E. Boada. 2012. "Sodium Imaging of Human Brain at 7 T with 15-Channel Array Coil." *Magnetic Resonance in Medicine* 68 (6): 1808–14.

Roemer, P B, W A Edelstein, C E Hayes, S P Souza, and Otward M Mueller. 1990. "The NMR Phased Array." *Magnetic Resonance in Medicine* 16: 192–225.

Roeschmann, Peter K H. 1988. "United States Patent 4746866."

Schnall, M.D, V Harihara Subramanian, J.S Leigh, and B Chance. 1985. "A New Double-Tuned Probed for Concurrent 1H and 31P NMR." *Journal of Magnetic Resonance (1969)* 65 (1): 122–29.

Shajan, G., Jens Hoffmann, Juliane Budde, Gregor Adriany, Kamil Ugurbil, and Rolf Pohmann. 2011. "Design and Evaluation of an RF Front-End for 9.4 T Human MRI." *Magnetic Resonance in Medicine* 66 (2): 596–604.

Shajan, G., Mikhail Kozlov, Jens Hoffmann, Robert Turner, Klaus Scheffler, and Rolf Pohmann. 2014. "A 16-Channel Dual-Row Transmit Array in Combination with a 31-Element Receive Array for Human Brain Imaging at 9.4 T." *Magnetic Resonance in Medicine* 71 (2): 870–79.

Shajan, G., Christian Mirkes, Kai Buckenmaier, Jens Hoffmann, Rolf Pohmann, and Klaus Scheffler. 2015. "Three-Layered Radio Frequency Coil Arrangement for Sodium MRI of the Human Brain at 9.4 Tesla." *Magnetic Resonance in Medicine.* doi:10.1002/mrm.25666.

Shajan, G;, Jens; Hoffmann, Rolf; Pohmann, and Scheffler Klaus. 2015. "Proc. Intl. Soc. Mag. Reson. Med. 23 (2015) 1815." *Proceedings of the 23rd Annual Meeting of ISMRM, Toronto, Canada* 23.

Shajan, G, Jens Hoffmann, Klaus Scheffler, and Rolf Pohmann. 2012. "A 16-Element Dual-Row Transmit Coil Array for 3D RF Shimming at 9.4 T." *Proceedings of the 20th Annual Meeting of ISMRM, Melbourne, Australia* 20: 308.

Shajan, G; Mirkes, Christian; Pohmann R, Scheffler K. 2015. "Proc. Intl. Soc. Mag. Reson. Med. 23 (2015) 3148." *Proceedings of the 23rd Annual Meeting of ISMRM, Toronto, Canada* 23: 3148.

Soher, B J, B M Dale, and E M Merkle. 2007. "A Review of MR Physics: 3T versus 1.5T." *Magnetic Resonance Imaging Clinics of North America* 15: 277–90.

Van De Moortele, Pierre François, Can Akgun, Gregor Adriany, Steen Moeller, Johannes Ritter, Christopher M. Collins, Michael B. Smith, J. Thomas Vaughan, and Kamil Ugurbil. 2005. "B1 Destructive Interferences and Spatial Phase Patterns at 7 T with a Head Transceiver Array Coil." *Magnetic Resonance in Medicine* 54 (6): 1503–18.

Vaughan, J Thomas, Hoby P Hetherington, Joe Otu, Jullie W Pan, and Gerald M Pohost. 1994. "High Frequency Volume Coils for Clinical NMR Imaging and Spectroscopy." *Magnetic Resonance in Medicine*, no. 32: 206–18.

Vaughan, J. T., G. Adriany, C. J. Snyder, J. Tian, T. Thiel, L. Bolinger, H. Liu, L. DelaBarre, and K. Ugurbil. 2004. "Efficient High-Frequency Body Coil for High-Field MRI." *Magnetic Resonance in Medicine* 52 (4): 851–59.

Vaughan, J. T., M. Garwood, C. M. Collins, W. Liu, L. Delabarre, G. Adriany, P. Andersen, et al. 2001. "7T vs. 4T: RF Power, Homogeneity, and Signal-to-Noise Comparison in Head Images." *Magnetic Resonance in Medicine* 46 (1): 24–30.

Vaughan, Thomas, Lance DelaBarre, Cari Snyder, Jinfeng Tian, Can Akgun, Devashish Shrivastava, Wanzahn Liu, et al. 2006. "9.4T Human MRI: Preliminary Results." *Magnetic Resonance in Medicine* 56 (6): 1274–82.

Wang, Jinghua, Qing X. Yang, Xiaoliang Zhang, Christopher M. Collins, Michael B. Smith, Xiao Hong Zhu, Gregor Adriany, Kamil Ugurbil, and Wei Chen. 2002. "Polarization of the RF Field in a Human Head at High Field: A Study with a Quadrature Surface Coil at 7.0 T." *Magnetic Resonance in Medicine* 48 (2): 362–69.

Wiggins, G C, R Brown, L Fleysher, B Zhang, B Stoeckel, M Inglese, and D K Sodickson. 2010. "A Nested Dual Frequency Birdcage/Stripline Coil for Sodium/Proton Brain Imaging at 7T." *Proceedings of the 18th Annual Meeting of ISMRM, Honolulu, USA*, 1500.

Wiggins, Graham C., C. Triantafyllou, a. Potthast, a. Reykowski, M. Nittka, and L. L. Wald. 2006. "32-Channel 3 Tesla Receive-Only Phased-Array Head Coil with Soccer-Ball Element Geometry." *Magnetic Resonance in Medicine* 56 (1): 216–23.

Wright, Sm, and Ll Wald. 1997. "Theory and Applications of Array Coils in MR Spectroscopy." *NMR in Biomedicine* 10: 394–410.

Yang, Qing X., Jinghua Wang, Xiaoliang Zhang, Christopher M. Collins, Michael B. Smith, Haiying Liu, Xiao Hong Zhu, J. Thomas Vaughan, Kamil Ugurbil, and Wei Chen. 2002. "Analysis of Wave Behavior in Lossy Dielectric Samples at High Field." *Magnetic Resonance in Medicine* 47 (5): 982–89.

Zhang, Xiaoliang, Kamil Ugurbil, and Wei Chen. 2001. "Microstrip RF Surface Coil Design for Extremely High-Field MRI and Spectroscopy." *Magnetic Resonance in Medicine* 46 (3): 443–50.

Zhang, Xiaoliang, Kamil Ugurbil and Wei Chen. 2003. "A Microstrip Transmission Line Volume Coil for Human Head MR Imaging at 4 T." *Journal of Magnetic Resonance* 161 (2): 242–51.

Zhang, Xiaoliang, Kamil Ugurbil, Robert Sainati, and Wei Chen. 2005. "An Inverted-Microstrip Resonator for Human Head Proton MR Imaging at 7 Tesla." *IEEE Transactions on Biomedical Engineering* 52 (3): 495–504.

6.0 AUTHOR CONTRIBUTIONS

1. Design and evaluation of an RF front-end for 9.4 T human MRI

G. Shajan, Jens Hoffmann, Juliane Budde, Gregor Adriany, Kamil Ugurbil and Rolf Pohmann

Journal reference: Magnetic Resonance in Medicine 66(2) 594–602

Synopsis: Constructive and destructive interferences cause strong inhomogeneities in the B_1 field produced by a volume coil causing shading over large parts of the image. This effect is even more severe at 9.4 T than at 7 T because the wavelength in average brain tissue is as low as 10.6 cm. Specialized radio frequency hardware and B_1 management methods are required to obtain high-quality images. A radio frequency front-end consisting of custom-built preamplifiers, TR switches and a 16-channel microstrip transceiver array coil was developed. Destructive interference patterns were eliminated, in virtually the entire brain, using a simple in situ radio frequency phase shimming technique.

Contributions:

G. Shajan: Design of microstrip array, design of TR switches, design of preamplifiers, bench testing and optimization, data collection, validation in scanner, preparation of manuscript.

Jens Hoffmann: EM simulation, B_1 shimming, validation in scanner, data collection, contribution to manuscript and correction.

Juliane Budde: Validation in scanner and manuscript correction.

Gregor Adriany: Design inputs for microstrip array design.

Kamil Ugurbil: Advice on manuscript.

Rolf Pohmann: Project supervision and advice on manuscript.

2. A 16-channel dual-row transmit array in combination with a 31-element receive array for human brain imaging at 9.4T

G. Shajan, Mikhail Kozlov, Jens Hoffmann, Robert Turner, Klaus Scheffler and Rolf Pohmann.

Journal reference: Magnetic Resonance in Medicine 71(2) 870–879

Synopsis: Multi-row transmit array provides an additional degree of freedom to correct B_1^+ field inhomogeneities along the longitudinal direction and achieve whole brain excitation at ultra-high field strengths. Receive arrays shaped to the contours of the anatomy are used to increase the signal-to-noise ratio (SNR). A unique RF coil configuration, that combines the advantages of transmit array and receive array techniques, was developed. Whole brain coverage at 9.4T, three dimensional RF shimming capability and significant increase in SNR was achieved using our novel coil combination.

Contributions:

G. Shajan: Conceptualize and design of dual-row transmit array, design of receive array, integration and testing of the two arrays, design of miniaturized TR switches, bench testing, troubleshooting and validation in scanner, data collection, safety testing and preparation of manuscript.

Mikhail Kozlov: EM simulation, contribution to manuscript and correction.

Jens Hoffmann: Validation in scanner, data collection, safety simulation, safety evaluation and documentation, manuscript correction.

Robert Turner: Advice on manuscript.

Klaus Scheffler: Project supervision and advice on manuscript.

Rolf Pohmann: SNR comparison study, project supervision and advice on manuscript.

3. Three-layered radio frequency coil arrangement for sodium MRI of the human brain at 9.4 Tesla

G. Shajan, Christian Mirkes, Kai Buckenmaier, Jens Hoffmann, Rolf Pohmann and Klaus Scheffler.

Synopsis: Sodium MRI at ultra-high field (UHF) is highly beneficial because of the increase in SNR with respect to the strength of the static magnetic field. Furthermore, B_0 shimming is an essential requirement at UHF because the field inhomogeneity increases with field strength. A novel RF coil configuration combining three RF coil arrays in an integrated dual-frequency setup was developed. We demonstrate that optimum SNR, efficient transmit excitation and B_0 shimming capability can be achieved using the three-layered coil arrangement.

Contributions:

G. Shajan: Hardware design concept, design of the entire hardware, hardware integration, troubleshooting and bench testing, validation in scanner and preparation of manuscript.

Christian Mirkes: Formulation of requirements for [23]Na MRI, validation in scanner and troubleshooting, data acquisition, contribution to manuscript and correction.

Kai Buckenmaier: EM simulation, safety documentation, manuscript correction.

Jens Hoffmann: Contribution to EM simulation, manuscript correction.

Rolf Pohmann: Advice on manuscript.

Klaus Scheffler: Project supervision, and advice on manuscript.

4. Rat brain MRI at 16.4T using a capacitively tunable patch antenna in combination with a receive array

G. Shajan, Jens Hoffmann, David Balla, Dinesh Deelchand, Klaus Scheffler and Rolf Pohmann.

Journal reference: NMR in Biomedicine 25(10) 1170-1176.

Synopsis: The principal RF engineering challenge at 16.4T is to generate a spatially homogeneous transmit field over a volume of interest. This calls for new approaches to RF coil design for extremely high field strength magnets. A remotely placed capacitively tunable patch antenna was used to generate a relatively homogeneous excitation field covering a large imaging volume. To enhance the receive sensitivity, the transmit antenna was combined with an actively detunable 3-channel receive coil array. In addition to increased SNR compared to a quadrature transceive surface coil, we were able to get high quality gradient echo and spin-echo images covering the whole rat brain.

Contributions:

G. Shajan: Design of receive array, design of TR switches, design of preamplifiers, bench testing, troubleshooting and validation in scanner, data collection and preparation of manuscript.

Jens Hoffmann: EM simulation, transmit antenna design, validation in scanner, contribution to manuscript and correction.

David Balla: Coil interface to scanner, data acquisition and correction of manuscript.

Dinesh Deelchand: Transmit field map measurement.

Klaus Scheffler: Advice on manuscript.

Rolf Pohmann: Project supervision and advice on manuscript.

Acknowledgements

Sincere thanks to all my colleagues in the department and Tina Schroeder in particular. You all make this a lovely place to work.

My heartfelt thanks to Prof. Fritz Shick, who is my supervisor from the University of Tuebingen.

Lastly, my heartfelt thanks to my wife Binu and my grandma Mary Lizzie. Thank you for being what you are to me.

Thank you all!

Curriculum vitae

Shajan Gunamony, born on 5th January 1974.

Summary

I have 17 years of experience in premier institutions like Indian Space Research Organization, Bangalore and Max Planck Institute, Germany. I have hands-on experience in designing MRI RF coils for various MRI scanners with field strengths from 1T up to 16.4T and RF subsystems for space applications.

Educational Qualification

Degree/ School	Institute/ Univ.	Specialization	Year of passing	Score
B.E.	Karunya Institute of Technology, Coimbatore, India	Electronics and Communication	1995	74.5%
M.E	Thiagarajar College Of Engineering, Madurai, India.	Communication Systems	1998	75%
PhD	Max Planck Institute, Tuebingen / University of Tuebingen	Doctoral thesis is under review. Thesis defense is expected before the end of 2015.		

Professional Experience

05/1998 to 11/2000: Scientist/Engineer at the Indian Space Research organization, Bangalore, India.

2001 to 06/2007: Senior systems specialist at GE Healthcare Technologies, Bangalore, India.

Since 06/2007: Research Scientist at the MPI for Biological Cybernetics, Tuebingen, Germany.

Patent

1. RF Coil Assembly US patent No. 7605588 / HF-Spulenanordnung (DE102006050989A1)

2. Multichannel coil for UHF MRI. File No.: MI 0107-4677-BC-JK, Max Planck Innovation.

Scientific activities

Reviewer in NMR in biomedicine since 2012

Reviewer in Magnetic resonance in Medicine since 2012

Faculty member in the RF coil building course organized by ESMRMB

Membership

Member in ISMRM since 2008

Member in ESMRMB since 2012

Peer-reviewed Publications

Four first author and 17 co-author publications

1. **G. Shajan,** Jens Hoffmann, Juliane Budde, Gregor Adriany, Kamil Ugurbil and Rolf Pohmann. Design and evaluation of an RF front-end for 9.4 T human MRI. Magn Reson Med 2011; 66: 594–602

2. **G. Shajan**, Mikhail Kozlov, Jens Hoffmann, Robert Turner, Klaus Scheffler and Rolf Pohmann. A 16-channel dual-row transmit array in combination with a 31-element receive array for human brain imaging at 9.4T. Magn Reson Med 2014; 71: 870–879

3. **G. Shajan**, Christian Mirkes, Kai Buckenmaier, Jens Hoffmann, Rolf Pohmann and Klaus Scheffler. Three-layered radio frequency coil arrangement for sodium MRI of the human brain at 9.4 Tesla. Magn Reson Med DOI 10.1002/mrm.25666

4. **G. Shajan**, Jens Hoffmann, David Balla, Dinesh Deelchand, Klaus Scheffler and Rolf Pohmann. Rat brain MRI at 16.4T using a capacitively tunable patch antenna in combination with a receive array. NMR in Biomed 2012; 25: 1170-1176.

Co-authored peer-reviewed articles:

1. Hong S-T, Balla DZ, **G. Shajan**, Choi C , Ugurbil K and Pohmann R. Enhanced neurochemical profile of the rat brain using in vivo 1H NMR spectroscopy at 16.4 T. Magn Reson Med 2011; 65: 28-34.
2. Budde J, **G. Shajan**, Hoffmann J, Ugurbil K and Pohmann R. Human imaging at 9.4 T using T2*-, phase-, and susceptibility-weighted contrast. Magn Reson Med 2011; 65: 544-550.
3. Pohmann R, **G. Shajan** and Balla D. Contrast at high field: Relaxation times, magnetization transfer and phase in the rat brain at 16.4 T. Magn Reson Med 2011; 66: 1572-1581.
4. Pohmann R, **G. Shajan**, Hoffmann J, Budde J, Hagberg G, Bieri O, Bisdas S, Ernemann U, Weigel M, Ehses P, Hennig J, Chadzynski G and Scheffler K. Imaging and Spectroscopy at 9.4 Tesla: First Results on Patients and Volunteers *MAGNETOM Flash* 2013; 58-67.
5. Hoffmann J, **G. Shajan**, Budde J, Scheffler K and Pohmann R. Human brain imaging at 9.4 T using a tunable patch antenna for transmission. Magn Reson Med 2013; 69: 1494-1500.
6. Balla DZ, Gottschalk S, **G. Shajan**, Ueberberg S, Schneider S, Hardtke-Wolenski M, Jaeckel E, Hoerr V, Faber C, Scheffler K, Pohmann R and Engelmann J. In vivo visualization of single native pancreatic islets in the mouse *Contrast Media & Molecular Imaging* 2013; 8: 495-504.
7. Budde J, **G. Shajan**, Zaitsev M, Scheffler K and Pohmann R. Functional MRI in human subjects with gradient-echo and spin-echo EPI at 9.4 T. Magn Reson Med 2014; 71: 209-218.

8. Budde J, **G. Shajan**, Scheffler K and Pohmann R. Ultra-high resolution imaging of the human brain using acquisition-weighted imaging at 9.4 T. *NeuroImage* 2014; 86: 592–598.

9. Hoffmann J, **G. Shajan**, Scheffler K and Pohmann R. Numerical and experimental evaluation of RF shimming in the human brain at 9.4 T using a dual-row transmit array. *Magnetic Resonance Materials in Physics, Biology and Medicine* 2014; 27: 373-386.

10. Ehses P, Bause J, **G. Shajan** and Scheffler K. Efficient generation of T2*-weighted contrast by interslice echo-shifting for human functional and anatomical imaging at 9.4 Tesla *Magn Reson Med*, DOI 10.1002/mrm.25570.

11. Mirkes C, Hoffmann J, **G. Shajan**, Pohmann R and Scheffler K. High-resolution quantitative sodium imaging at 9.4 tesla. Magn Reson Med 2015; 73: 342–351.

12. Hoffmann J, Mirkes C, **G. Shajan**, Scheffler K and Pohmann R. Combination of a multimode antenna and TIAMO for traveling-wave imaging at 9.4 Tesla. Magn Reson Med. DOI 10.1002/mrm.25614

13. Mirkes C, **G. Shajan**, Bause J, Buckenmaier K, Hoffmann J and Scheffler K. Triple-quantum-filtered sodium imaging at 9.4 Tesla. Magn Reson Med DOI: 10.1002/mrm.25688

14. Hoffmann J, Henning A, Giapitzakis IA, Scheffler K, **G. Shajan**, Pohmann R and Avdievich NI. Safety testing and operational procedures for self-developed radiofrequency coils. NMR in Biomedicine. DOI: 10.1002/nbm.3290.

15. Bause J, Ehses P, Mirkes C, **G. Shajan**, Scheffler K and Pohmann R. Quantitative and functional pulsed arterial spin labeling in the human brain at 9.4 T. Mag Reson Med. DOI 10.1002/mrm.25671

16. Chadzynski GL, Pohmann R, **G. Shajan**, Kolb R, Bisdas S, Klose U and Scheffler K. In vivo proton magnetic resonance spectroscopic imaging of the healthy human brain at 9.4 T: initial experience. *Magnetic Resonance Materials in Physics, Biology and Medicine 2015;* 28: 239-249.

17. Wiesner HM, Balla DZ, **G. Shajan**, Scheffler K, Ugurbil K, Chen W, Uludag K and Pohmann R. 17O relaxation times in the rat brain at 16.4 tesla. Magn Reson Med. DOI 10.1002/mrm.25814.

Conference proceedings: Eight as first author and more than 50 as co-author in ISMRM and ESMRMB.

Curriculum vitae

G. Shajan was born to K. Gunamony and K. Anlet on the 5th of January 1974 in Neyyoor, situated in the southern state of Tamilnadu in India. Shajan completed his higher secondary education in 1991 from Scott christian higher secondary school, Nagercoil and bachelors degree in electronics and communication engineering from Karunya institute of technology, Coimbatore in the year 1995. He completed his masters degree in communication engineering with distinction in early 1998 from Thiagarajar college of Engineering, Madurai under the guidance of Prof. Dr. V. Abhai Kumar. The strong collaboration between the institute and the country's defense research and development organization (DRDO) provided him with the opportunity to undertake his masters degree project at LRDE, Bangalore under Dr. U.K Revankar, who introduced him to the design of low noise amplifiers for C-band frequencies.

Soon after, Shajan was offered a job at the Indian Space Research Organization in Bangalore where he continued to work on the development of RF amplifiers in the frequency range of 12 GHz. When GE started the MR team in Bangalore, Shajan joined the engineering group in 2001 and together with his colleagues, developed and manufactured the plant's first RF coil. The team grew and the facility went on to become one of GE Healthcare's largest RF coil design and manufacturing site.

Prof. Kamil Ugurbil offered him the opportunity to build RF coils for 9.4T and 16.4T scanners, two of world's strongest MRI scanners in respective categories at that time, installed at the Max Planck Institute of biological cybernetics in Tuebingen. Shajan moved with his wife and two sons to Tuebingen in summer 2007. The two scanners being unique in frequency, not only the RF coils, the entire RF front end including the preamplifiers had to be custom-built. Shajan received excellent support from Prof. Dr. Klaus Scheffler and Dr. Rolf Pohmann for the RF coil program at MPI, Tuebingen. A variety of ^{1}H and multi-nuclei coils for brain imaging of humans, rodents and non-human primates for the different magnets in the institute were developed. Coil technology for human MRI at 9.4T advanced from spending an hour to set up an experiment to routine studies comparable to clinical environment.